

University of Windsor

## Scholarship at UWindor

---

Electronic Theses and Dissertations

Theses, Dissertations, and Major Papers

---

2011

### Experimental and Numerical Analysis of Sidewall Curl in Advanced High Strength Steels

ALI ARYANPOUR  
*University of Windsor*

Follow this and additional works at: <https://scholar.uwindsor.ca/etd>

---

#### Recommended Citation

ARYANPOUR, ALI, "Experimental and Numerical Analysis of Sidewall Curl in Advanced High Strength Steels" (2011). *Electronic Theses and Dissertations*. 171.  
<https://scholar.uwindsor.ca/etd/171>

This online database contains the full-text of PhD dissertations and Masters' theses of University of Windsor students from 1954 forward. These documents are made available for personal study and research purposes only, in accordance with the Canadian Copyright Act and the Creative Commons license—CC BY-NC-ND (Attribution, Non-Commercial, No Derivative Works). Under this license, works must always be attributed to the copyright holder (original author), cannot be used for any commercial purposes, and may not be altered. Any other use would require the permission of the copyright holder. Students may inquire about withdrawing their dissertation and/or thesis from this database. For additional inquiries, please contact the repository administrator via email ([scholarship@uwindsor.ca](mailto:scholarship@uwindsor.ca)) or by telephone at 519-253-3000ext. 3208.

**EXPERIMENTAL & NUMERICAL STUDY  
OF SIDEWALL CURL IN  
ADVANCED HIGH STRENGTH STEELS**

By  
Ali ARYANPOUR

A Thesis  
Submitted to the Faculty of Graduate Studies  
through Mechanical, Automotive and Materials Engineering  
in Partial Fulfillment of the Requirements for  
the Degree of Master of Applied Science at the  
University of Windsor

Windsor, Ontario, Canada

2011

©2011 Ali Aryanpour

# Experimental & Numerical Analysis of Sidewall Curl in Advanced High Strength Steels

By  
Ali Aryanpour

APPROVED BY:

---

Dr. V. Stoilov, Outside Reader  
Department of Mechanical, Automotive and Materials Engineering

---

Dr. W. Altenhof, Program Reader  
Department of Mechanical, Automotive and Materials Engineering

---

Mr. M. Rodzik, Industrial Advisor  
The NARMCO Group

---

Dr. D. E. Green, Advisor  
Department of Mechanical, Automotive and Materials Engineering

---

Dr. B. Zhou, Chair of Defense  
Department of Mechanical, Automotive and Materials Engineering

October 18, 2011

## **Author's Declaration of Originality**

I hereby certify that I am the sole author of this thesis and that no part of this thesis has been published or submitted for publication.

I certify that, to the best of my knowledge, my thesis does not infringe upon anyone's copyright nor violate any proprietary rights and that any ideas, techniques, quotations, or any other material from the work of other people included in my thesis, published or otherwise, are fully acknowledged in accordance with the standard referencing practices. Furthermore, to the extent that I have included copyrighted material that surpasses the bounds of fair dealing within the meaning of the Canada Copyright Act, I certify that I have obtained a written permission from the copyright owner(s) to include such material(s) in my thesis and have included copies of such copyright clearances to my appendix.

I declare that this is a true copy of my thesis, including any final revisions, as approved by my dissertation committee and the Graduate Studies office, and that this dissertation has not been submitted for a higher degree to any other University or Institution.

## ABSTRACT

Sidewall curl is a type of springback deformation resulting from successive bending-unbending when a sheet metal is drawn over a die radius or through a drawbead. In this study, the sidewall curl in stamped AHSS parts (TRIP780 and DP980) was predicted using four models from LS-DYNA material library: 24, 36, 37, 125 and a UMAT in ABAQUS based on the Yoshida-Uemori model. Various material characterization tests were analyzed to identify the input parameters. Plane-strain channel sections were drawn in a specialized die with adjustable drawbeads and various die entry radii and compared with simulation results. By increasing drawbead penetration, the springback angle decreased but the sidewall curl increased in the channel sections. For simulations in LS-DYNA, MAT37 with increased integration points predicted the most accurate results. The YU model in ABAQUS showed less than 8% error compared to the predicted sidewall curl for channel sections with shallow drawbeads.

*Dedicated to my wife, for her loving support*

## ACKNOWLEDGEMENTS

I wish to express my greatest gratitude for my advisor, Dr. Daniel E. Green in providing continuous support and helpful ideas in the course of my graduate studies and different stages of my research. I consider myself to be very fortunate to work under his supervision and learn from him in discipline, knowledge and character.

I would like to thank my thesis committee members, Dr. William Altenhof, Dr. Vesselin Stoilov and Matthew Rodzik for their valuable comments and recommendations. I should also express my great appreciation for the discussions and exchange of ideas with my colleague, Amir Hassannejad-asl.

During the course of my studies and throughout the difficulties experienced during this time, I received full support from my beloved wife and helpful advice from my brothers. I wish to thank them and all my family for their belief in me and the strength I gained from their encouragement.

Finally, I want to express my sincere gratitude to the following individuals and organizations:

- Professor Chester Van Tyne and Lee Rothleutner from Colorado School of Mines, for carrying out the Unloading modulus experiments.
- Dr. Ming Shi from USSteel, for carrying out the cyclic tension-compression tests.
- Patrick Seguin, for his help in performing the uniaxial tensile tests and upgrading the data acquisition system.
- Brian Vensk, Kapco Tool& Die Co. plant manager, for his numerous supports and advices during the experimental phase of the project.
- The Narmco group for sponsoring the channel draw experiments and in-kind provision of the study materials.

# Table of Contents

<b>Author's Declaration of Originality</b>	<b>iii</b>
<b>Abstract</b>	<b>iv</b>
<b>Dedication</b>	<b>v</b>
<b>Acknowledgements</b>	<b>vi</b>
<b>List of Tables</b>	<b>ix</b>
<b>List of Figures</b>	<b>x</b>
<b>List of Abbreviations and Symbols</b>	<b>xv</b>
<b>1 Introduction</b>	<b>1</b>
1.1 Overview . . . . .	1
1.2 Sidewall curl and springback . . . . .	2
1.3 Springback of Advanced High Strength Steels . . . . .	5
1.4 Prediction and Compensation . . . . .	9
1.5 Objective and outline of thesis . . . . .	11
<b>2 Material Models</b>	<b>13</b>
2.1 Introduction . . . . .	13
2.2 Literature review . . . . .	14
2.2.1 Early studies . . . . .	14
2.2.2 Analytical solutions . . . . .	16
2.2.3 Numerical studies . . . . .	19
2.2.4 Constitutive material models . . . . .	22
2.2.5 Identification of material parameters . . . . .	30
2.3 Yoshida-Uemori two-surface plasticity model . . . . .	33
2.3.1 Degradation of elastic stiffness during unloading . . . . .	39
2.3.2 Identify the YU Hardening parameters from cyclic tests . . . . .	42
2.4 LS-DYNA material models for sheet metal forming . . . . .	45
<b>3 Experimental study</b>	<b>50</b>
3.1 Introduction . . . . .	50
3.2 Description of the channel draw process . . . . .	50



3.2.1	Data acquisition system . . . . .	59
3.3	Experimental results of channel draw for DP980 and TRIP780 . . . . .	62
3.3.1	Punch force vs. displacement curves . . . . .	62
3.3.2	Channel sidewall profiles . . . . .	68
3.3.3	Thickness reduction and strain distribution . . . . .	75
3.4	Material characterization and mechanical properties . . . . .	77
3.4.1	Uniaxial tension tests . . . . .	78
3.4.2	Unloading elastic modulus . . . . .	84
3.4.3	Cyclic Tension and Compression tests . . . . .	91
3.4.4	Friction coefficient . . . . .	94
<b>4</b>	<b>Numerical Analysis</b>	<b>95</b>
4.1	Introduction . . . . .	95
4.2	Determination of Constitutive Material Parameters . . . . .	96
4.3	Finite element model of channel draw . . . . .	105
4.4	Results of channel forming simulations . . . . .	114
4.4.1	Punch Force vs. Displacement curves . . . . .	114
4.4.2	Channel sidewall profiles . . . . .	126
4.4.3	Thickness reduction and strain distribution . . . . .	135
<b>5</b>	<b>Final Discussions and Conclusions</b>	<b>140</b>
<b>A</b>	<b>Simulation of B-pillar</b>	<b>148</b>
	<b>Bibliography</b>	<b>150</b>
	<b>Vita Auctoris</b>	<b>158</b>

# List of Tables

3.1	Geometrical dimensions for channel draw process . . . . .	57
3.2	Adjustable parameters of drawbeads and kiss blocks for each configuration . . . . .	57
3.3	Specifications of channel draw conditions with different die entry radius and no drawbeads . . . . .	66
3.4	Geometrical measures of channel draw experiments for various drawbead penetrations . . . . .	73
3.5	Principal strains and thickness of blanks measured in channel sidewalls . . . . .	77
3.6	Summary of mechanical properties measured by tensile tests at USSteel . . . . .	82
3.7	Average experimental results for Unloading Elastic Modulus . . . . .	87
3.8	Identified parameters for decay formula of unloading elastic modulus for prestrains up to 4.5% . . . . .	87
3.9	Identified parameters for decay formula of unloading elastic modulus with prestrain 12% for TRIP780 and 9% for DP980 . . . . .	90
4.1	Intermediate YU model parameters from systematic analysis of tension compression test . . . . .	96
4.2	Optimized YU model parameters for LS-DYNA with Mat125 . . . . .	102
4.3	Original YU parameters reported in another study . . . . .	105
4.4	Coefficients for Hill's 1948 yield function . . . . .	112
4.5	Stress anisotropic ratios for channel model in ABAQUS . . . . .	113
4.6	Transverse shear stiffness for channel model in ABAQUS . . . . .	113
4.7	Geometrical measures for channel sidewall profiles with shallow beads, predicted with LS-DYNA . . . . .	132
4.8	Geometrical measures for channel sidewall profiles without beads and DER=12 mm, predicted with LS-DYNA . . . . .	133
4.9	Summary of maximum values of thickness reduction and plastic strains predicted in the channel sidewalls . . . . .	136

# List of Figures

1.1	Different types of sidewall springback . . . . .	4
1.2	Origin and Mechanism of Sidewall curl . . . . .	4
1.3	Elastic recovery comparison between AHSS and MS during unloading . . . . .	5
1.4	Schematic of AHSS steels compared to conventional HSS and mild steels . . . . .	6
1.5	TRIP350/600 with a greater elongation than DP350/600 and HSLA350/450 . . . . .	7
1.6	Two channels made sequential in the same die . . . . .	8
1.7	Elastic recovery comparison between AHSS and MS during unloading . . . . .	8
1.8	The AHSS have greater sidewall curl for equal tensile strength steels . . . . .	9
1.9	Design process schematic . . . . .	11
2.1	Effect of stretching in SHAPESSET process . . . . .	15
2.2	A schematic diagram of the 2-D draw bending operation . . . . .	16
2.3	Schematic of straight flanging process . . . . .	17
2.4	Geometry of the draw bend test with deformed shape before and after springback . . . . .	18
2.5	Schematics of cylindrical and 2-D draw bending tests and a double-S rail . . . . .	21
2.6	Description of isotropic hardening model with the uniaxial stress-strain curve . . . . .	23
2.7	Description of kinematic hardening model showing the translation and the resulting stress-strain curve with shifted yield stress in compression . . . . .	25
2.8	Schematics of the isotropic hardening in the deviatoric plane and the stress vs. plastic strain response . . . . .	27
2.9	Schematics of the linear kinematic hardening in the deviatoric plane and the stress vs. plastic strain response . . . . .	27
2.10	Schematic showing the stress-strain response with and without Bauschinger effect during forward and reverse loading paths . . . . .	28
2.11	Stress-strain response of a mild steel in a forward and reverse loading and the cyclic phenomena . . . . .	34

---

2.12	Schematic illustration of the YU two-surface model . . . . .	35
2.13	Definition of the parameters in the Yoshida-Uemori hardening model . . . . .	37
2.14	Schematic illustration of stagnation surface . . . . .	38
2.15	An example of unloading stress-strain response for the high strength steel sheet . . . . .	41
2.16	A schematic illustration of the stress-strain relationship of an unloading/reloading cycle . . . . .	41
2.17	Schematic illustration of stress-strain response during forward and reverse deformation for identification of YU hardening parameters . . . . .	42
2.18	Schematic illustrations of the motion of the yield and bounding surfaces under a uniaxial forward-reverse deformation . . . . .	43
3.1	A/SP die installed in a hydraulic press . . . . .	52
3.2	sideview of the A/SP die components and general dimension parameters . . . . .	53
3.3	Draw die schematic view . . . . .	53
3.4	Illustration of symmetry in the channel draw process . . . . .	54
3.5	Drawbead at 0% penetration . . . . .	55
3.6	Drawbead at 100% penetration . . . . .	56
3.7	Electroetching a grid of circles of 0.1(in) diameter onto one side of a blank . . . . .	58
3.8	Sample of channels produced for various drawbead configurations	59
3.9	Front panel of the data acquisition software . . . . .	60
3.10	Sensors used for the data acquisition system . . . . .	61
3.11	Experimental punch force-displacement curves for TRIP780 channels drawn with various drawbead penetrations . . . . .	63
3.12	Experimental punch force-displacement curves for DP980 channels drawn with various drawbead penetrations . . . . .	64
3.13	Experimental punch force-displacement curve for DP980 channels drawn with a shallow bead penetration (20%) . . . . .	65
3.14	Channels drawn with various die entry radii and without drawbeads . . . . .	65
3.15	omparison of punch force-displacement curves for TRIP780 channels drawn with shallow bead penetration (20%) when blanks are cut parallel to the rolling and the transverse directions . . . . .	66

---

3.16	Experimental punch force-displacement curves for TRIP780 channels drawn without beads and with various die entry radii, and for blanks cut in either the rolling or transverse directions . . . . .	67
3.17	Experimental punch force-displacement curves for DP980 channels drawn with various die entry radii . . . . .	68
3.18	Geometrical measures of sidewall curl for channel profile . . . . .	69
3.19	Sidewall profiles of TRIP780 channels drawn with various draw-bead penetrations . . . . .	70
3.20	Sidewall profiles of DP980 channels drawn with various draw-bead penetrations . . . . .	71
3.21	Comparison of sidewall profiles for channels drawn with and without drawbeads . . . . .	72
3.22	Sidewall profiles of channels made from TRIP780 blanks sheared in the rolling and transverse directions, with shallow bead penetration (20%) and no drawbeads (DER=12mm) . . . . .	74
3.23	Comparison of sidewall profiles for channels drawn with various die entry radii and without drawbeads . . . . .	75
3.24	Location of surface strain measurements on the channel sidewalls	76
3.25	Thickness measurement of channel sections using an ultrasonic thickness device . . . . .	76
3.26	Specimen for uniaxial tension test designed according to ASTM-E8	78
3.27	Uniaxial tension test data obtained at the University of Windsor for TRIP780 and DP980 . . . . .	81
3.28	Plasticity curves for TRIP780 from uniaxial tests performed at University of Windsor, USSteel and a power law curve . . . . .	83
3.29	Plasticity curves for DP980 from uniaxial tests performed at University of Windsor, USSteel and a power law curve . . . . .	84
3.30	Engineering stress-strain curves for unloading elastic modulus of TRIP780 and DP980, performed at the Colorado School of Mines	85
3.31	Sample of estimating initial and unloading elastic modulus of TRIP780 and DP980 from stress-strain curves . . . . .	86
3.32	Multiple loading and unloading cycles to estimate saturated unloading elastic modulus of TRIP780 and DP980 . . . . .	89
3.33	Fitting analytical decay function to unloading elastic modulus of TRIP780 and DP980 . . . . .	90
3.34	Cyclic tension - compression tests of TRIP780 . . . . .	92
3.35	Cyclic tension - compression tests of DP980 . . . . .	93

---

4.1	Fitting bounding surfaces to experimental tension and compression data of DP980 . . . . .	97
4.2	Fitting bounding surfaces to experimental tension and compression data of TRIP780 . . . . .	98
4.3	Schematic representation of the finite element model for tension compression test . . . . .	99
4.4	Comparison of experimental tension and compression test results with isotropic hardening and YU models (Mat 125) for TRIP780 and DP980 . . . . .	100
4.5	Optimized simulations with Material type 125 for tension compression tests of TRIP780 and DP980 . . . . .	103
4.6	Correlation matrices between Mat125 parameters and curve mapping error response for TRIP780 and DP980 . . . . .	104
4.7	Finite element model of the channel draw forming in LS-DYNA	107
4.8	Comparison of predicted and experimental punch force results for DP980 with various material models . . . . .	114
4.9	Comparison of predicted and experimental punch force results for TRIP780 with various material models . . . . .	115
4.10	Comparison of experimental and predicted punch force results for TRIP780 with shallow beads using the YU model in ABAQUS and LS-DYNA . . . . .	116
4.11	Energy balance for TPSB case with various material models . .	118
4.12	Energy balance for TPSB case with various material models . .	119
4.13	Energy balance for TPSB case in ABAQUS - YU model . . . . .	120
4.14	Energy balance for DPSB case with various material models . .	121
4.15	Energy ratio for DPSB case with various material models . . . .	123
4.16	Comparison of predicted and experimental punch forces for TRIP780 and DP980 without draw beads and with DER=12 mm . . . . .	124
4.17	Comparison of predicted and experimental punch forces for cases without beads, DER=12mm and Mat 24 for various coefficients of friction . . . . .	125
4.18	Schematic illustration of sidewall comparison between simulated and experimental curves . . . . .	126
4.19	Comparison of simulated and experimental sidewall profiles for TRIP780 channels with shallow beads . . . . .	128
4.20	Comparison of simulated and experimental sidewall profiles for DP980 channels with shallow beads . . . . .	129

---

4.21	Comparison of simulated and experimental sidewall profiles for TRIP780 channels without beads and DER=12mm . . . . .	130
4.22	Comparison of simulated and experimental sidewall profiles for DP980 channels without beads and DER=12mm . . . . .	131
4.23	Simulated sidewall profiles for TPNB12 condition with various friction coefficients . . . . .	134
4.24	Maximum principal strain histories for an element on the sidewall of TPSB channel forming simulation . . . . .	137
4.25	Minimum principal strain histories for an element on the sidewall of TPSB channel forming simulation . . . . .	137
4.26	Shell thickness reduction (%) for TPSB and DPSB conditions . . . . .	138
4.27	Effective plastic strain distributions for TPSB and DPSB conditions . . . . .	139
5.1	Modified prediction of cyclic behaviour of TRIP780 sheet metal by the isotropic hardening law . . . . .	141
5.2	Prediction of the cyclic behaviour of TRIP780 and DP980 steels with the combined isotropic-linear kinematic hardening law . . . . .	142
5.3	Channel sidewall profiles for the TPSB and DPSB cases predicted with the YU model in ABAQUS and LS-DYNA and compared with the experimental results . . . . .	144
5.4	Prediction of the thickness along the channel section predicted with the YU model in ABAQUS for TRIP780 and DP980 . . . . .	145
A.1	FE model of crash forming a B pillar part from DP980 . . . . .	149
A.2	Plastic strain distribution of forming simulation of a B-pillar, using Mat37 . . . . .	149
A.3	Predicted sprungback B-pillar, using Mat37 model . . . . .	149

# List of Abbreviations and Symbols

AHSS	Advanced High Strength Steels
AKDQ	Aluminum-Killed Draw Quality steel
DP	Dual phase steel
NIP	Number of Integration Points
TRIP	TRansformation Induced Plasticity
YU	Yoshida - Uemori plasticity model
IH	Isotropic hardening
LK	Linear Kinematic hardening
NKH	Nonlinear Kinematic hardening
Mat 18	Power law isotropic hardening model
Mat 24	Piecewise linear plasticity model
Mat 36	3-Parameter Barlat plasticity model
Mat 37	Transversely anisotropic elastic plastic model
Mat 125	Kinematic hardening transversely anisotropic model
E	Elastic Modulus
$\bar{\sigma}$	Effective stress
$\sigma_{y0}$	Initial yield stress
$\alpha$	Back-stress tensor



# Introduction

---

## 1.1 Overview

The ongoing need for vehicle weight reduction and safety improvement has resulted in the use of advanced high strength steels (AHSS) such as Dual Phase (DP) and Transformation Induced Plasticity (TRIP) sheet metals (along with aluminum). The advanced performance of these steels in ductility and strain hardening characteristics provides an opportunity to stamp complex geometries and improve performance of automotive body in crash, ductility and strength while reducing the overall weight. This increased formability of AHSS materials is their main advantage over conventional HSS. However, specific material characteristics have increased the challenges encountered when forming parts made from such steels.

One of the main challenges in industrial sheet metal forming processes is to satisfy design specifications without causing defects such as splits, wrinkling, skid lines, surface distortion and springback. From these, the springback deformation is unavoidable for all sheet metals because this type of elastic recovery appears naturally as a result of the unbalanced stresses that develop in the part as well as through-thickness just after its removal from the die. Along with the increase in strength and formability of sheet metals, the occurrence of severe distortions like springback and side-wall curl also increases. These complex deformations are the most significant factors that change the shape of parts after forming and make it difficult to achieve the required dimensional accuracy for the final product. This can lead to a product in which loss of dimensional accuracy causes difficulties to

join the part in a sub-assembly or even a loss of function in downstream operations. Therefore tooling revisions during die design phase are required in order to provide formed parts of close tolerances. This necessitates accurate prediction of springback and sidewall curl specially for parts made of advanced high strength sheet metals.

Spring back is an undesirable change in shape that results from non-uniform deformation across a sheet metal when it is formed, while sidewall curl results from successive bending and straightening which occurs when the sheet metal is drawn over a die radius or through drawbead. Although springback is the more general term when referring to discrepancy between the shape of the fully formed part when it is still in the closed die and the unconstrained shape of a part, side-wall curl is a concern to manufacturers when forming certain groups of automotive parts such as rails and drawn parts, because of the difficulty to join non-flat surfaces.

Nowadays computer aided simulation tools based on finite element method are regularly employed in the design of stamping dies for sheet metal parts in the automotive industry. These computer tools allow the design engineer to investigate the process and material parameters controlling the material flow over the die surfaces. Nevertheless, the reliability of predicted formability and the accuracy of the estimated deformed geometry for a given stamped part depend on the computational modeling approach that is selected. Equally important is how fast the results can be obtained and implemented in the design stage (CPU time).

## 1.2 Sidewall curl and springback

Once a deformed sheet-metal part is removed from the dies in which it was formed, the elastic component of strain is recovered. The discrepancy between the fully loaded shape at the end of the forming stage and the unloaded configuration is called springback. A complex form of springback in sheet forming occurs when the sheet undergoes both bending and unbending deformations. The inside surface of the sheet will incur more tendency to compressive stresses while the outer more tendency

to tension. This phenomenon takes place when the sheet first makes contact with the tool surface (bending) and then leaves the tool surface and partially or completely loses its curvature (unbending) [43], and is referred to as “sidewall curl”. In such a bending and unbending situation, the deformation histories for both sides of the material are unlikely to be the same, resulting in curling.

Therefore sidewall curl is the curvature created in the sidewalls of a channel. Sidewall curl can cause difficulties when assembling mating parts such as rails and channel sections, since assembly requires tight tolerances for efficient spot welding. In channel forming, sidewall curl is superimposed on the more common type of springback which is sidewall opening. As shown in Fig.1.1.a, b & c, wall opening refers to the change in the angle between the two sides of a bend line compared to the as-formed angle whereas in wall curl a straight sidewall becomes curved. During forming, the sidewall is subjected to plastic bending under tension as it is drawn over a die or punch radius or through a draw bead [22]. The primary cause is uneven stress distribution or stress gradient through the thickness of the sheet metal. This stress is generated during the bending and unbending process.

Fig.1.2 describes the origins of this phenomenon when sheet metal is drawn over the die radius (a bending-unbending process). The deformation in side A changes from tension ( $A_1$ ) during bending to compression ( $A_2$ ) during unbending while the deformation in side B changes from compression ( $B_1$ ) to tension ( $B_2$ ) during bending and unbending. As the sheet pulls over the die radius into the sidewall, side A is in compression and side B is in tension although both sides may have similar amount of strains. Once the punch is retracted (unloading), side A tends to be stretched and side B to be compressed due to elastic recovery. This difference in springback between sides A and B would lead to a non-uniform stress distribution which is the source of sidewall curl.

For higher strength metals, the magnitude and difference in elastic recovery between sides A and B will be greater which will result in greater sidewall curl. The

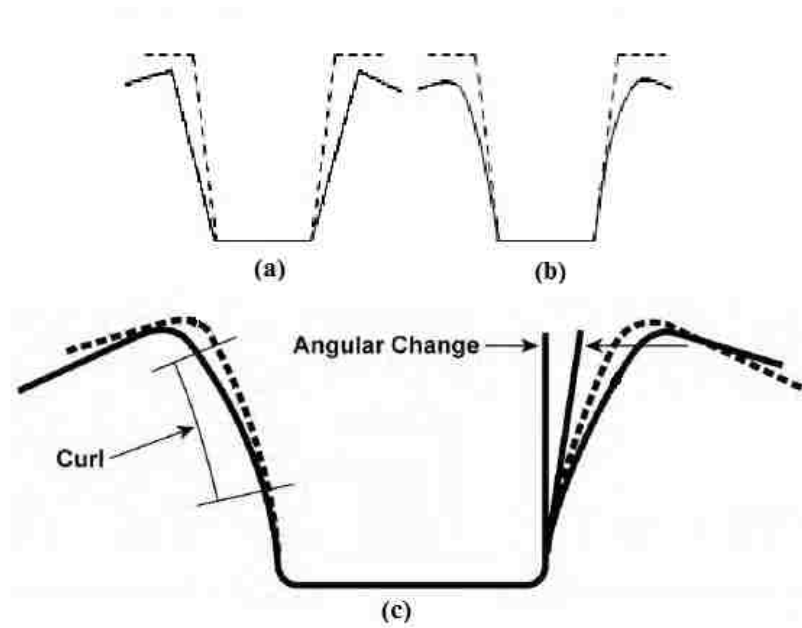


Figure 1.1: Different types of sidewall springback: a) wall opening, b) wall curl, [1]

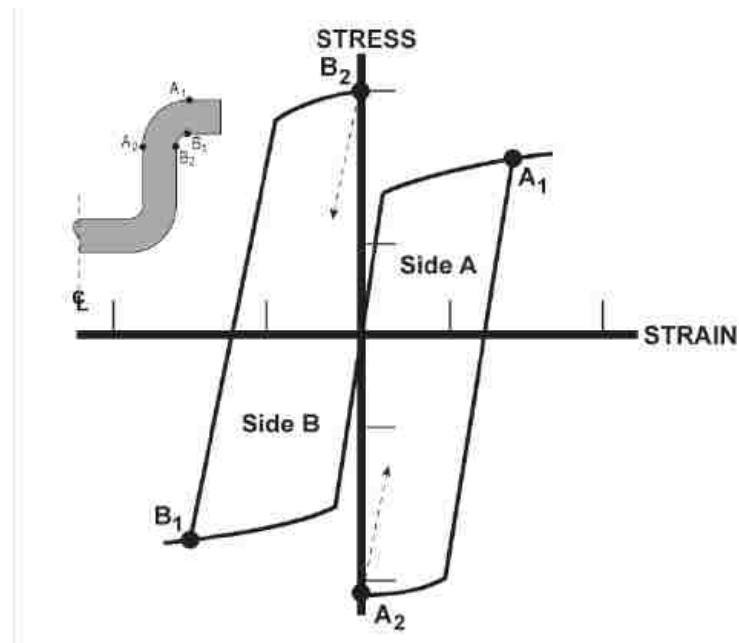


Figure 1.2: Origin and Mechanism of Sidewall curl, [1]

strength of the deformed metal depends not only on the as-received yield strength, but also on the work hardening capacity, which is one of the key differences between

conventional HSS and AHSS. In general, springback and sidewall curl experienced in AHSS parts is greater than what is seen in mild steel or HSLA (although not as great as aluminum) with higher strength-to-modulus ratios (Fig.1.3).

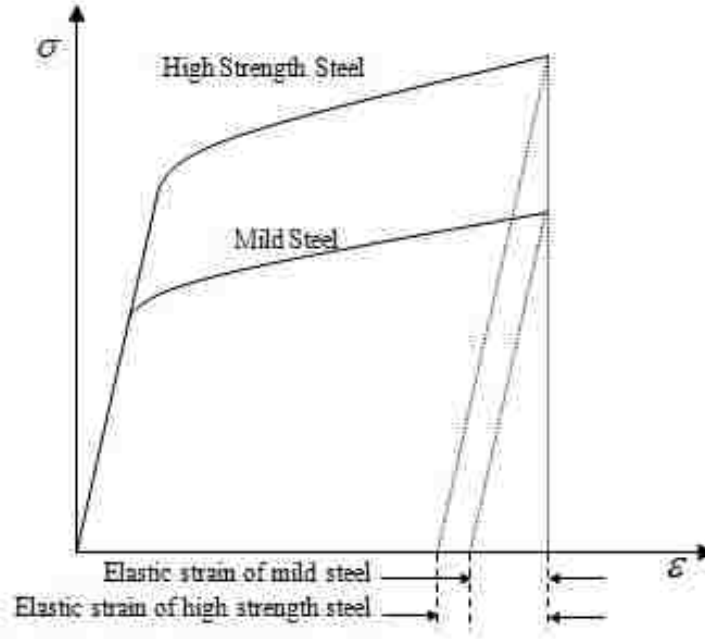


Figure 1.3: Elastic recovery comparison between AHSS and MS during unloading, [1]

### 1.3 Springback of Advanced High Strength Steels

Automotive steels can be classified in several different ways. One way is a metallurgical designation. Common designations include low-strength steels (interstitial-free and mild steels); conventional HSS (carbon-manganese, bake hardenable, high-strength interstitial-free, and high-strength, low-alloy steels); and the newer types of AHSS (dual phase, transformation-induced plasticity, complex phase, and martensitic steels). Additional higher strength steels for the automotive market include ferritic-bainitic, twinning-induced plasticity, hot-formed, and post-forming heat-treated steels (Fig.1.4).

Advanced high strength steels (AHSS) are defined as grades of steel with tensile

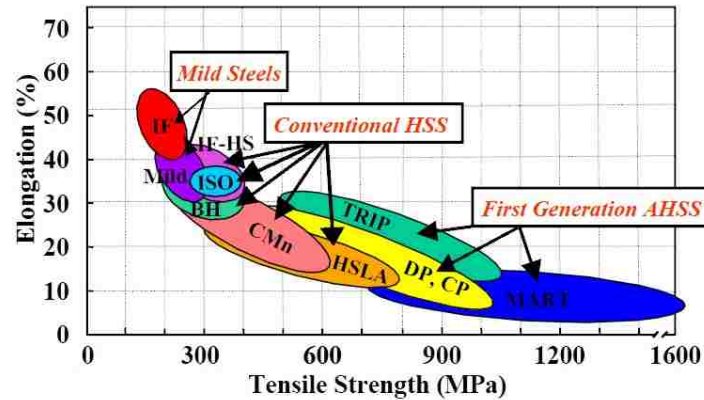


Figure 1.4: Schematic of AHSS steels compared to conventional HSS and mild steels, [1]

strength higher than 500 MPa and complex microstructures such as bainite, martensite, retained austenite, etc. and exclude the classical HSLA steels. The principal difference between conventional HSS and AHSS is their microstructure. Conventional HSS are single phase ferritic steels. AHSS are primarily multi-phase steels, which contain ferrite, martensite, bainite, and/or retained austenite in quantities sufficient to produce unique mechanical properties. Some types of AHSS have a higher strain hardening capacity resulting in a strength-ductility balance superior to conventional steels. Other types have ultra-high yield and tensile strengths and show a bake hardening behaviour.

The microstructure of DP steels is composed of ferrite and martensite, while the microstructure of TRIP steels is a matrix of ferrite, in which martensite and/or bainite and more than 5% retained austenite exist. DP steel has good formability due to high volume fraction of ferrite with high ductility and has good spot weldability due to the small amount of alloying elements. TRIP steel has extremely high elongation and n-values relative to DP grades providing opportunities for accommodating complex part geometries at strength levels not possible with the equivalent DP strength, but present greater challenges in weldability due to higher alloying content than DP grades. A comparison between three types of steels with approximately similar yield strength can be seen in Fig.1.5, where TRIP has a lower initial work hardening rate

than DP, but the hardening rate persists at higher strains whereas that of DP begins to diminish.

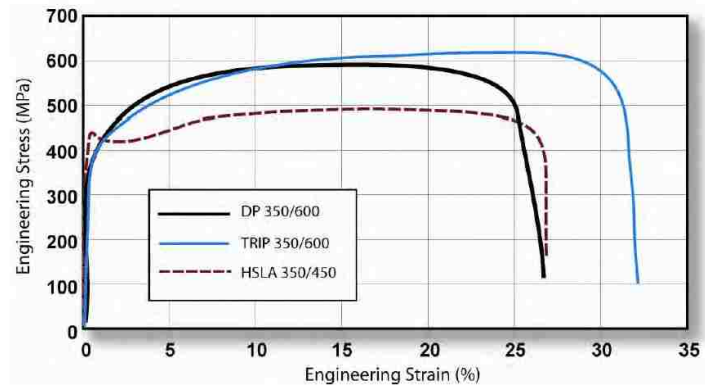


Figure 1.5: TRIP350/600 with a greater elongation than DP350/600 and HSLA350/450, [1]

The terminology of WorldAutoSteel organization was used here for identification of steel grades, i.e. by metallurgical type, minimum yield strength (in MPa), and minimum tensile strength (in MPa).

The introduction of AHSS materials have created additional challenges to the springback problem. Many reports state that springback and sidewall curl are much greater for AHSS than for traditional HSS. However, a better description would be that the springback of AHSS is different from springback of HSS steels and knowledge of different mechanical properties and material models is required. An example of this difference is shown in Fig.1.6 where two channels were made sequentially in a draw die with a post on a pad to attain part print for HSLA 350/450 steel. The strain distributions between the two parts were very close with almost identical lengths of line. However the stress distributions were very different because of the mechanical property differences between DP and HSLA steels.

The difference in strain hardening between conventional HSS and AHSS explains how the relationship between angular change and sidewall curl can alter part behaviour. Fig.1.7 shows the crossover of the true stress - strain curves when the two steels are specified by equal tensile strengths. The AHSS have lower yield strengths



Figure 1.6: Two channels made sequential in the same die, [1]

than traditional HSS for equal tensile strengths. At lower strain levels usually encountered in angular change at the punch radius, AHSS have a lower level of stress and therefore less springback.

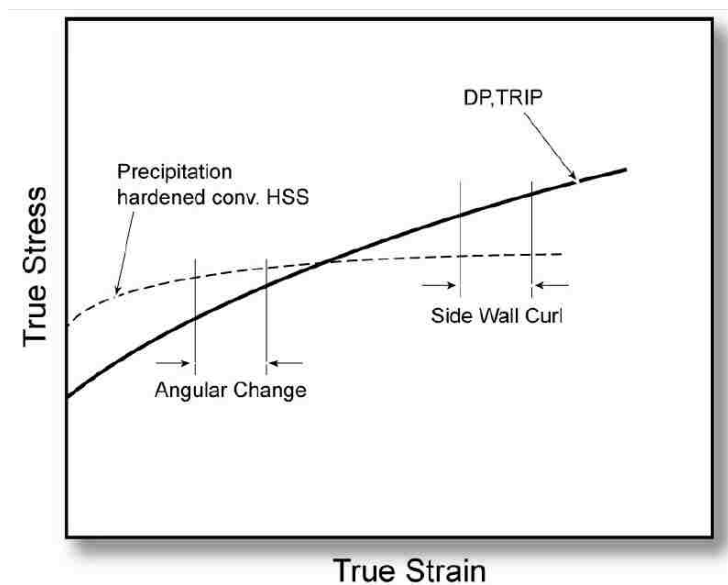


Figure 1.7: Elastic recovery comparison between AHSS and MS during unloading, [1]

Sidewall curl is a higher strain event because of the bending and unbending of the steel going over the die radius and possible drawbeads. For the two stress-strain curves shown in Fig.1.7, the AHSS reaches a higher stress level with increased elastic stresses. Therefore the sidewall curl is greater for AHSS as also compared in Fig.1.8.



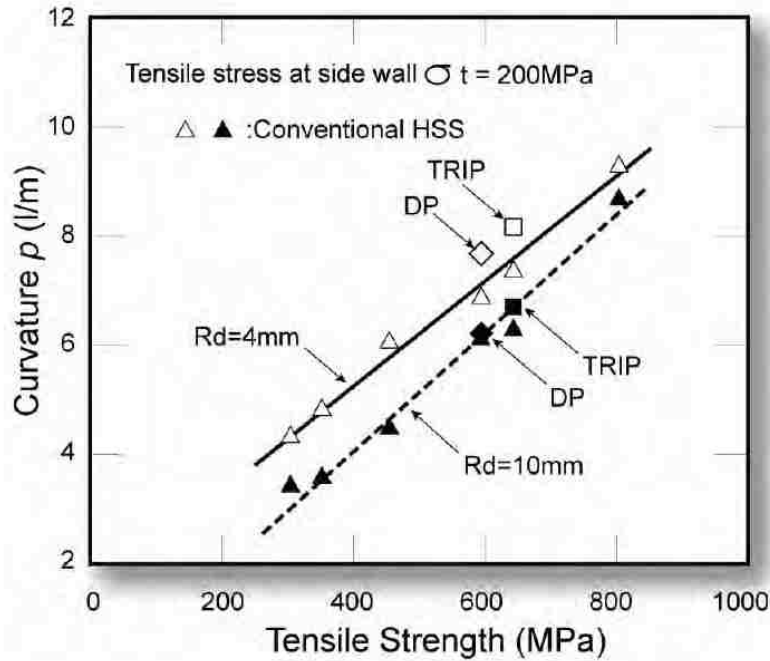


Figure 1.8: The AHSS have greater sidewall curl for equal tensile strength steels, [1]

These phenomena are dependent on many factors, such as part geometry, tooling design, process parameters and material properties. However, the high work-hardening rate of DP and TRIP steels causes higher increase in the strength of the deformed steel for the same amount of strain. Therefore any differences in tool build, die and press deflection, location of pressure pins and other inputs to the part can cause varying amounts of springback - even for completely symmetrical parts.

## 1.4 Prediction and Compensation

As stated, forming of a part creates elastic stresses unless the forming is performed at a higher temperature range where stresses are relieved before the part leaves the die. Therefore some form of springback correction is required to bring the part back to design intent. Several approaches have been proposed to control springback.

The first approach is to apply an additional process that changes undesirable

elastic stresses to less damaging elastic stresses. One example is a post-stretch operation that reduces sidewall curl by changing the tensile-to-compressive elastic stress gradient through the thickness of the sidewall to all tensile elastic stresses through the thickness. Another example is over-forming panels and channels so that the release of elastic stresses brings the part dimension back to design specifications instead of becoming undersized. However, the maximum tension in the sheet is limited by the fracture strength of the sheet material. Moreover this stretch-forming technique is generally not sufficient to eliminate springback. Some studies also suggest using a variable blank holder force during the punch trajectory. In this method, the blank holder force is low from the beginning until almost the end of the forming process and then it is increased at the end of the process such that a large tensile stress is applied to the sheet material.

A second approach is to modify the process and/or tooling to reduce the level of elastic stresses actually imparted to the part during the forming operation. An example would be to reduce sidewall curl by replacing sheet metal flowing through draw beads and over a die radius with a simple 90 degree bending operation.

A third approach for correcting springback problems is to modify the product design to resist the release of elastic stresses. Mechanical stiffeners are added to the part design to lock in the elastic stresses to maintain desired part shape.

Most of these approaches are applicable to all higher strength steels, however the very high flow stresses encountered with AHSS make springback correction high on the priority list [1]. In order to successfully manufacture a sheet metal part from AHSS material with the desired shape and performance, an extensive knowledge about the influence of various parameters is needed. Nowadays, to establish this knowledge base, experimental try-outs and numerical simulations are used. Computer simulation, based on the finite element (FE) method, is a powerful tool that gives the possibility to observe effects of changing process parameters prior to the

actual tool manufacturing. However, the key to success is to use material models which can describe the behaviour of such materials sufficiently accurate to quantitatively predict springback/sidewall curl during the design phase. Assuming that springback can be predicted accurately, a “backward” analysis is still required to work from these results back to an optimized die design (Fig.1.9).

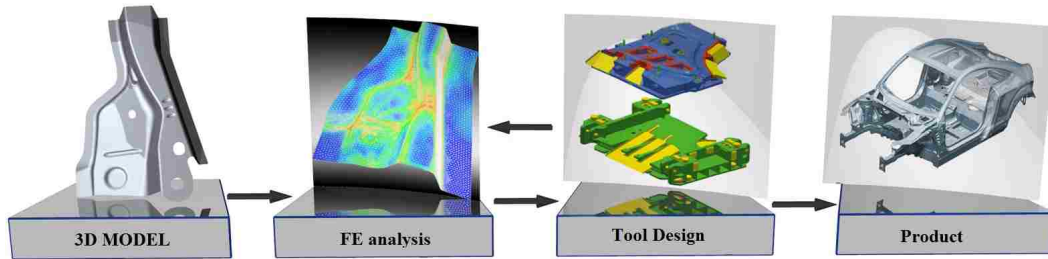


Figure 1.9: Design process schematic, [4]

## 1.5 Objective and outline of thesis

The main objective of the current study was to evaluate the applicability of different material models which are already developed for FE solvers like ABAQUS and LS-DYNA (DYNAFORM) for stamping parts made of advanced high strength steels like TRIP780 and DP980. For evaluation purposes, a channel draw die with adjustable penetration drawbead inserts and several die entry radii - previously presented as Benchmark #3 (BM3) at the NUMISHEET 2005 International Conference [27] - was used to form U-shaped channel sections that exhibit various levels of sidewall curl. The severe deformation in the drawbead and over the die radius provided a cyclic loading scenario as a combination of bending, unbending and reversed bending on the benchmark. The complex contact condition also presented a challenge for evaluation of the contact model.

Numerical simulations of the channel draw process were carried out using different material models to determine how accurately they can predict the sidewall curl for both grades of AHSS materials, i.e. TRIP780 and DP980. The input pa-

parameters for these constitutive models were separately determined for both grades of steel through a series of laboratory experiments and subsequent analysis.

The present thesis is composed of five chapters. The first chapter provides a brief introduction to the general terms used in this study as well as its organization. A review of the literature related to the prediction of springback phenomena in general and sidewall curl in particular are presented in the second chapter along with detailed explanations about the candidate material models for the AHSS panels, i.e. TRIP780 and DP980. Chapter three covers the experimental studies performed for the material characterization tests as well as channel draw forming experiments. Numerical analysis of these experiments are explained in chapter four. Final discussions and conclusions of this study are given in chapter five.

# Material Models

---

## 2.1 Introduction

Metal forming researchers have investigated the prediction and compensation of springback and sidewall curl since the early 1980's. Different approaches such as analytical, semi-analytical and finite element methods have been extensively employed in these studies to quantitatively analyze the problem. FEM is a relatively time-consuming method whereas analytical solutions can instantaneously provide a description of the deformation mechanism based on a theoretical model. However, analytical solutions are limited to simple applications and often only provide qualitative estimation of springback.

It has been shown that many process variables such as friction, temperature, variations in the thickness and mechanical properties of the incoming sheet metals along with numerical parameters such as material model, element type and size, integration algorithms, contact definition and convergence criteria, etc. affect the accuracy and validity of the solution. Moreover, complex strain histories and highly nonlinear deformation of the material during the forming process add to the difficulty of predicting springback/sidewall curl. Therefore, it is important to critically review related studies before selecting the appropriate solution method for the problem.

Results of the most recent studies on analytical and numerical solutions for springback and sidewall curl problem are summarized in the rest of this chapter. Special attention is given to the constitutive material models used to describe the deformation behaviour of sheet metals, and in particular to models for cyclic loading

and unloading of AHSS material which are necessary to accurately predict sidewall curl. The most widely used approach is to carry out computer simulations that rely on advanced material models to compute the stress distribution in the part and the final geometry of the part after unloading.

## 2.2 Literature review

### 2.2.1 Early studies

Davies (1984, [15]) proposed a simple experimental apparatus to examine the sidewall curl that occurred in low-carbon, HSLA 50 and 80 (with ultimate strengths of 450 and 620 MPa), and DP-80 (850 MPa ultimate strength) steels. He found that by imposing a plastic deformation, the curl can be eliminated as a result of the removal of the nonuniform distribution of residual stresses. Hayashi and Tagagi (1984, [29]) performed a series of experiments to investigate the effects of process parameters on the formation of sidewall curl for high-strength steels. They also tried to explain the deformation behaviour by stress/strain paths of different areas of the blank. Liu (1988, [37]) obtained quantitative relationships between restraining force and shape deviations, such as springback and side wall curl, in flanged channels made of AKDQ and high strength steels. It was observed that shape deviation is greatly reduced if the applied restraining force is beyond the yield strength of the material. However, due to the restriction of die entrance and punch corners, this condition cannot be readily achieved in the conventional bead system as sidewall fracture intervenes. Therefore an intermediate restraining process was proposed to form high quality flanged channels in one single operation through displacement control, once the properties of the material are known.

In another study, Ayres (1984, [2]) investigated a process developed by GM research fellows, known as ‘SHAPESET’, to reduce curl springback for a variety of high-strength steel. In the SHAPESET process, the steel is first bent to shape without drawbeads and without tension, which creates severe sidewall curl. This

sidewall curl is then removed in a second strike or stretch operation with drawbeads. Ayres's study showed that SHAPESET can reduce sidewall curl springback in straight rails made of dual phase steels (580, 670 MPa ultimate strength), by a factor of ten, because a greater wall load could be applied without splitting. Although the SHAPESET process was claimed not to be sensitive to the strength level of steel, in a recent work at Auto/Steel Partnership, Michigan, Bzdok (2005, [5]) reported that DP600 MPa and lower strength steels were the only materials that could be stretched with a two-break lockstep in the SHAPESET process. Higher-strength materials (DP780 and DP980) required a four-break lock step for effective stretch results, as shown in Fig.2.1.

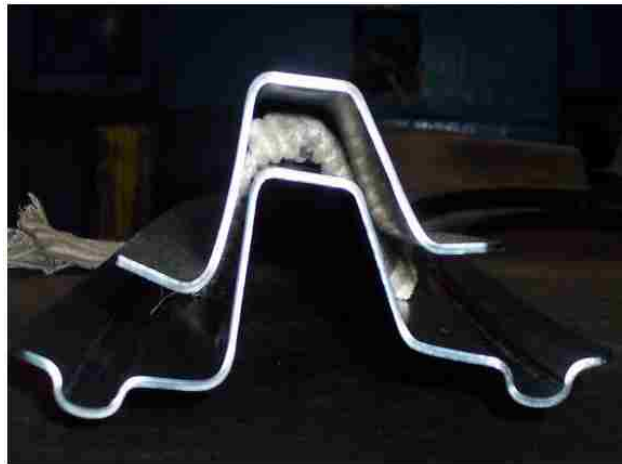


Figure 2.1: Effect of stretching in SHAPESET process, [5]

A simple theory for side-wall curl, was proposed by Thompson and Ellen (1985, [51]), which is based on the springback of a strip subjected to bending and straightening, and saturates the strain-hardened plastic moment in the strip. Kim and Thomson (1989, [33]) conducted a thorough literature review on both springback and side-wall curl up to that time. Later, the finite element method was employed by Tang (1987, [49]) for plane strain and axisymmetric parts without considering the contact problem and compared with experimental results. Taylor et al. (1995, [50]) used ABAQUS implicit and explicit finite-element modules to simulate NUMI-

FORM'93 benchmark problems and compared the results.

Chu (1991, [12]) analyzed the effects of restraining force on the springback and side-wall curl using an isotropic-kinematic hardening rule, and the significance of individual parameters on general springback phenomena was clearly identified. Pourboghraat and Chu (1995, [43]) made use of moment-curvature relationships derived for sheets undergoing plane-strain stretching, bending and unbending deformations, and employed the membrane finite element solutions to calculate the springback and side-wall curl in 2-D draw bending operations (Fig.2.2).

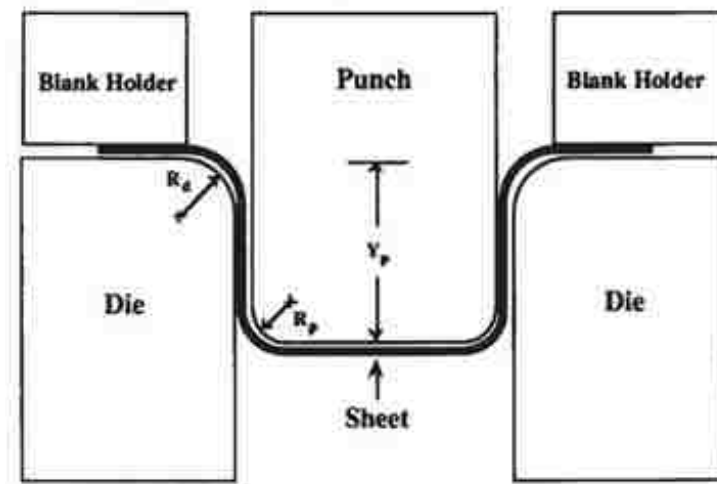


Figure 2.2: A schematic diagram of the 2-D draw bending operation, [43]

### 2.2.2 Analytical solutions

Cao and Buranathiti (2004, [6]) developed an analytical model for springback prediction of a straight flanging process (Fig.2.3), by calculating the bending moment under plane-strain conditions. They used the model to predict springback for a few HSS materials and compared the predicted results reported by other researchers.



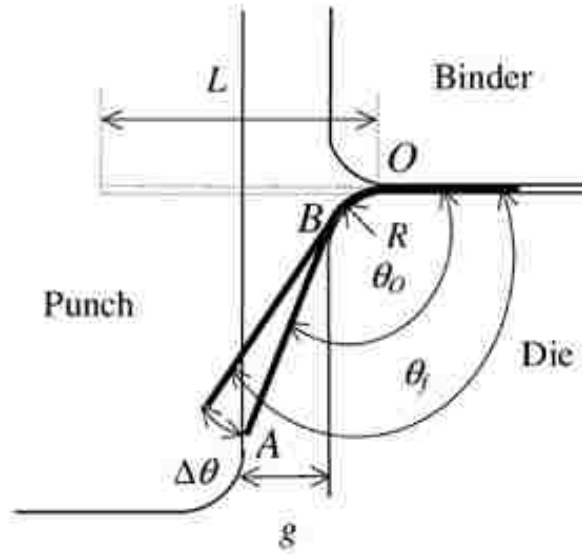


Figure 2.3: Schematic of straight flanging process, [6]

Chen and Tseng (2005, [10]) proposed a theoretical model for prediction of sidewall curl occurring in the forming of a flanged channel subjected to bending, sliding, and unbending. By numerically solving the governing equations, the amount of sidewall curl was calculated from the stress distribution through the sheet thickness and validated by experimental and finite element simulations. Lee et. al. (2007, [35]) developed a semi-analytic hybrid method to predict springback in a 2D draw bend test under plane strain conditions which superposed bending effects onto a membrane element formulation (Fig.2.4). This method was also shown to be useful for analyzing the effects of various process parameters such as the amount of bending curvature, normalized back force and friction, as well as material property effects such as hardening behaviour including the Bauschinger effect and yield surface shapes. Good agreement was reported for a dual phase steel compared to sprungback shapes. Springback was found to decrease by increasing  $\frac{R}{t}$ , restraining force and friction between sheet and tools.

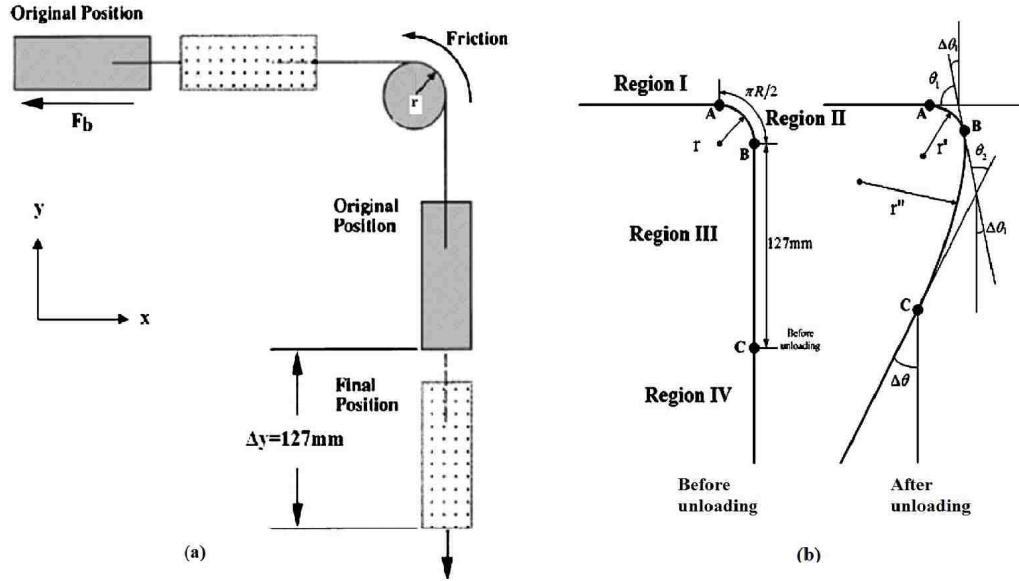


Figure 2.4: (a) Geometry of the draw bend test with, (b) deformed shape before and after springback, [35]

An analytical model of elasto-plastic bending under tension followed by elastic springback was proposed by Wagoner and Li (2007, [52]) to address the controversial problem of the number of through-thickness integration points (NIP) for shell elements. Using this model, guidelines for choosing NIP to assure a specified springback accuracy, varying with  $\frac{R}{t}$ , sheet tension and the required confidence limit, were presented. The relative springback error was shown to oscillate and in some cases even more than 51 integration points were required. Zhang et al. (2007, [62]) developed an analytical model to predict springback and sidewall curl in sheets bent in a U-die under plane-strain conditions (NUMISHEET'93 benchmark). They used Hill's 1948 yield function and took into account the effects of deformation history (by using three hardening rules: kinematic, isotropic and combined hardening), the evolution of sheet thickness and the shifting of the neutral surface.

In another study, Yi et al. (2008, [55]) developed an analytical model based on differential strains after relief from the maximum bending stress for six different deformation patterns. They used each deformation pattern to estimate springback by

the residual differential strains between outer and inner surfaces after elastic recovery, while other analytical models were based on elastic unloading from a bending moment. Such residual differential strain model only required the stress state on the outer and inner surfaces rather than through the whole thickness of the sheet metal. Moon and others (2008, [41]) developed a model based on the moment-curvature relationship during stretch-bend sheet forming operations and verified it with the sidewall curl experimentally measured after deformation of a strip subject to bending-under-tension.

A review of the aforementioned studies showed that although the use of analytical models is advantageous because of their simplicity, the application of these models is limited to simple geometries.

### 2.2.3 Numerical studies

Many researchers have used finite element analysis to numerically simulate sidewall curl during sheet metal forming operations. Such FE analyses consist of two main steps. Firstly, an explicit incremental or implicit incremental-iterative FE method is applied in order to simulate the forming process that includes the blank and the tooling. Secondly, the springback deformation is simulated with the static implicit FE approach based on the formed geometry along with the forming stress distribution as the baseline input. The accuracy of such simulations depends not only on the forming conditions (friction, tool and binder geometry), but also on the numerical parameters such as element type, in-plane mesh size and the number of through-thickness integration-points, as well as the constitutive model that governs the behaviour of the deformable sheet [25].

Yang and Lee (1998, [54]) used the Taguchi method to study numerical factors affecting springback of a mild steel after the U-bending draw test in which drawbeads were not used (Numisheet'93). Through an ANOVA study, the mesh size was found to have the strongest effect on the accuracy of springback prediction with respect to

damping and penalty parameters and punch velocity. Samuel (2000, [45]) proposed a numerical model based on the “updated Lagrangian” formulation to calculate springback and sidewall curl in a plane-strain stretch/draw sheet forming using the MARC FE package. Both the experimental data and the theoretical 2D model suggested that in draw bending, sidewall curl decreases with the die radius but also depends greatly on blank-holder force.

Al Azraq (2006, [3]) studied a simple channel profile after springback using the AUTOFORM incremental code for DP600 and TRIP800 materials. The springback was shown to increase with angular variation of the channels but for profiles with the same angle, TRIP 800 showed more vertical displacement than DP 600. Chung et. al. (2005, [13]) formulated a modified Chaboche-type combined Isotropic-Kinematic hardening law which accounted for the Bauschinger effect and transient behaviour, using Yld2000-2d under plane stress condition. Comparisons of simulations and experiments were in good agreement for the unconstrained cylindrical bending, 2-D draw bending and the modified industrial part (the double-S rail) for two Aluminum sheets and DP steel (Fig.2.5a, b, c).

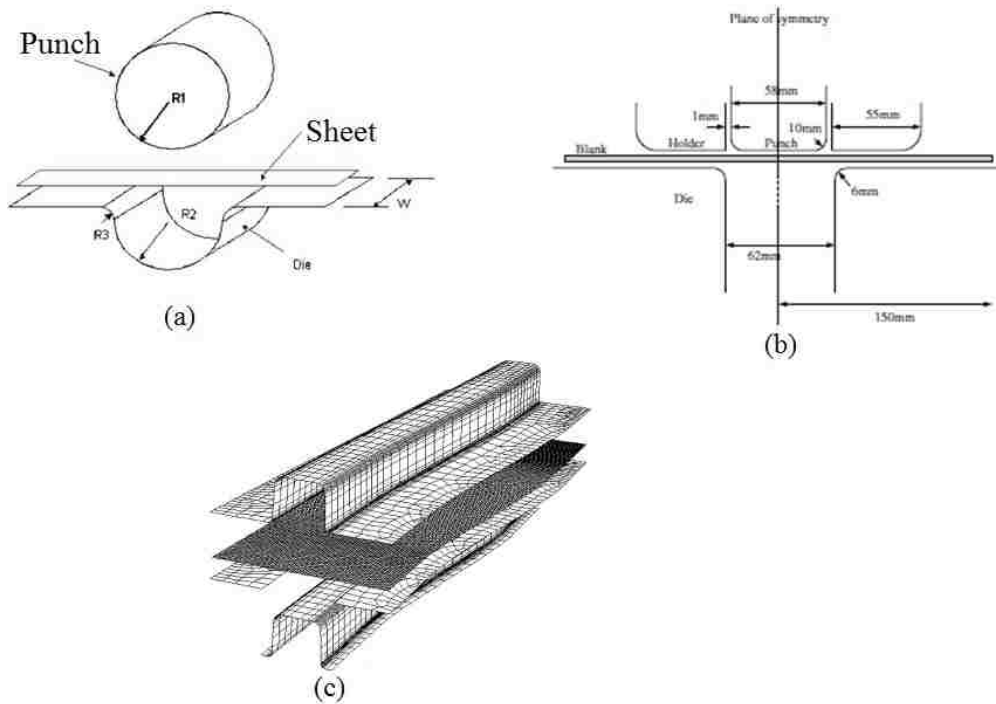


Figure 2.5: Schematics of (a)cylindrical bending test, (b)2-D draw bending test, (c)double-S rail, [13]

The influence of low-strain deformation behaviour on curl and springback in advanced high strength steels was assessed by Matlock et. al. (2007, [39]) using a bending-under-tension test apparatus. A non-linear relationship was found between curl height and back tension, though it might be approximated as linear for industrial purposes. The curl also depended on the low-strain deformation characteristics of the material. The TRIP590 material had less curl compared to a dual-phase steel of similar initial thickness and tensile strength at back tensions ranging from 15 to 45% of the sheet tensile strength.

Later, Aydin (2008, [31]) implemented the Yoshida-Uemori (YU) material model in LS-DYNA user material interface and used it for analysis of channel draw tests with various die radii for several grades of high strength steels. In order to detect the springback accuracy of this model, the results were evaluated with LS-DYNA

standard material models like Mat36 and Mat103. This study showed that the YU model is the most reliable and also the most expensive model to detect the springback of high strength steels. Also it was not possible to obtain a unique set of parameters from different characterization tests (for example from tension-compression or bending-unbending).

Firat (2008, [21]) presented a rate dependent anisotropic plasticity model accounting for the Bauschinger effect that was used in a FE analysis of the Numisheet'93 U-channel benchmark as well as an automotive part made of HSLA 350. Comparison of FE results using both an isotropic hardening model and his proposed model showed similar strain and thickness predictions but significant differences in residual stresses and final part geometry.

Recently, Taherizadeh et. al. (2009, [48]) predicted the springback of Numisheet 2005 Benchmark#3 with different material models using the commercial finite element code ABAQUS and four different drawbead penetrations for AKDQ-DP600-HSLA50-AA6022/T43. Later Ghaei and Green (2010, [26]) used the return mapping procedure to implement the YU two surface model in ABAQUS for arbitrary yield functions. As an example, Yld2000-2d and Hill48 yield functions were developed in the subroutines and were used to simulate springback of the Numisheet BM3 U-channel for the same material types studied by Taherizadeh. A comparison of the experimental and predicted channel sidewall profiles showed that the YU model improves the springback prediction compared to the isotropic hardening model or the combined isotropic-nonlinear kinematic hardening model.

#### 2.2.4 Constitutive material models

It has often been observed that the FE springback/sidewall curl predictions are not be always accurate and the shape distortions estimated for some industrial applications have been notably erroneous. The inaccuracy of springback prediction becomes even more significant when it comes to high strength steels. An inves-

tigation of the FE springback predictions for the representative conditions in the previous studies indicated that the discrepancies cannot be explained on the basis of variability of the input parameters or numerical factors alone and the plasticity models employed in the FE analyses significantly influence the predicted deformation [24] & [21].

It is well known that a phenomenological plasticity model is composed of : a yield condition, a plastic work hardening law and a model of degradation of elastic stiffness due to plastic straining. In classical plasticity, the yield function represents a convex yield surface in stress space, which limits the elastic range of materials. The proper measurements and descriptions of the initial yield stress surface and its evolution are essential for the constitutive law in plasticity. Since the yield surface and, especially, its evolution are difficult to measure experimentally, the isotropic hardening of the initial yield surface is often assumed in the classical plasticity. Under this assumption, the initial yield surface expands radially (or proportionally) in stress space during plastic deformation. This assumption is reasonably effective to predict plastic deformations, especially when the deformation of material elements is approximately monotonous and proportional (Fig.2.6).

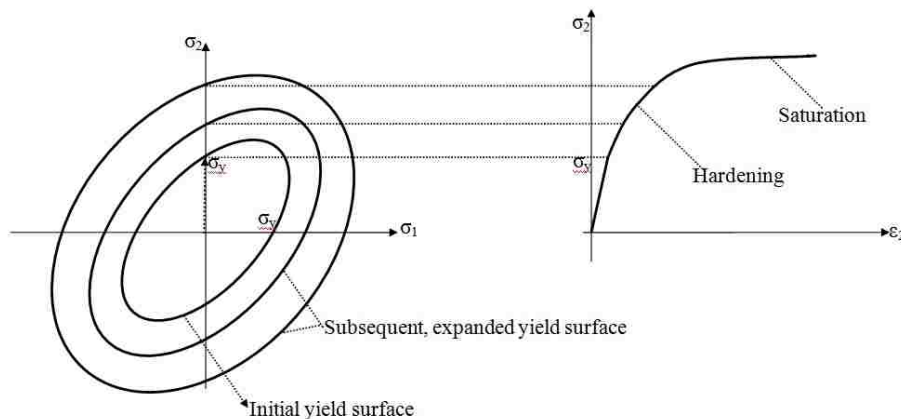


Figure 2.6: Isotropic hardening: the yield surface expands with plastic deformation, according to the work hardening described by the uniaxial stress-strain curve, [16]

For isotropic hardening, the yield function equation can be written as:

$$f(\sigma, p) = \bar{\sigma} - \sigma_y(p) = 0, \quad (2.1)$$

where  $\bar{\sigma}$  is the effective stress,  $p$  is the accumulated effective plastic strain, and  $\sigma_y(p)$  is the yield stress. Many functions could be written for  $\sigma_y(p)$ , for instance one might be:

$$\sigma_y(p) = \sigma_{y0} + R(p),$$

in which  $\sigma_{y0}$  is the initial yield stress and  $R(p)$  is the isotropic hardening function which is commonly expressed as:

$$\dot{R}(p) = b(Q - R)\dot{p}$$

where  $b$  and  $Q$  are material constants, creating an exponential shape to the uniaxial stress-strain curve which saturates at large plastic strains. The initial condition  $R(0) = 0$ , gives:

$$R(p) = Q(1 - e^{-bp}) \quad (2.2)$$

Therefore in isotropic hardening  $Q$  is the saturated value of  $R$  and the saturation stress is  $(\sigma_{y0} + Q)$ . Constant  $b$  determines the rate at which saturation is achieved (Fig.2.6).

If material elements undergo non-monotonous deformations, such isotropic hardening might not be so effective, even though deformations are approximately proportional. When sheet parts are removed from tools after forming, material elements experience elastic unloading and springback. During this reverse loading, material elements usually demonstrate the Bauschinger effect, which can be described as a translation of the yield surface. The Bauschinger effect is normally associated with



conditions where the yield strength of a metal decreases when the direction of strain is changed. It is a general phenomenon found in many polycrystalline metals. When the yield surface is assumed to expand uniformly in isotropic hardening, the yield stress in the reverse loading is predicted to be equal to that in forward loading, but this is not often the case. Therefore, isotropic hardening is not able to describe the Bauschinger effect in reverse loading.

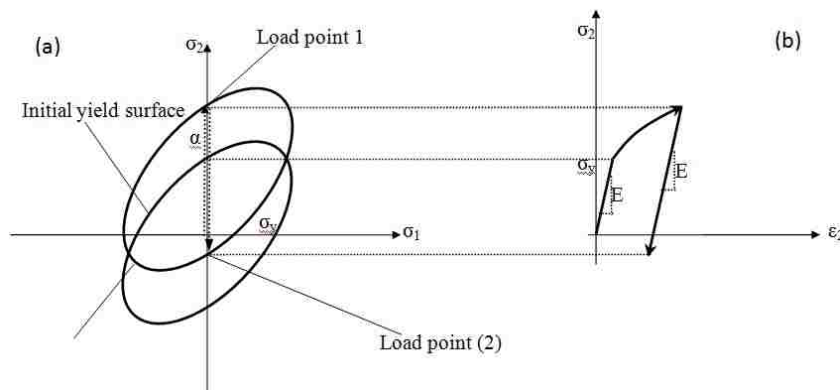


Figure 2.7: Kinematic hardening showing (a) the translation, and (b) the resulting stress-strain curve with shifted yield stress in compression, [16]

Assuming the initial yield surface to translate in stress space without changing its shape and size during plastic deformation is another way to model the evolution of the yield surface; this is called kinematic hardening. In order to reproduce the Bauschinger effect, a linear kinematic hardening model was first proposed by Prager (1956) and later modified by Ziegler (1959). Assuming kinematic hardening, the yield surface equation can be written as:

$$f(\boldsymbol{\sigma} - \boldsymbol{\alpha}) - \sigma_y = 0, \quad (2.3)$$

where  $\boldsymbol{\alpha}$ , called the *backstress tensor*, is a variable in the stress space and determines the location of the centre of the yield surface. As shown in Fig.2.7, the elastic region predicted by kinematic hardening, when unloading starts at point (1) and the material deforms elastically until point (2), is smaller than what is predicted

by isotropic hardening. The evolution of the backstress tensor can be defined by various functions. Prager proposed a linear kinematic hardening rule:

$$d\boldsymbol{\alpha} = \frac{2}{3}cd\boldsymbol{\varepsilon}$$

where  $c$  is a material constant. Ziegler modified Prager's rule according to the following equation:

$$d\boldsymbol{\alpha} = d\mu(\boldsymbol{\sigma} - \boldsymbol{\alpha}), \text{ where } d\mu > 0.$$

and  $d\mu$  also depends on the material. Classical isotropic hardening and Prager's or Ziegler's linear kinematic hardening models provide a reasonable description of the hardening properties of materials, for the case of proportional loading where the load is increasing monotonically and no unloading occurs.

In order to describe the expansion and translation of the yield surface during plastic deformation, the combination of isotropic (Fig.2.8) and kinematic hardening (Fig.2.9) is also commonly used. The combined isotropic-kinematic hardening constitutive law based on the modified Chaboche model [13] is given by:

$$f(\boldsymbol{\sigma} - \boldsymbol{\alpha}) - \bar{\sigma}_{iso} = 0, \quad (2.4)$$

where  $\boldsymbol{\alpha}$  is the back stress for the kinematic hardening and  $\bar{\sigma}_{iso}$  is the effective stress related to the isotropic hardening. In the Chaboche model, the back stress increment is composed of two terms,  $d\boldsymbol{\alpha} = d\boldsymbol{\alpha}_1 - d\boldsymbol{\alpha}_2$  to differentiate the transient hardening behaviour during loading and reverse loading.

Recent experiments in cyclic loading have revealed that the material responses under this loading condition are much more complex than under monotonic loading and cannot be described by the aforementioned isotropic, kinematic or combined hardening rules. The following phenomena have been observed during cyclic plastic deformation of sheet metals (mild steels and dual phase steels) [25]:

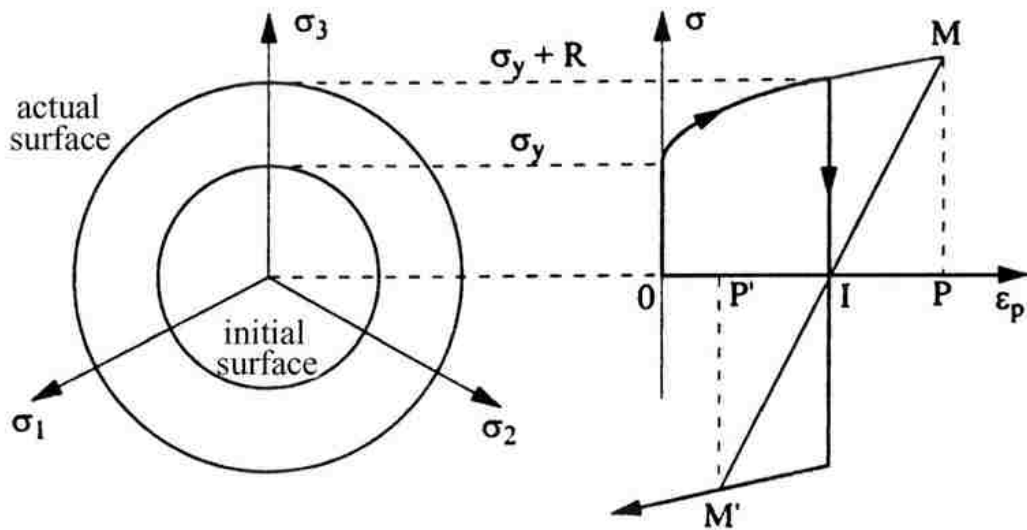


Figure 2.8: Schematics of the isotropic hardening. Left: in the deviatoric plane; right: the stress vs. plastic strain response, [8]

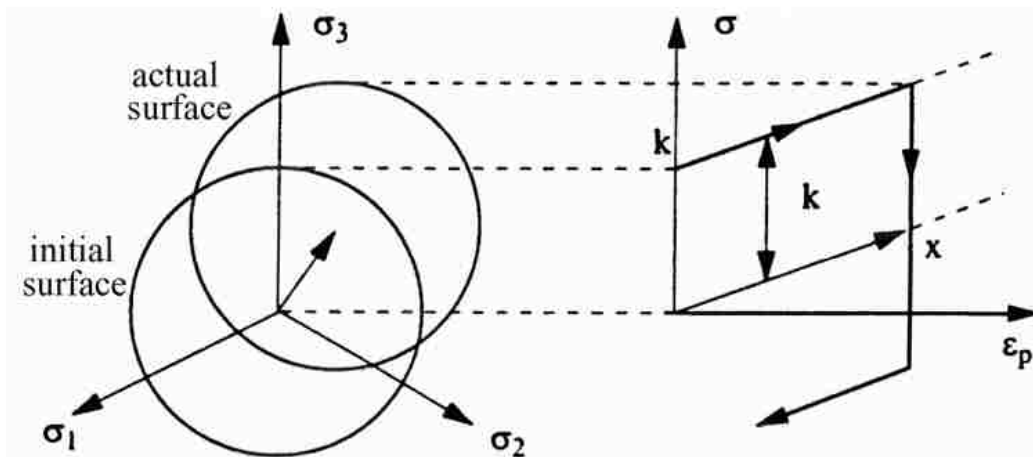


Figure 2.9: Schematics of the linear kinematic hardening. Left: in the deviatoric plane; right: the stress vs. plastic strain response, [8]

- Transient Bauschinger behaviour characterized by early re-yielding and a smooth elastic-plastic transition
- Abnormal shapes of reverse stress-strain curves due to work-hardening stagnation caused by dissolution of dislocation cell walls during reverse loading.

- Decrease of elastic modulus during unloading as the plastic strain increases and finally saturates to a particular value after large plastic strains
- Permanent softening appears after rapid changes of work-hardening rate in reverse plastic deformation.

Therefore in order to perform an accurate simulation of such a sheet metal forming process, it is necessary to have an appropriate constitutive model, which can consider the phenomena that occur during cyclic loading and unloading of such sheet metals (Fig.2.10).

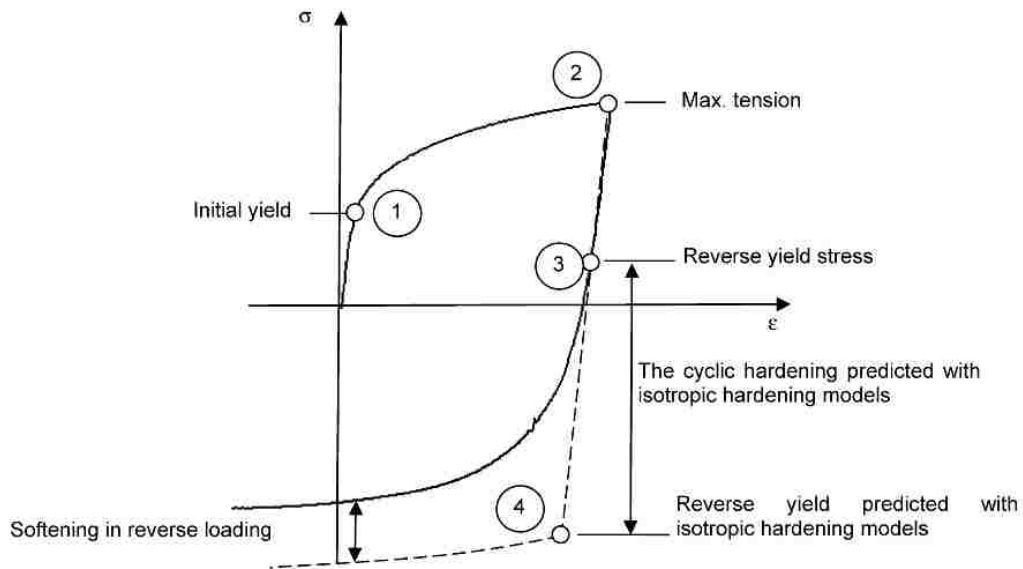


Figure 2.10: Schematic showing the stress-strain response with and without Bauschinger effect during forward and reverse loading paths, [21]

Within the last half-century some models have been proposed to meet the challenge. The most important ones are the multisurface model proposed by Mroz (1967), the two-surface model by Dafalias and Popov (1976), the nonlinear kinematic hardening model initiated by Armstrong and Fredrick (1966) and then developed further by Chaboche (1977) and the Endochronic theory proposed by Valant (1971) and developed further by Watanabe and Atluir (1986) [32].

Armstrong and Frederick [23] proposed the nonlinear kinematic hardening model in order to capture the transient behaviour curve during reverse loading:

$$d\boldsymbol{\alpha} = \frac{2}{3}cd\varepsilon^p - \gamma\boldsymbol{\alpha}dp, \quad (2.5)$$

where  $c$  and  $\gamma$  are two material constants, and  $p$  is the accumulated effective plastic strain. Later, Chaboche (1986, [9]) modified the Armstrong-Frederick nonlinear kinematic model to better reproduce the transient behaviour and ratcheting in fatigue. Ratcheting is a very important factor in the design of components subject to cyclic loading in the inelastic domain. The amount of plastic strain can accumulate continuously with an increasing number of cycles and may eventually cause material failure. For better modeling of cyclic deformations, Yoshida et al. (2002, [60]) developed two constitutive models called IH+NKH and IH+NLK+LK. The first model used a combined isotropic-nonlinear kinematic hardening and in the second model, a linear term was added to the Armstrong-Frederick model for evolution of backstress in LK. However they concluded that neither the IH+NLK model nor the IH+NLK+LK model could accurately describe all the phenomena observed in cyclic experiments [57].

In parallel to modifying the nonlinear kinematic hardening models, two-surface plasticity models also attracted a lot of attention because both the transient and long-term behaviour of the material could be fairly well described by these models. In two-surface models, the evolution of the inner surface is usually defined such that it describes the transient response of the material and the evolution of the bounding surface is usually responsible for describing the long-term response of the material. Among these models, the two-surface model developed by Yoshida and Uemori (2002) is of more interest in the current study and will be used for the analysis of sidewall curl for the channel draw operation in AHSS materials.

An assessment of recent plasticity models indicates that various methods exist to quantitatively describe the deformation of sheet metals. But as the capabilities

of material model improve, the number of material parameters necessary to describe the deformation also increases, and this inevitably leads to more complex material characterization tests and more sophisticated mathematical techniques to determine these parameters [21]. This may be an undesirable situation from an industrial perspective, since the simple tension test is usually the only available material data during the tooling design phase and is also the industry standard for the identification of sheet metal properties. However once the parameters are identified, more accurate results can be expected from improved material models.

### 2.2.5 Identification of material parameters

As discussed, many purely phenomenological hardening laws have been proposed in the literature with the purpose of describing the cyclic behaviour of metal sheets. The complexity of these models can vary considerably with respect to the number of material parameters and strain history variables. The material parameters involved have to be determined from some kind of cyclic loading experiment.

In theory, the most simple and straightforward test is a tension/compression test of a sheet strip. In practice, however, such a test is very difficult to perform, due to the tendency of the strip to buckle in compression. In spite of these difficulties, some successful attempts to perform cyclic tension/compression tests have been reported in the literature. Bulk compression tests (Abel and Ham, 1966; Bate and Wilson, 1986) and in-plane compression tests (Ramberg and Miller, 1946; Tan et al., 1994; Yoshida et al., 2002) provided more uniform strain distribution with appropriate length-to-thickness ratio. But large strain was not easy to obtain due to the specimen's tendency to buckle under compression. Yoshida et al. [60] successfully bonded a few thin sheets of metal to provide support for the sheet during uniaxial compression.

Kuwabara (1995, [34]) used fork-shaped dies to reduce the unsupported area during uniaxial tension-compression tests. Normal forces were provided by the weight

of the die itself. However there were unavoidable uncovered areas of the sample between each pair of ‘fingers’ of the die which were prone to buckling. Wagoner et al. (2005, [53]) used solid flat plates as buckling constraints and applied normal pressure through a hydraulic clamping system. But the problem remained with gaps between the die and clamps of the tensile machine.

Recently, Cao et al. (2009, [7]) developed a fixture to perform uniaxial tension-compression tests on modified “dog-bone” specimens with single or double sided fins. Experiments were done for DP600 and AA6111-T4 sheet samples and material parameters were determined for a combined isotropic-kinematic hardening law based on the Chaboche model as well as for a modified two surface model based on Dafalias-Popov and Krieg models.

Cyclic simple shear tests have also attracted the attention of some researchers as the specimen is not compressed during these tests. Miyauchi (1984, [30]), Genevois (1992, [42]), Rauch (1998, [44]) and Barlat et al. (2003, [20]) have successfully used the simple shear test for reverse loading at large strains.

Another kind of test that frequently has been used for the determination of material hardening parameters is some kind of bending test [63], [40], [56]. The advantage of this kind of test is that it is simple to perform, and standard test equipments can be used. However, a bending test will involve inhomogeneous stress and strain distributions in the sheet specimen, and the stress-strain response cannot be directly determined from the experiment. This means that the material parameters have to be determined by an inverse approach. Usually, the experiments are simulated by FEA, and the material parameters are identified by means of some optimization technique.

The optimization methods for determining the parameters in a material model are usually based on an inverse approach in which an appropriate algorithm allows the minimization between experimental observable variables and simulated ones. Here, the optimization variables  $\boldsymbol{x}$  are the material parameters and the purpose is

to find a vector  $\mathbf{x}$  that minimizes the objective function:

$$F(\mathbf{x}) = \sum_{i=1}^L s^i F^i(\mathbf{x}), A_j \leq x_j \leq B_j, (j = 1, 2, \dots, N) \quad (2.6)$$

where  $L$  is the total number of deformation cycles,  $A_j$  and  $B_j$  are the lower and upper limits of the searching area for a material parameter  $x_i$ , and  $F^i(\mathbf{x})$  is the dimensionless function defined as the square of the difference in stress between the experimental data, and the corresponding calculated results for an assumed set of material parameters  $\mathbf{x}$ . For the minimization of the objective function different techniques are used by researchers. Yoshida (1998, [56]) used an iterative multi-point approximation concept by minimizing the difference between the test results and the results obtained by numerical simulation of the same test. This approach was verified by comparing simulated stress-strain curves using constitutive model incorporating identified parameters with experimental cyclic bending curves. The same method was later used for identification of Chaboche model parameters for an aluminum clad stainless steel sheet (2003, [61]) and also for determining parameters in the YU model from cyclic tension-compression tests for mild and high strength steels (2002, [57]).

Collin et. al. (2009, [14]) used an inverse approach coded in a software called ‘SidoLo’ which allows the minimization between experiments and simulations with a decrease direction algorithm to determine the Chaboche model parameters from monotonic and cyclic tensile tests. The parameters were then used in a FE code to simulate cyclic indentation experiments.

In a recent study, Eggertsen and Mattiasson (2010, [17]) used an inverse approach for determining different hardening parameters, using simulations of three-point cyclic bending tests by means of the explicit FE-code LS-DYNA [38]. The identification of the hardening parameters was performed by means of the optimization code LS-OPT [47] and a Response Surface Methodology (RSM). The RSM is especially advantageous for problems in which gradients to the objective func-



tion are difficult to calculate, such as in highly nonlinear problems of parameter identification.

Although using optimization tools like LS-OPT or SiDoLo facilitates the determination of material parameters, it should be pointed out that different experiments as well as the same experiment performed with varying conditions can result in different parameter sets which may affect the predictability of the material model specially for springback/sidewall curl in AHSS [31].

The methods for identification of the YU model parameters from cyclic tension-compression experiments are discussed after a brief explanation of the model itself. Later, several other material models that are implemented in commercial finite element codes are described and compared with YU model.

### **2.3 Yoshida-Uemori two-surface plasticity model**

As mentioned before, advanced models of material equations are required for more accurate simulation of sheet metal forming and subsequent springback. Cyclic loading is a very common type of loading in sheet metal forming processes as the material flows over the punch radius, die radius or through a drawbead. The Yoshida-Uemori (YU) model [57] is one of the most sophisticated and comprehensive phenomenological models and is capable of reproducing the transient Bauschinger effect, permanent softening and work-hardening stagnation in large elasto-plastic deformations, as shown in Fig.2.11.

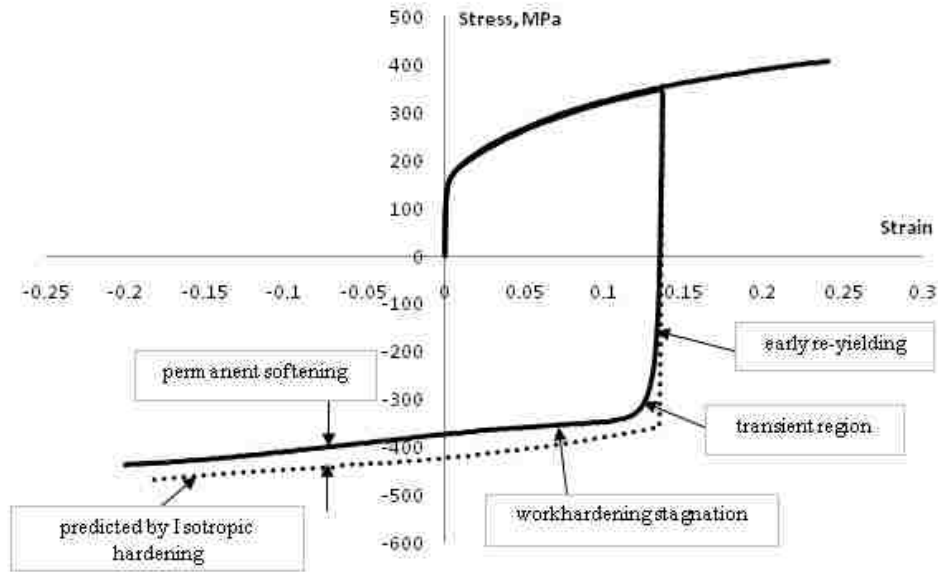


Figure 2.11: Stress-strain response of a mild steel in a forward and reverse loading and the cyclic phenomena, [58]

The YU model assumes kinematic hardening of the yield surface within the bounding surface and mixed isotropic-kinematic hardening of the bounding surface itself. The evolution of the yield surface is defined by superposition of two kinematic hardening laws and therefore it is possible to assume that a total of three surfaces are defined in the plane stress space. The additional surface controls the permanent softening and the work hardening stagnation.

The inner surface, or yield surface, determines the elastic domain of the material in stress space. It is assumed that this surface can only translate in stress space, i.e. it undergoes a pure kinematic hardening. This is a valid assumption since experimental stress-strain responses under reverse deformation show that the re-yielding starts at a very early stage of stress reversal. Therefore, kinematic hardening of the yield surface describes the transient Bauschinger deformation characterized by early re-yielding and subsequent rapid change of work-hardening rate, which is mainly due to the motion of less stable dislocations, such as piled-up dislocations. The bounding surface, on the other hand, can translate as well as expand, i.e. mixed hardening prevails (Fig.2.12).

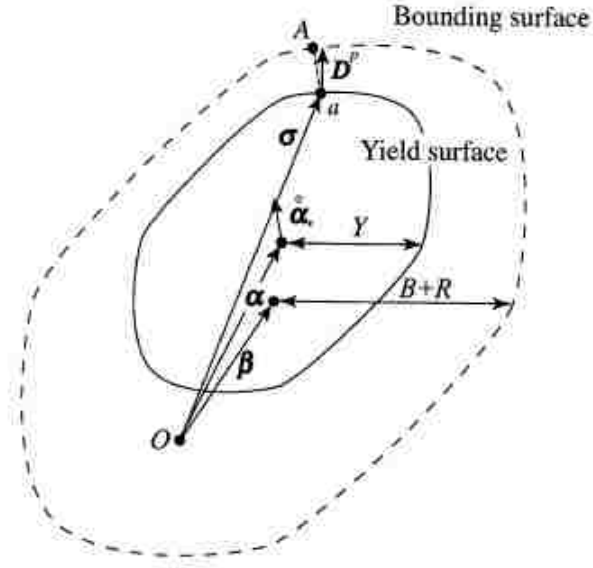


Figure 2.12: Schematic illustration of the two-surface model, [58]

The size of the yield surface is thus constant, and we have  $\sigma_{iso} = Y$ , where  $Y$  is the initial, uniaxial yield stress. The yield function can, thus, be written as:

$$f = \bar{\sigma}(\boldsymbol{\sigma} - \boldsymbol{\alpha}) - Y = 0 \quad (2.7)$$

The bounding surface is described by the following equation:

$$F = \bar{\sigma}(\boldsymbol{\sigma} - \boldsymbol{\beta}) - (B + R) = 0 \quad (2.8)$$

where  $\boldsymbol{\beta}$  locates the centre of the bounding surface,  $B$  is its initial size, and  $R$  represents its isotropic hardening. The relative motion of the yield surface with respect to the bounding surface is expressed by:

$$\boldsymbol{\alpha}^* = \boldsymbol{\alpha} - \boldsymbol{\beta} \quad (2.9)$$

The relative kinematic motion  $\boldsymbol{\alpha}^*$  is a function of the difference between the sizes of the two surfaces and is defined such that the inner surface never passes

the outer surface. Therefore, the yield surface never passes through the bounding surface. This fact makes the numerical implementation of the YU model much easier compared to other two-surface models.

The evolutions of  $\boldsymbol{\alpha}^*$  and  $\boldsymbol{\beta}$  are given by the equations:

$$\dot{\boldsymbol{\alpha}}^* = C \left[ \frac{B + R(\bar{\varepsilon}^p) - Y}{Y} (\boldsymbol{\sigma} - \boldsymbol{\alpha}) - \boldsymbol{\alpha}^* \right] \dot{\bar{\varepsilon}}^p \quad (2.10a)$$

$$\dot{\boldsymbol{\beta}} = k \left[ \frac{b}{B + R(\bar{\varepsilon}^p)} (\boldsymbol{\sigma} - \boldsymbol{\beta}) - \boldsymbol{\beta} \right] \dot{\bar{\varepsilon}}^p \quad (2.10b)$$

where  $\dot{\bar{\varepsilon}}^p$  is the effective plastic strain rate, and  $C$  is a material constant that controls the rate of the kinematic hardening. Eq.2.10a indicates that the yield surface moves in such a way that the current stress point existing on the yield surface is approaching the corresponding point on the bounding surface. Under a uniaxial stress state, this equation is simplified to:

$$\dot{\alpha}^* = c(B + R - Y) \left[ \dot{\varepsilon}^p - \text{sgn}(\alpha^*) \sqrt{\frac{\bar{\alpha}^*}{B + R - Y}} |\dot{\varepsilon}^p| \right] \quad (2.11)$$

To describe the global work-hardening, which is associated with the formation of stable dislocation structures, for the bounding surface, the evolution of  $R$  is assumed to be:

$$\dot{R}(\bar{\varepsilon}^p) = k(R_{sat} - R(\bar{\varepsilon}^p)) \dot{\bar{\varepsilon}}^p \quad (2.12)$$

where  $R_{sat}$  is the saturated value of the isotropic hardening stress  $R$  at infinitely large plastic strain, and  $k$  is a material parameter that controls the rate of isotropic hardening. The meaning of various parameters in the above equations is explained graphically in Fig.2.13. It should be noted that in uniaxial tension, the bounding surface is explicitly expressed by Eq.2.13.

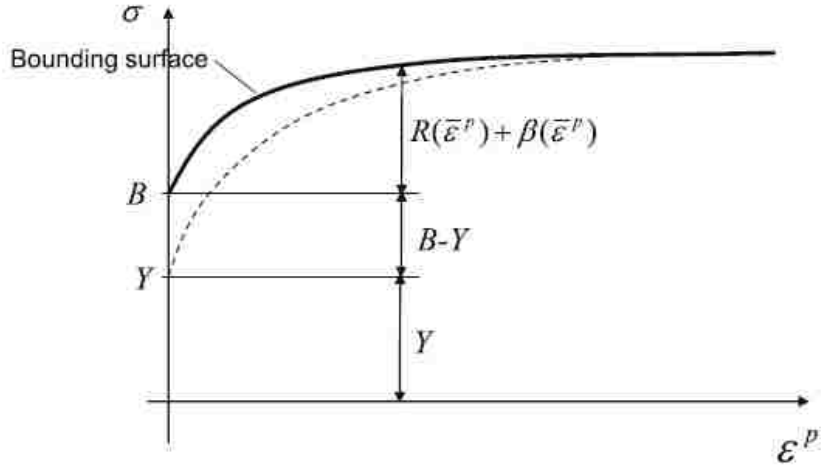


Figure 2.13: Definition of the parameters in the Yoshida-Uemori hardening model - Forward Bounding, [18]

$$\sigma_{bound}^{forward} = B + R + \beta = B + (R_{sat} + b) \left(1 - e^{-k\varepsilon^p}\right) \quad (2.13)$$

It should be emphasized that the mentioned formulas are the original form of the Yoshida-Uemori model. Further modifications were later made to this model in order to be able to reproduce more exactly the experimental hardening curves from a uniaxial tensile test, in which:

$$B = Y \quad (2.14)$$

$$Y + R(\bar{\varepsilon}^p) + \beta(\bar{\varepsilon}^p) = H(\bar{\varepsilon}^p) \quad (2.15)$$

where  $H(\bar{\varepsilon}^p)$  is the experimental plastic hardening curve [18].

The experimentally obtained stress-strain curves on a mild steel exhibit apparent work-hardening stagnation in a certain period of reverse deformation starting from the reverse re-yielding. This phenomenon is also related to the cyclic strain-range, as well as the mean-strain. It is mainly caused by the dissolution of dislocation cell walls performed during forward deformation and the formation of new dislocation

microstructures during reverse deformation [28], [11]. To model work-hardening stagnation as well as permanent softening during reverse deformations, Yoshida and Uemori introduced an additional surface  $g_\sigma$  (shown in Fig.2.14), in the stress space defined by:

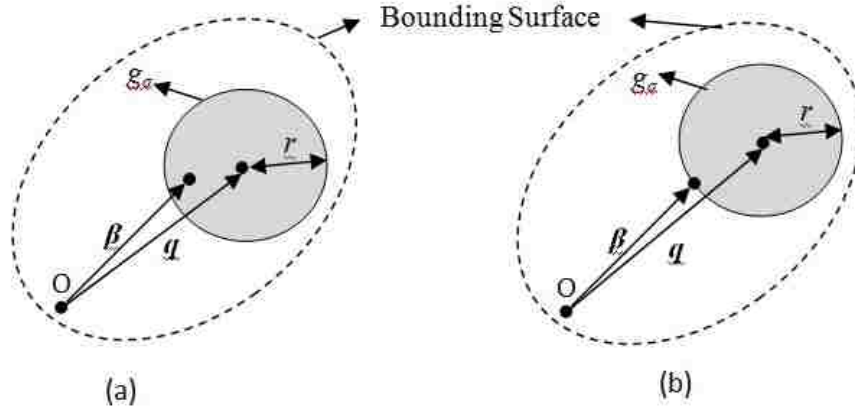


Figure 2.14: Schematic illustration of stagnation surface: a) non-isotropic hardening ( $\dot{R} = 0$ ); b) isotropic hardening takes place ( $\dot{R} > 0$ ), [59]

$$g_\sigma = \bar{\sigma}(\beta - q) - r = 0, \quad (2.16)$$

where  $r$  denotes the size of  $g_\sigma$  and  $q$  its centre. The center of the bounding surface, defined by  $\beta$ , is forced to always be situated inside, or on the boundary of  $g_\sigma$ . The purpose of this additional surface is to govern the evolution of the parameter  $R$ , such that  $R$  only evolves when  $\beta$  is situated on the boundary of  $g_\sigma$ . Therefore, isotropic hardening of the bounding surface takes place if the centre of the bounding surface is located on the boundary of  $g_\sigma$ . The evolution of  $r$  was assumed to be:

$$\dot{r} = h \frac{3(\beta - q)^T P \dot{\beta}}{2r}, \text{ when } \dot{R} > 0 \quad (2.17a)$$

$$\dot{r} = 0, \text{ when } \dot{R} = 0 \quad (2.17b)$$

where ( $0 \leq h \leq 1$ ) is a material parameter that determines the rate of expansion of surface  $g_\sigma$ , and  $P$  is:

$$P = \frac{1}{3} \begin{bmatrix} 2 & -1 & -1 & 0 & 0 & 0 \\ & 2 & -1 & 0 & 0 & 0 \\ & & 2 & 0 & 0 & 0 \\ & & & 3 & 0 & 0 \\ & Sym & & & 3 & 0 \\ & & & & & 3 \end{bmatrix}$$

Larger values of  $h$  lead to a rapid expansion of the non-IH surface, and as a result, less cyclic hardening takes place. Since the non-IH (work-hardening stagnation) appears during reverse deformation after prestrain, the initial value of  $r$  may be assumed to be very small.

### 2.3.1 Degradation of elastic stiffness during unloading

The amount of springback during unloading depends to a great extent on the elastic stiffness of the material. In classic elastic-plastic theory, the unloading of a material after plastic deformation is assumed to be linearly elastic with the stiffness equal to Young's modulus. However, several experimental investigations have revealed that this is an incorrect assumption. Levy et al. (2006, [36]) reported that the apparent unloading modulus is smaller than the initial elastic modulus and experimentally obtained the variation of unloading modulus as a function of plastic strain for AKDQ and DP600 sheet materials. Eggertsen and Mattiasson (2010, [19]) studied and discussed this phenomenon extensively. Their study confirmed earlier investigations from the literature that the unloading path is not linear and nor is the reloading path. Both the unloading and the reloading paths are slightly curved, and deviate from linearity around an imaginary "mean" line, representing the secant to the curves (Fig.2.16). Moreover, the slope of this secant is strongly affected by

the amount of plastic strain. This is mainly due to very early re-yielding and the Bauschinger effect and strongly affected by the amount of plastic strain. More precisely, the magnitude of the unloading modulus is decreasing with increasing plastic strain.

Such a prestrain dependency of Young's modulus would much influence the springback behaviour especially when sheets are subjected to a large deformation during press forming. However, for practical modeling, instead of instantaneous Young's modulus, Yoshida introduced a term called 'average Young's modulus',  $E_{av}$ , as an average slope of the unloading stress-strain curve calculated from each of following stress ranges (Fig.2.15) :

1.  $0.75\sigma_0 \leq \sigma \leq 0.95\sigma_0$ ,
2.  $0.50\sigma_0 \leq \sigma \leq 0.95\sigma_0$ ,
3.  $0.25\sigma_0 \leq \sigma \leq 0.95\sigma_0$ ,
4.  $0 \leq \sigma \leq 0.95\sigma_0$ .

Since the stress-strain response just after the beginning of unloading was highly nonlinear, which would be due to the viscosity of the steels,  $0.95\sigma_0$  was chosen as the starting point for determination of the average Young's modulus, rather than the stress reversal point,  $\sigma_0$ .

The variation of the unloading modulus with plastic strain was expressed with an analytical function by Yoshida et al. [58] :

$$E_u = E_0 - (E_0 - E_{sat}) \cdot \left(1 - e^{-\xi \cdot \bar{\epsilon}^p}\right) \quad (2.18)$$

where  $E_0$  is the initial Young modulus,  $E_{sat}$  is a value that the unloading modulus saturates towards, and  $\xi$  is a material parameter. The notation  $E_u$  represents the slope of the secant to the non-linear unloading path and the variable  $E_t$  in Fig.2.16 is the slope just at the beginning of the unloading or reloading path. Instead of  $E_u$ , it would be more practical to use  $E_{av}$  as explained before. The parameters  $E_{sat}$



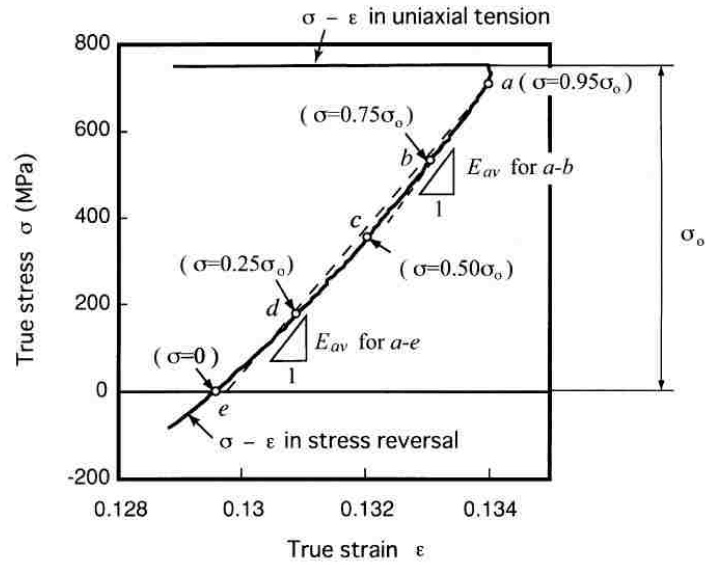


Figure 2.15: An example of unloading stress-strain response for the high strength steel sheet. The average Young's modulus  $E_{av}$  is defined as an average slope of the unloading stress-strain curve in a certain stress range, as shown by broken lines, [60]

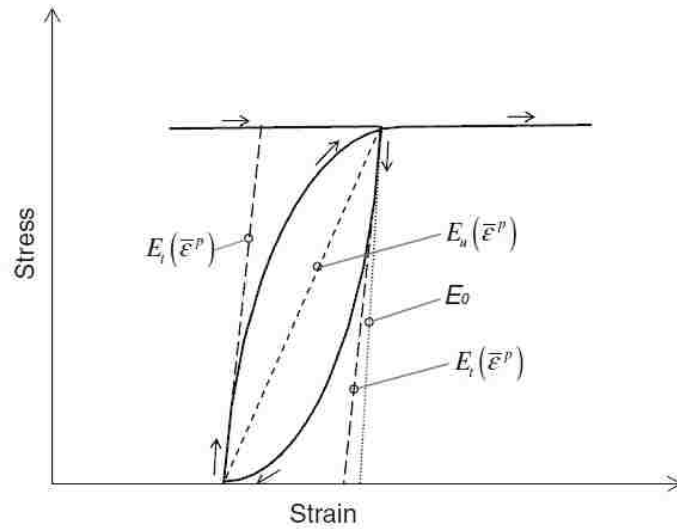


Figure 2.16: A schematic illustration of the stress-strain relationship of an unloading/reloading cycle, [19]

and  $\xi$  are determined from experimental uniaxial tension data at various pre-strain levels until the saturated values can be observed at sufficiently large prestrain levels.

2.3.2 Identify the YU Hardening parameters from cyclic tests

The original YU hardening model contains seven material parameters ( $Y$ ,  $C$ ,  $B$ ,  $R_{sat}$ ,  $b$ ,  $k$ ,  $h$ ). In order to obtain these unknown parameters from experimental cyclic tests, tension-compression in particular, one of two methods can be used: the systematic method and the optimization method. In the systematic method, the cyclic stress-strain curve is used to calculate the parameters as follows (Fig.2.17):

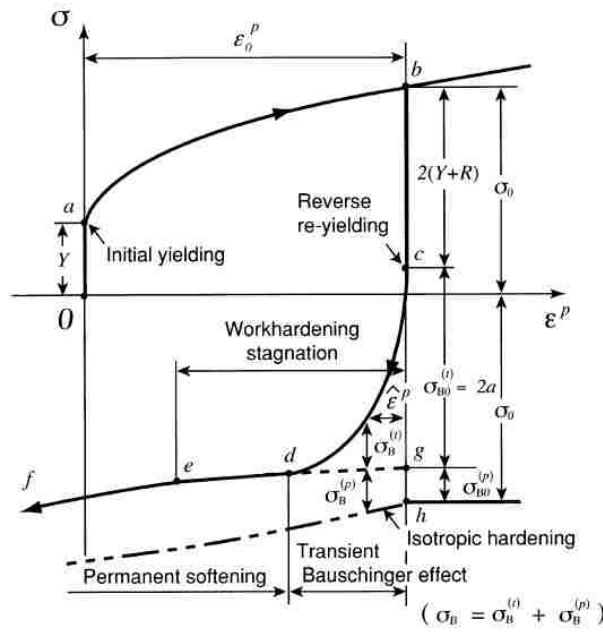


Figure 2.17: Schematic illustration of stress-strain response during forward and reverse deformation, [60]

- The radius of the yield surface  $Y$  is determined as the elastic limit.
- From a forward-reverse stress-strain curve, the lines of forward and reverse bounds can be drawn as schematically illustrated in Fig.2.18.b (lines (b)-(c) for forward deformation and (j)-(f)-(g) for reverse deformation). The forward bounding stress curve is used in the first cycle to fit the experimental curve to Eq.2.13. Therefore, parameters  $B$ ,  $(R_{sat} + b)$  and  $k$  will be found.

It should be mentioned that the stress offset  $\sigma_B$ , defined as the difference in the flow stress between forward and reverse deformations, is a measure of the

Bauschinger effect.  $\sigma_B$  can be divided into two parts, namely the ‘transient softening’,  $\sigma_B^{(t)}$  and the ‘permanent softening’,  $\sigma_B^{(p)}$  which appears after the transient period. In the reverse deformation, the transient softening is the difference between the reverse stress-strain curve and the extrapolated curve of the region of permanent softening.

- In order to find  $b$ , it is required to find  $\sigma_{B0}^{(p)}$  which is equal to the difference between the experimental yield stress and predicted yield stress by isotropic hardening model at the beginning of reverse loading (at  $\hat{\epsilon}_p = 0$ , as shown in Fig.2.18a). From Eq.2.10b, the amount of softening at the beginning of reverse loading is given by:

$$\sigma_{B0}^{(p)} = 2\beta_0 = 2b \left( 1 - e^{-k\epsilon_0^p} \right), \quad (2.19)$$

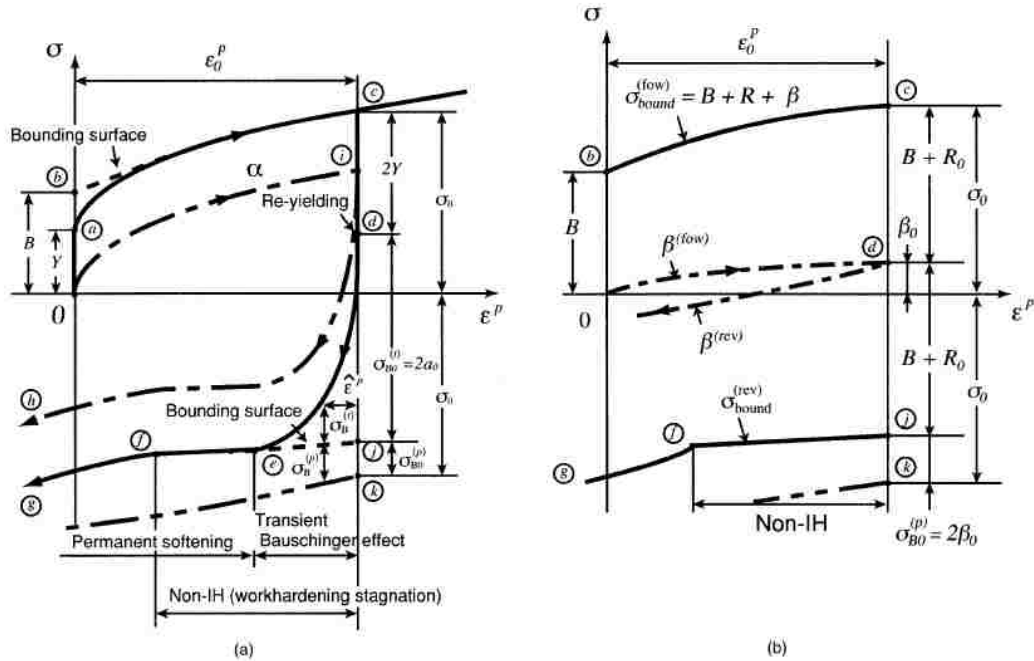


Figure 2.18: Schematic illustrations of the motion of: (a) the yield surface; and (b) the bounding surface under a uniaxial forward-reverse deformation [57]

where  $\beta_0$  denotes the kinematic hardening of the bounding surface at the stress reversal point, and  $\varepsilon_0^p$  is the plastic prestrain at the beginning of reverse loading. From Eq.2.19, the parameter  $b$  is obtained. Since  $(R_{sat} + b)$  is already known from the previous step,  $R_{sat}$  is also determined.

Referring to the definition of  $\sigma_B^{(t)}$  and  $\sigma_B^{(p)}$ , the determination of the dividing point 'e', Fig.2.18a includes a certain ambiguity, however it should not affect the relationship between the transient and permanent softening vs.  $\hat{\varepsilon}^p$ , as the rate of work-hardening at this point is so small with respect to the transient softening. The initial value of transient softening when reverse re-yielding just starts (at  $\hat{\varepsilon}^p = 0$  which is indicated as  $\sigma_{B0}^{(t)} = 2a$  in Fig.2.18a, increases with the plastic prestrain.

Alternatively, it is possible to find parameter  $b$  from the reverse bounding surface in the region of work-hardening stagnation:

$$\sigma_{bound}^{(rev)} = -(B + R_0) + \beta^{(rev)}, \quad (2.20a)$$

$$R_0 = R_{sat} \left(1 - e^{-k\varepsilon_0^p}\right), \quad (2.20b)$$

$$\beta^{(rev)} = b \left[-1 + 2e^{-k\hat{\varepsilon}^p} - e^{-k(\varepsilon_0^p + \hat{\varepsilon}^p)}\right]. \quad (2.20c)$$

- Parameter  $C$  is identified from the stress-strain curve of the transient Bauschinger deformation. From Eq.2.10a, for reverse deformation after large forward pre-strain:

$$C \approx \frac{2}{\hat{\varepsilon}^p} \left[ (1 + \ln 2) - \sqrt{\frac{|\alpha_*|}{a}} + \ln(1 + \text{sgn}(\alpha_*) \sqrt{\frac{|\alpha_*|}{a}}) \right] \quad (2.21)$$

Since  $\sigma_B^{(t)} = a + \alpha_*$ ,  $\frac{\alpha_*}{a}$  is given as a function of the transient stress offset  $\sigma_B^{(t)}$  as:

$$\frac{\alpha_*}{a} \approx \frac{\sigma_B^{(t)}}{a_0} - 1 = 2 \left( \frac{\sigma_B^{(t)}}{\sigma_{B0}^{(t)}} \right) - 1, a_0 = \frac{1}{2} \sigma_{B0}^{(t)} = \sigma_0 - Y - \frac{1}{2} \sigma_{B0}^{(p)} \quad (2.22)$$

It is then possible to plot  $\hat{\varepsilon}_p$  vs.  $\frac{\sigma_B^{(t)}}{\sigma_{B0}^{(t)}}$  for various values of  $C$  and compare them with experimental data to find the best value for  $C$ .

- Parameter  $h$  should be identified either from the experimental magnitude of the plastic strain in which work-hardening stagnation takes place and cyclic hardening characteristics, or from numerical simulation so as to obtain the best-fit curves to the corresponding experimental data.

Instead of the above scheme which has certain amount of ambiguity, it is possible to identify the YU set of parameters simultaneously by using an optimization method introduced in the previous section (Eq.2.6). More details for implementing this methodology will be explained in the next chapters.

## 2.4 LS-DYNA material models for sheet metal forming

The numerical simulations in this investigation were performed with the commercial software LS-DYNA for explicit simulations of forming and implicit simulations of springback. LS-DYNA accepts a wide range of material models and equations of state, each with its unique number of stress-strain history variables. Approximately 150 material models are implemented, and space has been allotted for up to 10 user-specified models [38]. From these models, more attention is placed on several material types that are conventionally used in DYNAFORM, a pre/post processor with LS-DYNA solver engine, which is extensively used for simulation of industrial sheet metal forming processes. An analogy will be presented between these models and the constitutive models explained in the beginning of this chapter.

- **Mat 18: Power Law Isotropic Plasticity** This model provides elastoplastic behaviour with isotropic hardening. The yield stress,  $\sigma_y$ , is a function

of plastic strain and obeys the equation:

$$\sigma_y = K\varepsilon^n = K(\varepsilon_{yp} + \bar{\varepsilon}^p)^n$$

where  $\varepsilon_{yp}$  is the elastic strain to yield and  $\bar{\varepsilon}^p$  is the effective plastic logarithmic strain.

- **Mat 24: Piecewise Linear Plasticity** defines elasto-plastic material with a user-defined stress vs. strain curve and strain rate dependency. It can also model failure.
- **Mat 36: 3\_Parameter Barlat** was developed by Barlat and Lian [1989] for modeling the forming of anisotropic sheet materials under plane stress conditions. This model allows the use of the Lankford parameters to define the material anisotropy. The yield condition can be written as:

$$f(\boldsymbol{\sigma}, \varepsilon_p) = \sigma_{eff}(\sigma_{11}, \sigma_{22}, \sigma_{12}) - \sigma_Y(\varepsilon_p) \leq 0$$

where

$$\sigma_{eff}(\sigma_{11}, \sigma_{22}, \sigma_{12}) = \left( \frac{a}{2} |K_1 + K_2|^m + \frac{a}{2} |K_1 - K_2|^m + \frac{c}{2} |2K_2|^m \right)^{1/m} \quad (2.23a)$$

$$K_1 = \frac{\sigma_{11} + h\sigma_{22}}{2} \quad (2.23b)$$

$$K_2 = \sqrt{\frac{\sigma_{11} - h\sigma_{22}}{2}^2 + p^2\sigma_{12}^2} \quad (2.23c)$$

and the hardening of the yield surface is either linear, exponential or determined by a load curve. In the above, the stress components  $\sigma_{11}$ ,  $\sigma_{22}$  and  $\sigma_{12}$  are with respect to the material coordinate system and  $\varepsilon_p$  denotes the effective plastic strain. The material parameters  $a$ ,  $c$ ,  $h$  and  $p$  can be determined from

the Lankford parameters  $R_0$ ,  $R_{45}$  and  $R_{90}$  (the ratios of instantaneous width to thickness change for each of the directions  $0^\circ$ ,  $45^\circ$  and  $90^\circ$  with respect to the sheet rolling direction  $R = \frac{dW/d\varepsilon}{dT/d\varepsilon}$  with W and T as functions of width and thickness strain):

$$a = 2 \left( 1 - \sqrt{\frac{R_0}{1+R_0} \frac{R_{90}}{1+R_{90}}} \right) \quad (2.24a)$$

$$c = 2 - a \quad (2.24b)$$

$$h = \sqrt{\frac{R_0}{1+R_0} \frac{1+R_{90}}{R_{90}}} \quad (2.24c)$$

The anisotropy parameter  $p$  can be calculated implicitly by an iterative search for the root of the following function:

$$g(p) = \frac{2m\sigma_Y^m}{\left( \frac{\partial f(\sigma)}{\partial \sigma_x} + \frac{\partial f(\sigma)}{\partial \sigma_y} \right) \sigma_{45}} - 1 - R_{45}$$

For FCC materials  $m=8$  is recommended and for BCC materials  $m=6$  may be used.

- **Mat 37: Transversely Anisotropic Elastic Plastic** is a fully iterative plasticity model for simulation of anisotropic sheet metal forming only with shell elements. Hill 1948 yield function with isotropic hardening and transverse anisotropy can be considered as well as optional definition of stress vs. plastic strain curve. The decrease in Young's modulus w.r.t. effective plastic strain can be accommodated with a curve of scale factors or by defining the parameters in the empirical function proposed by Yoshida, Eq. `refeq:unloadingelasticmodulus`. Considering Cartesian reference axes parallel to the planes of anisotropic symmetry, the Hill [1948] yield function of can be

written as:

$$F(\sigma_{22} - \sigma_{33})^2 + G(\sigma_{33} - \sigma_{11})^2 + H(\sigma_{11} - \sigma_{22})^2 + 2L\sigma_{23}^2 + 2M\sigma_{31}^2 + 2N\sigma_{12}^2 - 1 = 0, \quad (2.25)$$

where  $\sigma_{11}$ ,  $\sigma_{22}$  and  $\sigma_{33}$  are the tensile normal stresses and  $\sigma_{12}$ ,  $\sigma_{23}$  and  $\sigma_{31}$  are the shear stresses. The anisotropy constants F, G, H, L, M and N are related to the yield stress as in Eq.2.26.

$$\begin{aligned} F &= \frac{(\sigma^0)^2}{2} \left( \frac{1}{\sigma_{22}^2} + \frac{1}{\sigma_{33}^2} - \frac{1}{\sigma_{11}^2} \right), \\ G &= \frac{(\sigma^0)^2}{2} \left( \frac{1}{\sigma_{33}^2} + \frac{1}{\sigma_{11}^2} - \frac{1}{\sigma_{22}^2} \right), \\ H &= \frac{(\sigma^0)^2}{2} \left( \frac{1}{\sigma_{11}^2} + \frac{1}{\sigma_{22}^2} - \frac{1}{\sigma_{33}^2} \right), \\ L &= \frac{3}{2} \left( \frac{\tau^0}{\sigma_{23}} \right)^2, \\ M &= \frac{3}{2} \left( \frac{\tau^0}{\sigma_{13}} \right)^2, \\ N &= \frac{3}{2} \left( \frac{\tau^0}{\sigma_{12}} \right)^2. \end{aligned} \quad (2.26)$$

where each  $\sigma_{ij}$  is the measured yield stress value when  $\sigma_{ij}$  is applied as the only nonzero stress component;  $\sigma^0$  is the user-defined reference yield stress specified for the metal plasticity definition; and  $\tau^0 = \frac{\sigma^0}{\sqrt{3}}$ .

For the special case of plane stress, where  $\sigma_{33} = 0$ , the anisotropy input parameter  $R$  is defined as the ratio of the in-plane plastic strain rate to the out-of-plane plastic strain rate:

$$R = \frac{\dot{\varepsilon}_{22}}{\dot{\varepsilon}_{33}}$$

Using the plane stress assumption and the definition of  $R$ , the yield function can be written as:



$$f(\sigma) = \sqrt{\sigma_{11}^2 + \sigma_{22}^2 - \frac{2R}{1+R}\sigma_{11}\sigma_{22} + 2\frac{2R+1}{1+R}\sigma_{12}^2}, \quad (2.27)$$

- **Mat 125: Kinematic Hardening Transversely Anisotropic** combines Yoshida non-linear kinematic hardening rule with Mat37. This theory needs two surfaces to describe the hardening behaviour: the yield surface and the bounding surface. In the forming process, the yield surface does not change in size but its center translates with deformation; the bounding surface changes both in size and location. This model also allows for a change of Young's modulus as explained in Mat 37.

It should be mentioned here that Mat 125 was implemented in LS-DYNA based on the general publications of YU model. However it has been observed that springback results using this model are not consistent with predictions using other software. Therefore, it appears that the YU model was incorrectly implemented in the current version of LS-DYNA (version 971, edition R5.1.1)

Material models 24, 36, 37 and 125 will be used for the numerical analysis of the channel draw process in order to identify how accurately they can predict the springback and sidewall curl of the channel sections made of AHSS materials. Further details of implementation and modeling will be explained in subsequent chapters.

# Experimental study

---

## 3.1 Introduction

A channel forming process - previously presented as Benchmark #3 in Numisheet 2005 conference - was used in the current research in order to assess the capability of various material models to predict sidewall curl, as well as the effect of several geometrical parameters such as die entry radius and drawbead penetration for high strength steels. Two grades of steel, DP980 and TRIP780, were used to draw channel sections in the presence of drawbeads and with various die entry radii in a draw die specially designed for this type of research. The experimental work to produce these channels is described hereafter. This will provide the necessary information for numerical simulating the channel drawing process.

As DP980 and TRIP780 materials have variable properties with respect to the rolling direction, a series of characterization tests were also performed to identify their respective mechanical properties. Furthermore, the procedure for identifying specific material parameters for the constitutive models introduced in the second chapter, will be explained in this chapter. Results of various characterization tests for each of the study materials will also be presented.

## 3.2 Description of the channel draw process

Numisheet channel draw benchmark was provided by General Motors Corporation, Research & Development Institute IRDI and the US National Institute of

Standards and Technology (NIST) along with the US Steel Corporation for the Numisheet 2005 conference in Detroit, MI. The draw die was made by the Auto/Steel Partnership (A/SP) to form straight channel sections. The draw die was installed at a local stamping plant (NARMCO) in a Williams/White hydraulic 600-ton press with a stroke of 1310 mm, for the analysis of different grades of advanced high strength steel sheets and in order to understand the effects of different forming parameters on the springback and sidewall curl of the channels (Fig. 3.1 ). The draw die was constructed in such a way that the material in the channel sidewalls was formed over a drawbead and a die entry radius, thus work hardening the sheet by cyclic bending and unbending in the drawbead and over the die radius. Blanks were sheared to a width of 254 mm so that the channel sidewalls would be stretched in plane strain.



Figure 3.1: A/SP die installed in a hydraulic press

A schematic of the draw die in its open position is shown in Fig. 3.2 . This tool consists of an upper moving die section, a floating binder mounted on six cylinders pressurized by Nitrogen and a fixed lower punch. The upper die is equipped with changeable inserts on each side that provide different die entry radii as well as different inboard and outboard penetrations for the drawbeads. In this project no outboard drawbeads were used and flat blocks were inserted in their locations. Lower female drawbead inserts were mounted on the binder such that they would mate with the upper B and C male drawbead inserts. The female inserts could provide space for single or double beads to deform the sheet metal as well (Fig.3.3).

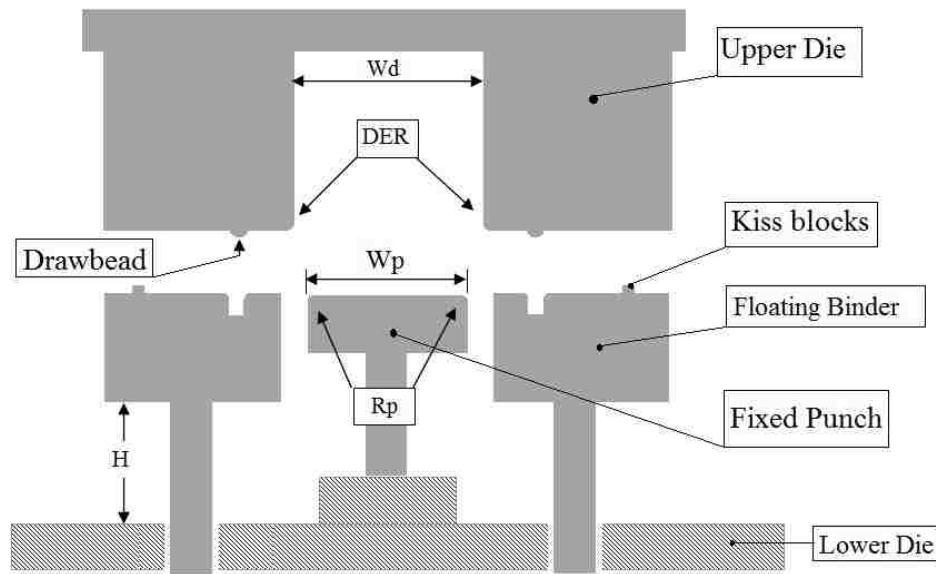


Figure 3.2: sideview of the A/SP die components and general dimension parameters

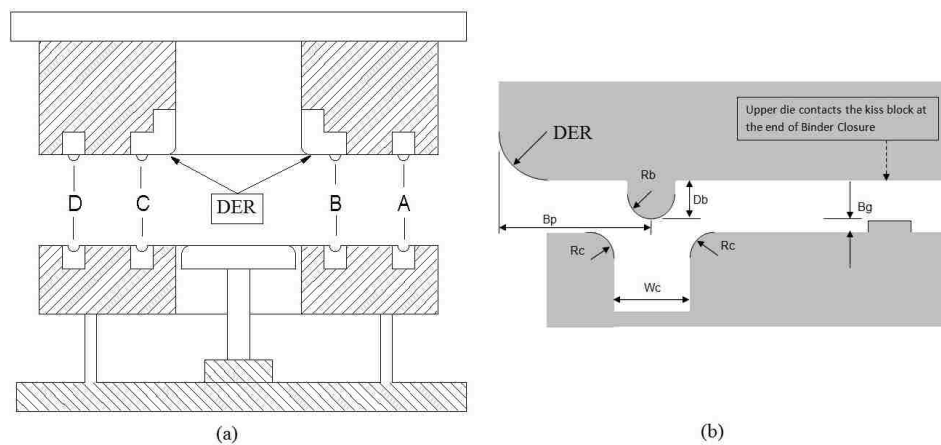


Figure 3.3: (a) schematic view of the die with changeable inserts with various die entry radius and inboard drawbeads (B, C) and outboard beads (A, D); (b) dimensional parameters of die drawbead block and kiss block on the binder shown in open position

Motion of the upper die and binder was restricted by four rigid blocks positioned under the binder for about 20 mm of the whole stroke. Also for safety considerations and ensuring repeatable total stroke, blocks with a total height of 1074 mm were set on two sides of the tool to restrict the movement of the press ram during the stroke. There were also four shimmable kiss blocks located on the top surface of the binder

which were used to maintain a constant gap between the binder and the upper die. This kiss gap was adjusted for each material thickness to maintain a clearance of approximately 30% more than the stock thickness. The symmetry of the tool was checked by multiple measurements of the drawbead height, kiss blocks heights with respect to the binder surface and dimensions with respect to the center of symmetry as shown in Fig.3.4.

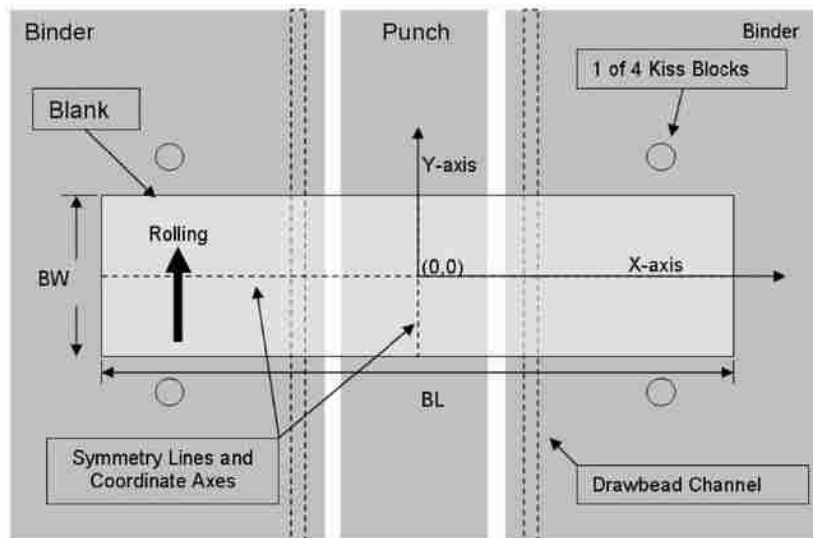


Figure 3.4: Illustration of symmetry in the channel draw process

From the set of available drawbeads, round beads with a 4mm radius were selected for the single bead trials. These drawbeads and the die entry blocks were polished with very fine sandpaper (180 - 320 grit). They were then heat-treated to a hardness of 50 HRC. Shims were added to their back plates to increase the drawbead penetration and to produce channels with a variety of adjustable parameters. A brief description of these parameters is provided here before identifying the selected cases for each material type:

- **Clearance:** The binder clearance is the distance measured vertically between the binder surface and the upper die surface when the upper die is in contact with the kiss blocks.

This vertical clearance between the binder and the upper die was equivalent to the sheet thickness plus the kiss gap. This parameter could be measured with solder imprints by closing the die without a sheet metal blank. The same clearance was applied to all sides.

- **Kiss gap:** Vertical distance (air gap) between the binder and the upper die NOT including the thickness of the sheet material. “Kiss” blocks that were located on each corner of the floating binder maintained the kiss gap.

$$\text{Kiss gap} = \text{Clearance} - \text{Material Thickness}$$

- **Male bead height:** The height of a male bead is the vertical distance that the bead protrudes from the surface of the upper insert that is flush with the upper die face. The penetration of the drawbead is then calculated from the measured male bead height as:

$$(\text{average}) \text{ Penetration} = (\text{average}) \text{ Height} - \text{Kiss gap}$$

- **Penetration:** The penetration of a drawbead was defined according to the following:
  - *0% penetration:* when the male bead is in contact with the sheet material but the sheet is not subject to any bending (Fig.3.5).

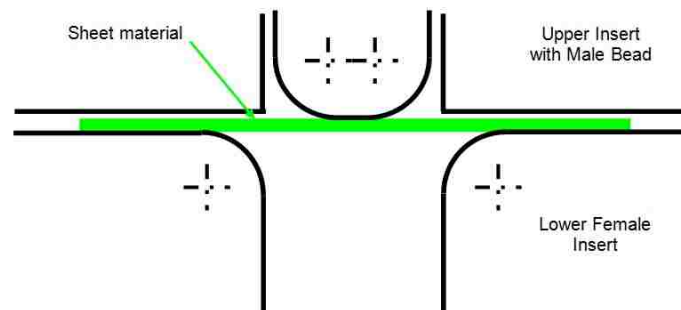


Figure 3.5: Drawbead at 0% penetration

- *100% penetration*: when the centres of curvature for the radii of both male and female beads lie on the same horizontal line (Fig.3.6).

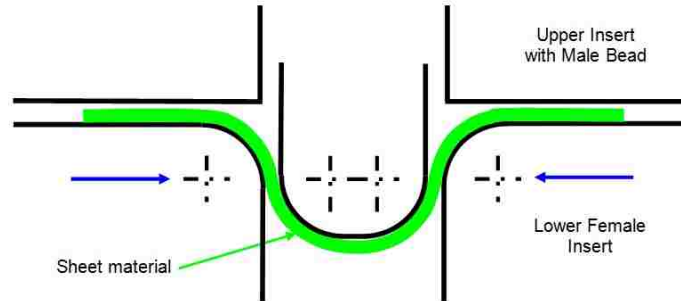


Figure 3.6: Drawbead at 100% penetration

$$\text{Penetration}\% = \frac{\text{Ave. Penetration} * 100}{\text{Upper Bead Radius} + \text{Female Insert Radius} + \text{Material Thk}}$$

Based on these definitions, a set of geometrical and process parameters for the study materials were selected and tested during a set of pre-trial experiments. The general dimensional parameters of the tools and blanks were as summarized in Table 3.1 and selected drawbead configurations are presented in Table 3.2.

The pre-trial tests showed that with the high strength materials, deeper drawbeads would require much more force input from the press and also resulted in scoring of the channel sidewalls. Therefore only the specific cases which are described in Table 3.2 were selected for the actual experiments. Another set of tests were also performed for each material type using inserts with a die entry radius of 12, 6 and 3 mm but without any male drawbeads. Other parameters of the latter experiments were similar to the conditions with beads.



Table 3.1: Geometrical dimensions for channel draw process

Component	Description	Symbol	value(mm)
Upper Die	Width of Die Cavity	$W_d$	257.8
	Die Entry Radius	DER	12.0
Punch	Width of Punch	$W_p$	224.0
	Radius of Punch Profile	$R_p$	12.0
Binder	Width of Binder		1074.0
	Kiss block gap	$B_g$	See Table 3.2
Drawbead	Bead position w.r.t. cavity center line	$B_p$	31.05
	Male bead height	$D_b$	See Table 3.2
	Radius of bead	$R_b$	4.0
	Width of female bead	$W_c$	10.8
	Radius of female bead	$R_c$	4.0
Blank	Width	$B_W$	254
	Length	$B_L$	996 (DP980) 965 (TRIP780)

Table 3.2: Adjustable parameters of drawbeads and kiss blocks for each configuration

Material	Thickness (mm)	Clearance (mm)	Adjusted kiss gap (mm)	Actual bead penetration%	$D_b$ (mm)	Symbol
DP980	1.5	1.85	0.36	20	2.2	DPSB
				25	2.7	DPMB
				37	4.0	DPDB
				100	9.5	-
TRIP780	1.2	1.5	0.30	20	2.2	TPSB
				25	2.7	TPMB
				40	4.0	TPDB
				100	9.2	-

After setting up each configuration, sample tryouts were carried out using ordinary draw quality steel sheet before the actual tests were done. A total of 5 channel sections were produced for each case of the experiments, while recording the punch force, binder displacement and cylinder pressures using a data acquisition system. A brief explanation of the data acquisition hardware and setup of the measurement sensors is given in next section. Before the actual experiments for each material type, the blanks cut to the required dimensions were clean, marked in the middle of

the length to coincide with the center of the punch and positioned in the dimensional margins drawn on the binder. The blanks were fully lubricated on both sides with standard mill oil used for drawing purposes. Two of the blanks were electro-etched with a circle grid (as shown in Fig.3.7), at appropriate distances from the middle of the blank in order to measure the strains in the sidewalls and to compare these with the results predicted by numerical simulation.



Figure 3.7: Electroetching a grid of circles of 0.1(in) diameter onto one side of a blank

Upon opening of the die after forming was finished, the formed channel was removed from the tools and set free to springback to its final shape as shown in Fig.3.8. The channel sidewalls were then 3D measured for each case using a 5-axis milling device with recording capabilities. The IGS files of the measurement data were then created and transferred for final comparison.



Figure 3.8: Sample of channels produced for various drawbead configurations

### 3.2.1 Data acquisition system

In order to measure the force exerted on the punch during the forming stage as well as the displacement of the binder (which is equivalent to the relative punch displacement), several sensors were installed in the A/SP die and connected to a desktop computer with a data acquisition card. The acquisition software was developed in LabView 7.1 and was calibrated for the current project (Fig.3.9).

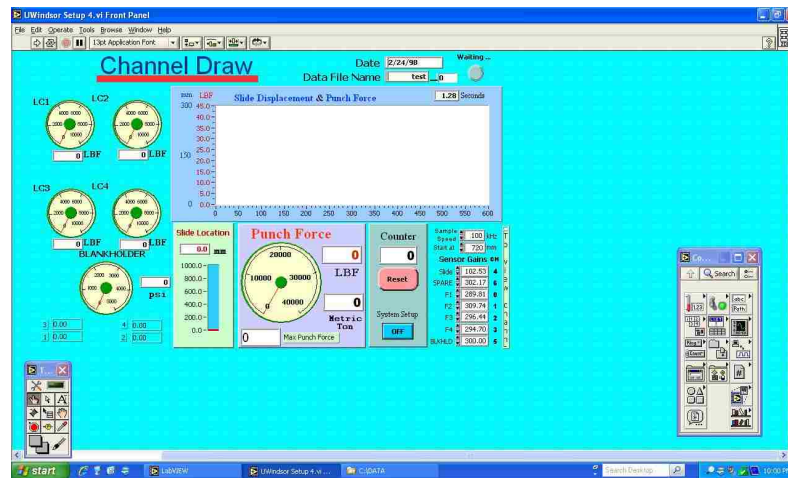


Figure 3.9: Front panel of the data acquisition software

A total of six channels were used from a National Instrument data card (SCB-68) to convert the analog data to digital info which were then recorded by the software. The punch force data were read from four OMEGA load cells (LC305-10K: 0-10,000 lb) situated on the four corners of the lower shoe on which the punch was attached. A BALLUFF linear potentiometer (BIW1-A/M300-S115) was installed on the binder to record its vertical displacement during forming of the channels. Brackets for holding this sensor were attached to the lower die block to ensure its pure vertical movement while this LVDT recorded required data of the forming stroke. An AST pressure transducer (AST4700A05000P5D000 at 0-10V) was connected via a pressure regulator and a connection box to the Nitrogen filled cylinders supporting the binder (Fig.3.10). A 24V-DC power supply was also used to actuate the position and pressure sensors.

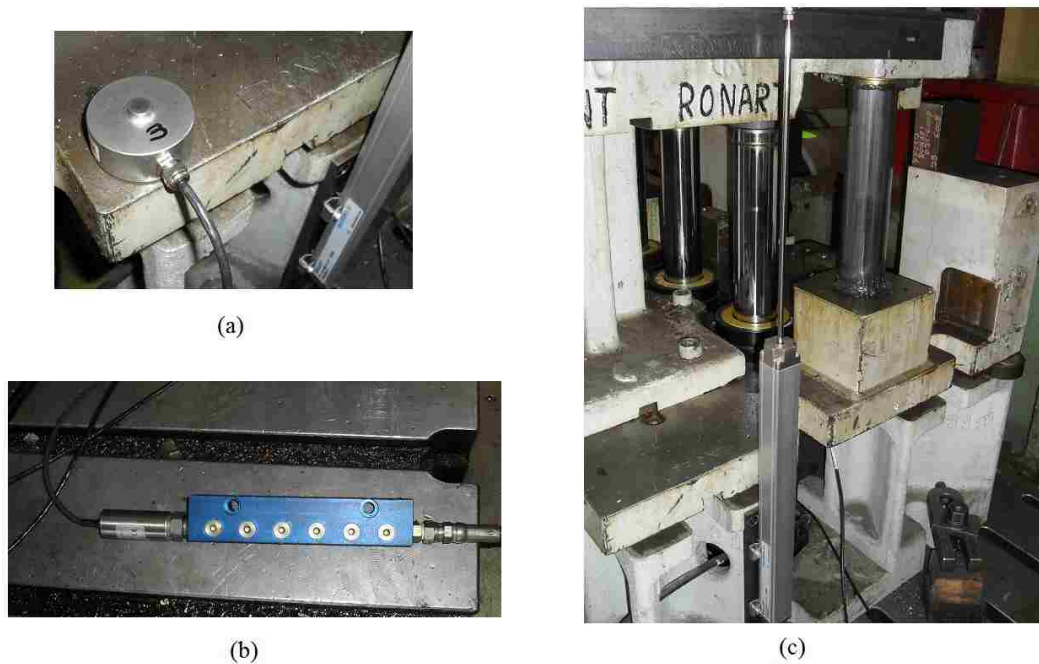


Figure 3.10: Sensors used for the data acquisition: a) OMEGA Load cell, b) AST pressure transducer connected to a junction box, and c) BALLUF linear potentiometer

Known weights were placed on top of individual load cells and the output signal was then calibrated. After installing them under the lower die shoe, gain and bias were finely adjusted. Before each trial, the calibration and data range output of the sensor signals were checked in the measurement configuration module of LabView. The analog output of the load cells was collected by a high performance DP41-S display panel from OMEGA which was also scaled for appropriate monitoring.

Analysis of the first series of experimental data showed that the 10,000 lb load cells were not capable of recording the punch force during forming of DP980 material. Therefore a second series of the experiments were conducted after replacing the 10,000 lb load cells with four sensors rated at 20,000 lb loading capacity. The software and the display panel were then adjusted for the new load cells with appropriate scaling factors. A summary of both series of experimental results is provided here but the second set will be used for comparison with the simulation data in the

next chapter.

### **3.3 Experimental results of channel draw for DP980 and TRIP780**

The experimental results from the channel draw trials for each of the configurations mentioned in Table 3.2 are explained in this section. These results include: punch force vs. displacement curves recorded by the data acquisition system; geometrical parameters derived from the sidewall profile as well as measurements of wall thickness and residual strain distributions. A set of user defined Matlab codes were developed for data interpretation and to produce appropriate results.

#### **3.3.1 Punch force vs. displacement curves**

The total punch force exerted on a blank was the sum of the force data recorded by the four load cells at each corner of the punch. The vertical displacement of the punch with respect to the blank was also identical to the displacement recorded by the LVDT as the blank remained in contact with the binder throughout the forming stage. Graphs for channels made from TRIP780 with shallow(20%), medium (25%) and deep (40%) bead penetrations are shown in Fig.3.11. Results for DP980 with approximately similar bead configurations are shown in Fig.3.12. It should be noted that a constant kiss gap was maintained for each condition as mentioned in Table 3.2 . As shown, the signals from the load cells saturated during the forming of DP980 channel sections. Also a drop in the punch force for deeper penetrations of drawbeads for DP980 is observed which showed non-uniform forming process of these cases. Therefore a subsequent series of experiments were performed for channels with shallow beads for DP980, and the average punch force results that were obtained with load cells with a greater capacity (20,000 lbf each), are shown in Fig.3.13.

### 3.3. Experimental results of channel draw for DP980 and TRIP780 63

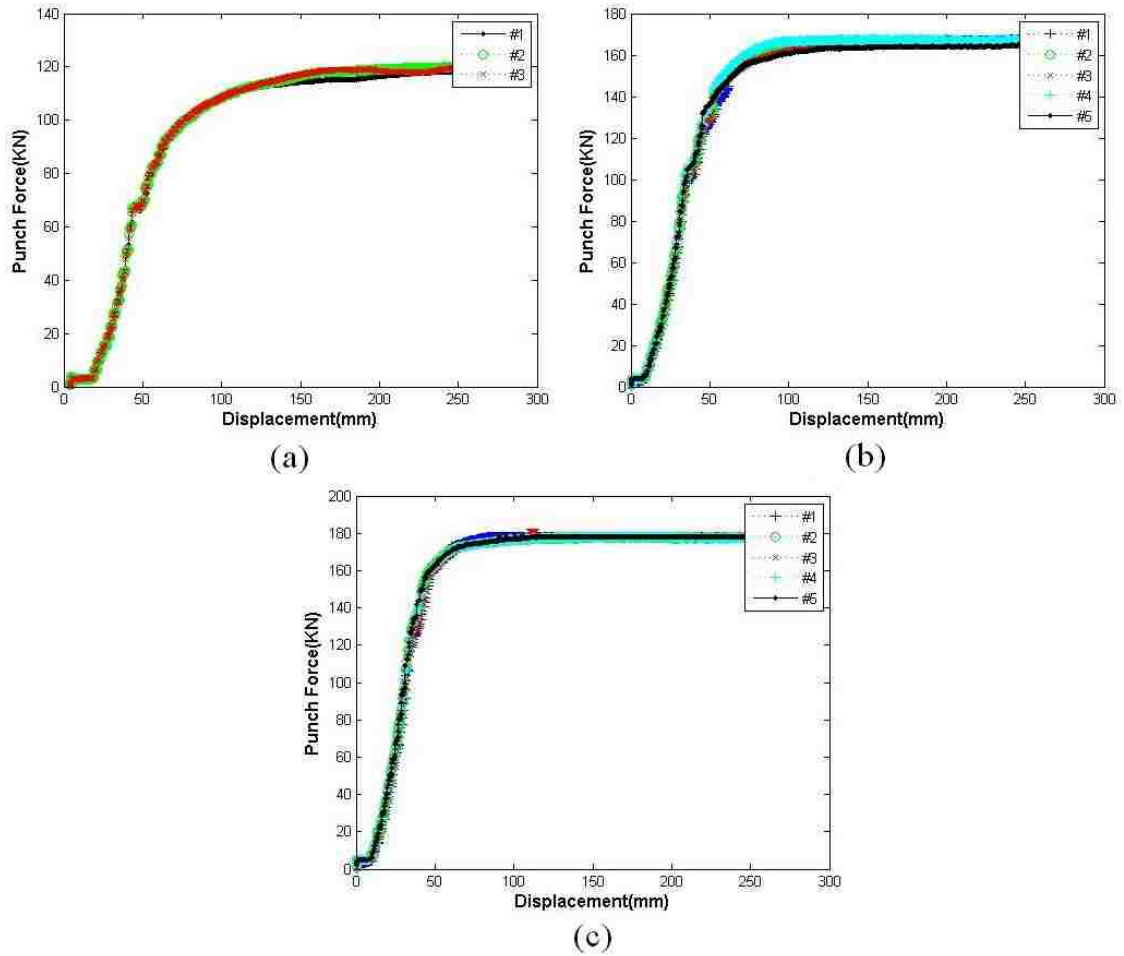


Figure 3.11: Experimental punch force-displacement curves for TRIP780 channels drawn with various drawbead penetrations: a)TPSB (20%), b)TPMB (25%), c)TPDB (40%)

### 3.3. Experimental results of channel draw for DP980 and TRIP780 64

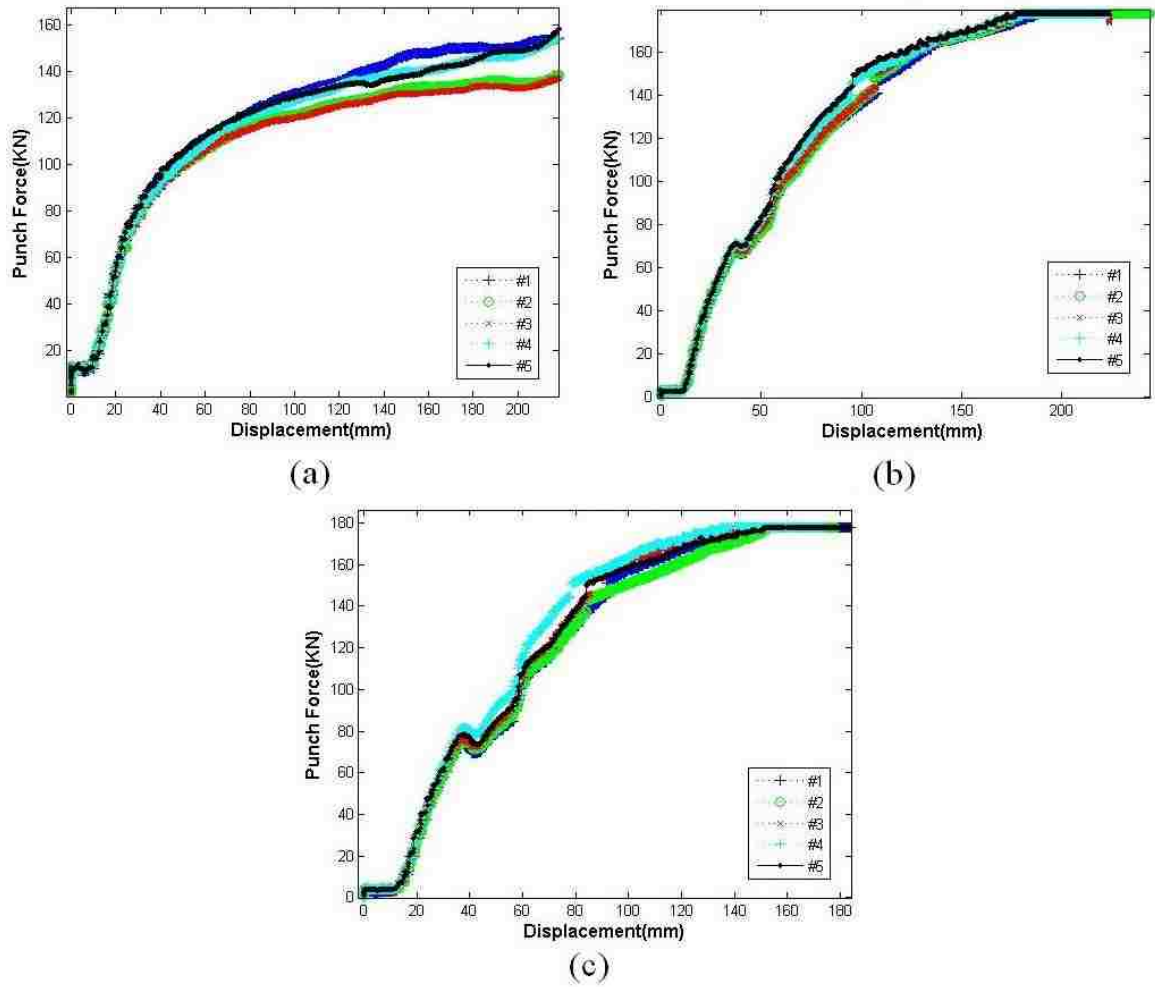


Figure 3.12: Experimental punch force-displacement curves for DP980 channels drawn with various drawbead penetrations: a)DPSB (20%), b)DPMB (25%), c)DPDB (37%)



### 3.3. Experimental results of channel draw for DP980 and TRIP780 65

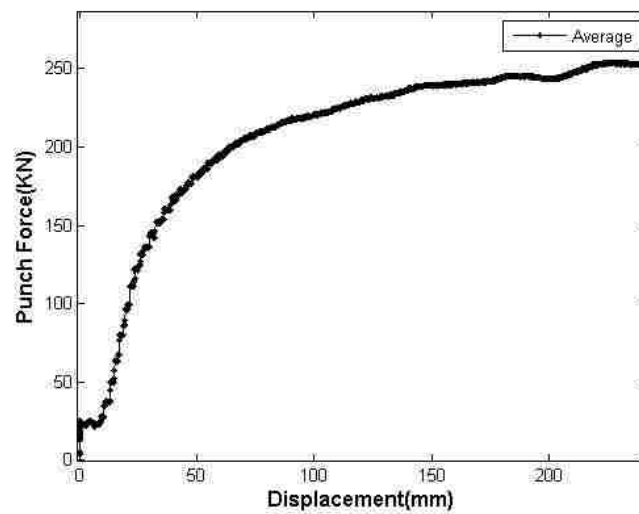


Figure 3.13: Experimental punch force-displacement curve for DP980 channels drawn with a shallow bead penetration (20%)



Figure 3.14: Channels drawn with various die entry radii and without drawbeads

For studying the effect of the die entry radius, a series of tests were performed such that the upper die inserts without drawbeads but with varying die entry radii were used (Fig.3.14). A summary of the specifications for these conditions are given in Table 3.3 and the resultant punch force curves are shown in Figs.3.16 and 3.17. Results of TRIP780 were also compared for channels made of blanks cut both parallel as well as perpendicular to the rolling direction (i.e. Rolling and Transverse

### 3.3. Experimental results of channel draw for DP980 and TRIP780 66

directions). Further comparison of rolling induced anisotropy on the required forming force was also performed with shallow bead penetrations of TRIP780 material and results were compared in Fig.3.15.

Table 3.3: Specifications of channel draw conditions with different die entry radius and no drawbeads

Material Type	adjusted kiss gap (mm)	Die Entry Radius [DER] - (mm)	Symbol
DP980	1.85	12	DPNB12
		6	DPNB6
		3	DPNB3
TRIP780	1.5	12	TPNB12
		6	TPNB6
		3	TPNB3

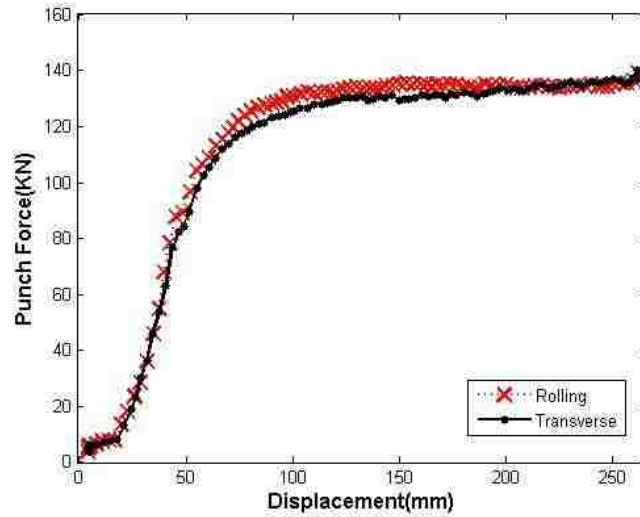


Figure 3.15: Comparison of punch force-displacement curves for TRIP780 channels drawn with shallow bead penetration (20%) when blanks are cut parallel to the rolling and the transverse directions

### 3.3. Experimental results of channel draw for DP980 and TRIP780 67

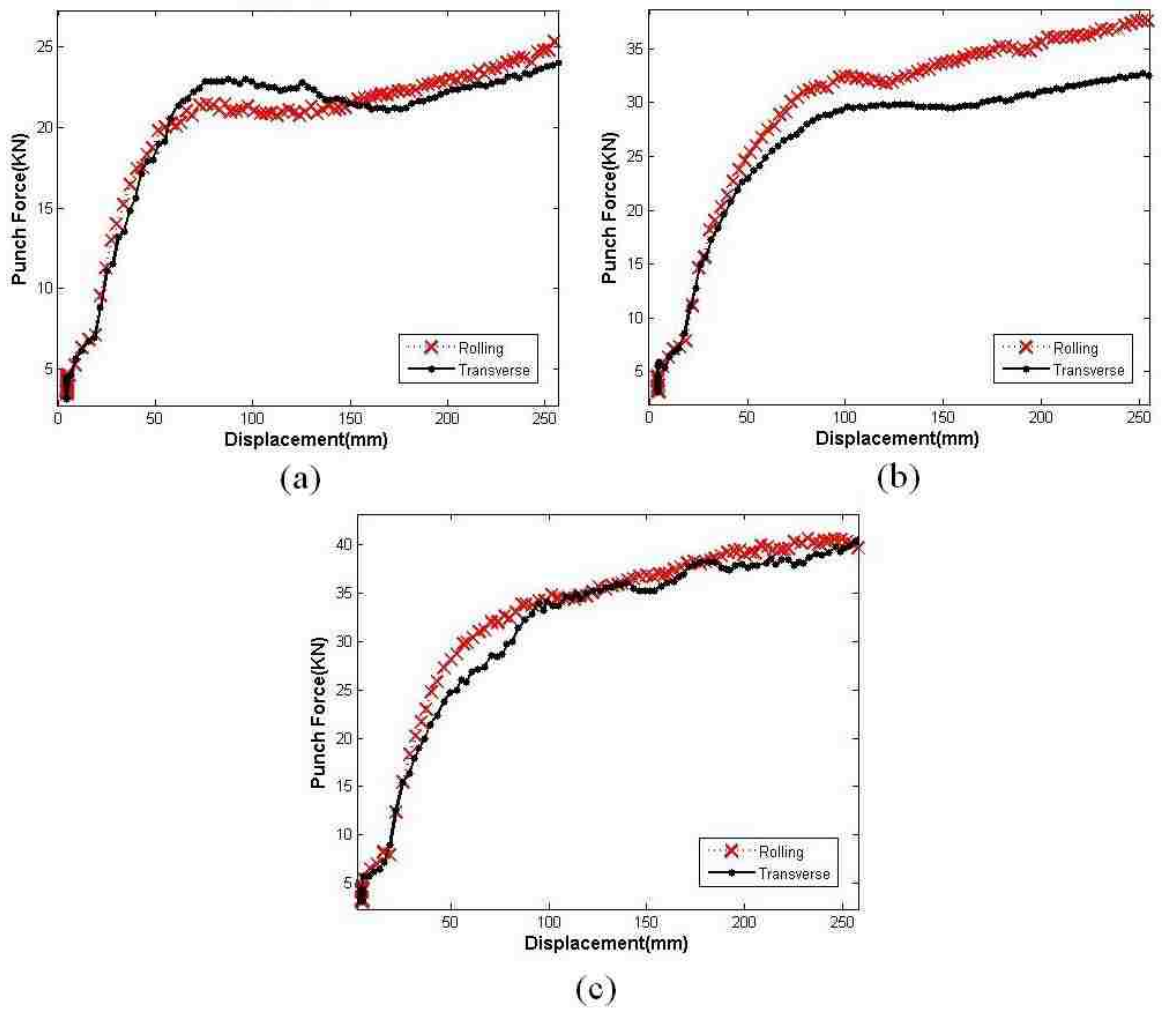


Figure 3.16: Experimental punch force-displacement curves for TRIP780 channels drawn with various die entry radii, and for blanks cut in either the rolling or transverse directions: a)TPNB12, b)TPNB6, c)TPNB3

### 3.3. Experimental results of channel draw for DP980 and TRIP780 68

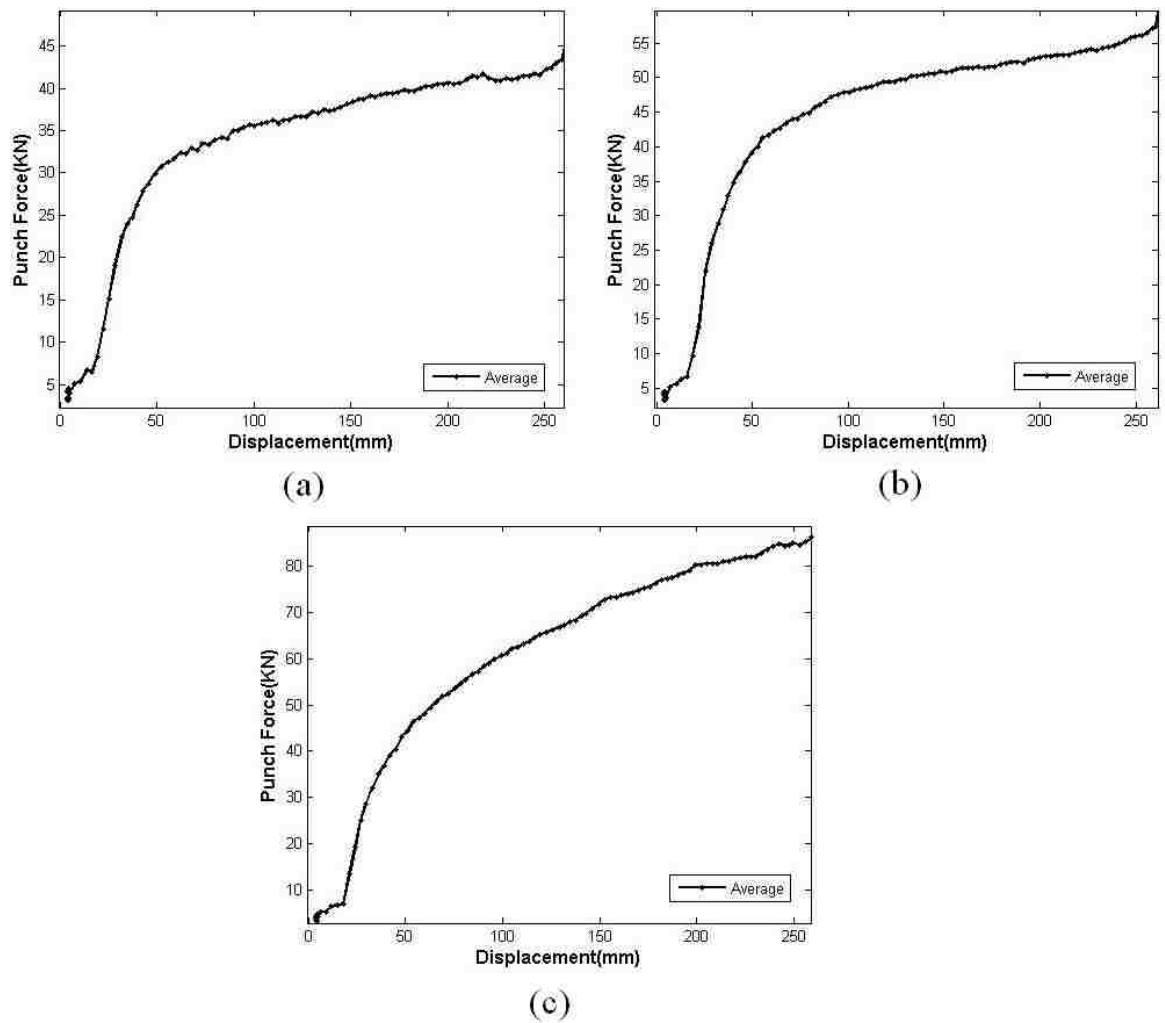


Figure 3.17: Experimental punch force-displacement curves for DP980 channels drawn with various die entry radii: a)DPNB12, b)DPNB6, c)DPNB3

#### 3.3.2 Channel sidewall profiles

After the parts were fully formed and taken out of the die, their sidewall profiles were 3D measured with onsite milling machine with measuring capabilities with maximum error of  $\pm 0.1$  mm. For comparison between channels formed under various conditions, specific features of sidewall curl and springback can be identified: sidewall opening angle, radius of curvature and flange tip angle as defined in Fig.3.18. Repeatability of the experimental results can be observed by comparing the profiles

### 3.3. Experimental results of channel draw for DP980 and TRIP780 69

for each configuration. Figs.3.19 and 3.20 illustrate the sidewall profiles for channels made of DP980 and TRIP780, respectively.

An important observation was made when the sidewalls of channels formed with and without drawbeads were compared. As shown in Fig.3.21, introduction of drawbeads has a major impact on the sidewall curl for both types of materials. The variability in results for DP980 with deeper bead penetrations was due to the fact that these channels were not formed to full depth and therefore were not included for comparison.

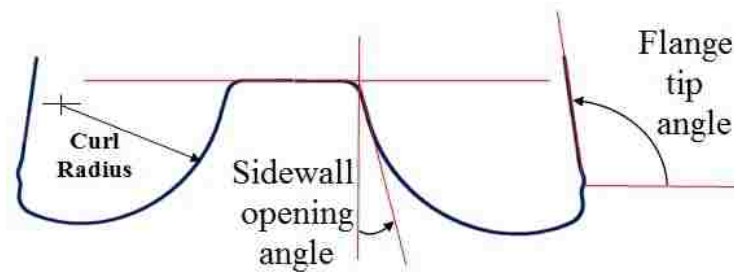


Figure 3.18: Geometrical measures of sidewall curl for channel profile

It can be generally observed that when drawbeads were used, the wall opening angle decreased. It was also observed that channel profiles for TRIP780 with blanks cut parallel and perpendicular to rolling direction, were approximately the same profile within the accuracy of the CMM measurements. Therefore planar anisotropy did not have a significant effect on the final shape of sidewall profiles (Fig.3.22). This was valid both for channels made with and without beads. Due to the shortage of available material, this comparison was not made for DP980.

### 3.3. Experimental results of channel draw for DP980 and TRIP780 70

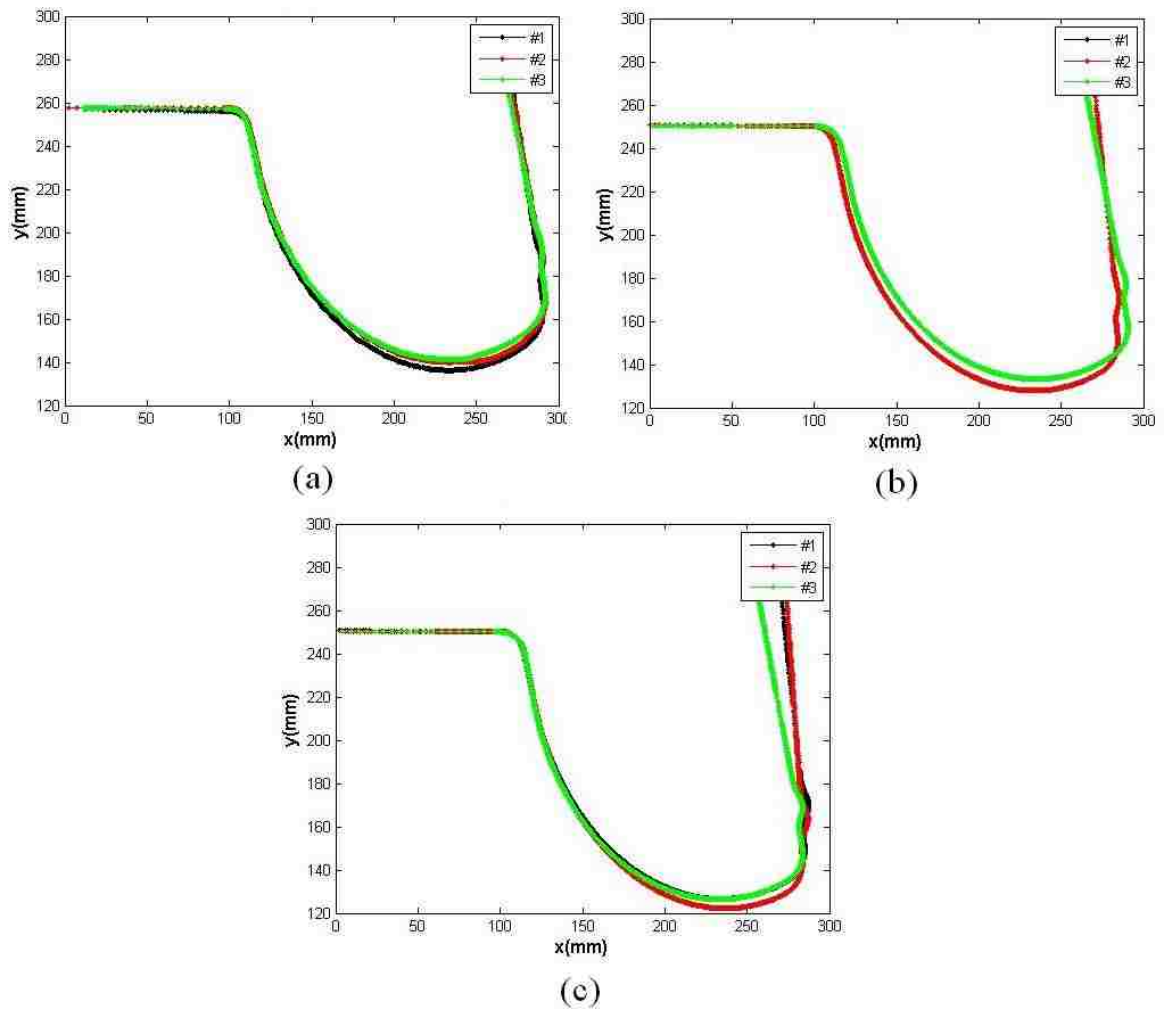


Figure 3.19: Sidewall profiles of TRIP780 channels drawn with various drawbead penetrations: a)TPSB (20%), b)TPMB (25%), c)TPDB (40%)

### 3.3. Experimental results of channel draw for DP980 and TRIP780 71

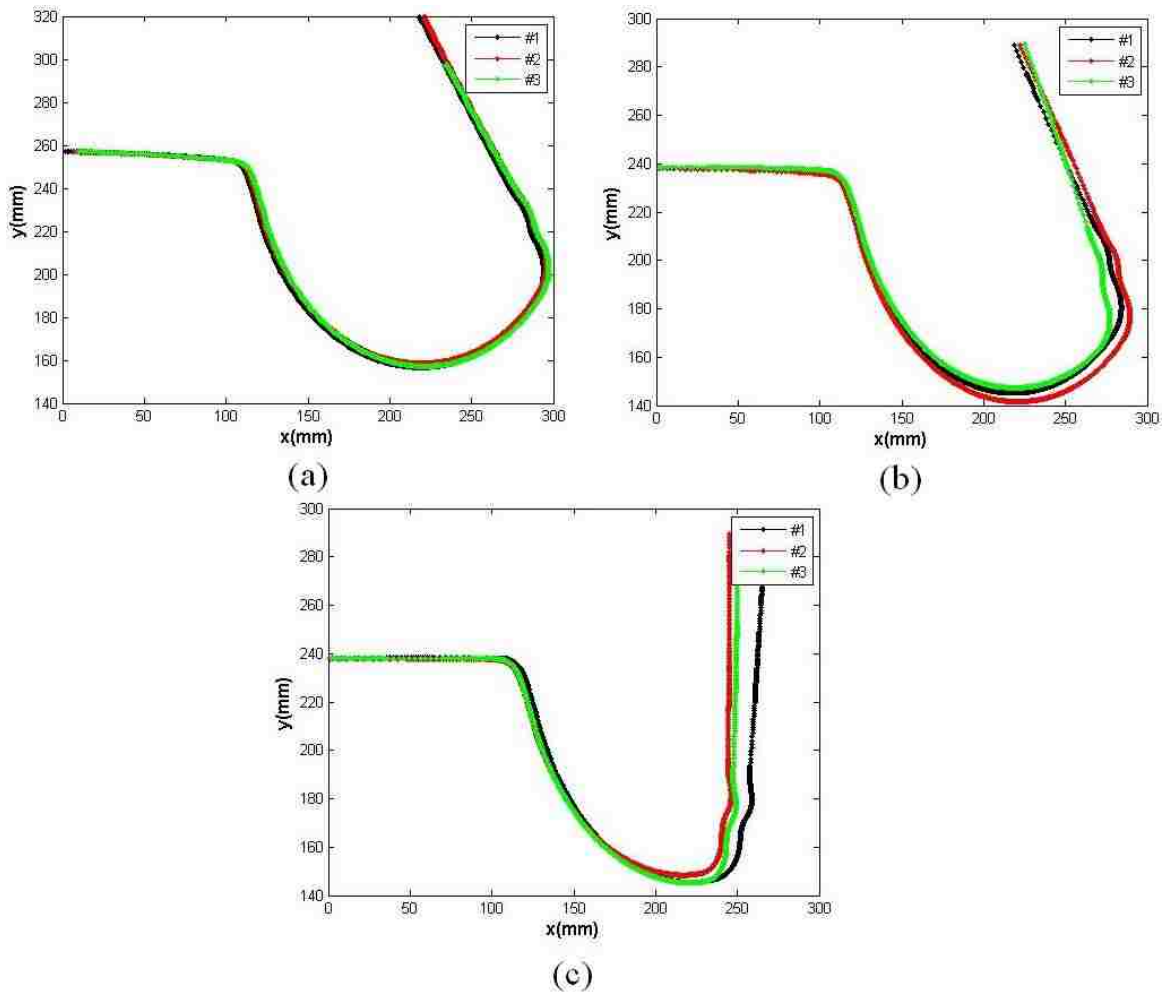


Figure 3.20: Sidewall profiles of DP980 channels drawn with various drawbead penetrations: a)DPSB (20%), b)DPMB (25%), c)DPDB (37%)

3.3. Experimental results of channel draw for DP980 and TRIP780 72

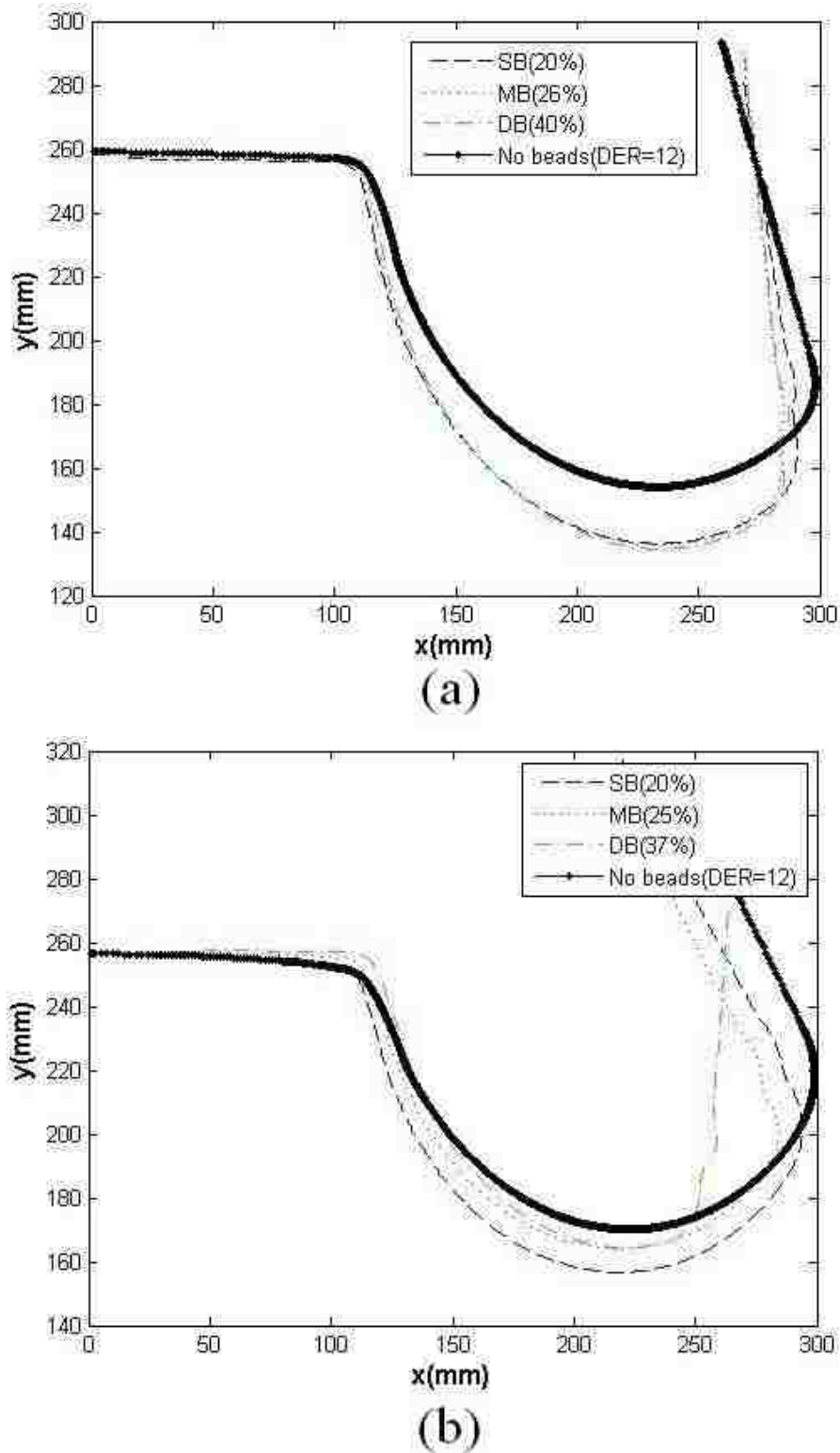


Figure 3.21: Comparison of sidewall profiles for channels drawn with and without drawbeads: a)TRIP780, b)DP980



### 3.3. Experimental results of channel draw for DP980 and TRIP780 73

In this study, the sidewall opening angle, the radius of curvature and the flange tip angle were calculated for each experimental sidewall profile. It should be mentioned that the radius of curvature was approximated for the portion of the sidewall that lies below the die impact line by calculating the best fit of a circular profile, using a Matlab code. Average results of three repeats for each condition of the channel draw experiments are summarized in Table 3.4 . The maximum values of standard deviation of the measurements were  $0.96^\circ$ ,  $1.64^\circ$  and 1.91 mm for the wall angle, the tip angle and the curl radius, respectively. It can be concluded that drawbeads introduce more curl (i.e. decrease wall radius) for both TRIP780 and DP980, but reduce the wall opening angle. Although results for DP980 with the deep bead penetration were not included (as the channels were not formed in a quasi-static condition near the end of the stroke), it is evident that TRIP780 has less sidewall curl and less wall angle than DP980. This is clearly observed for conditions without drawbeads as shown in Figs.3.23.

Table 3.4: Geometrical measures of channel draw experiments for various drawbead penetrations

Condition	TRIP780			DP980		
	Radius (mm)	Wall angle( $^\circ$ )	Flange angle( $^\circ$ )	Radius (mm)	Wall angle( $^\circ$ )	Flange angle( $^\circ$ )
No beads (DER=3)	114	16.7	128	94	27.4	164
No beads (DER=6)	120	20	117	107	25	132
No beads (DER=12)	126	21	107	117	28	122
Shallow beads (20%)	121.3	16.9	103	104	21	124
Medium beads (25%)	116	15.9	100	100	24	117
Deep beads (40%)	114	14.1	98	N.A.	N.A.	N.A.

### 3.3. Experimental results of channel draw for DP980 and TRIP780 74

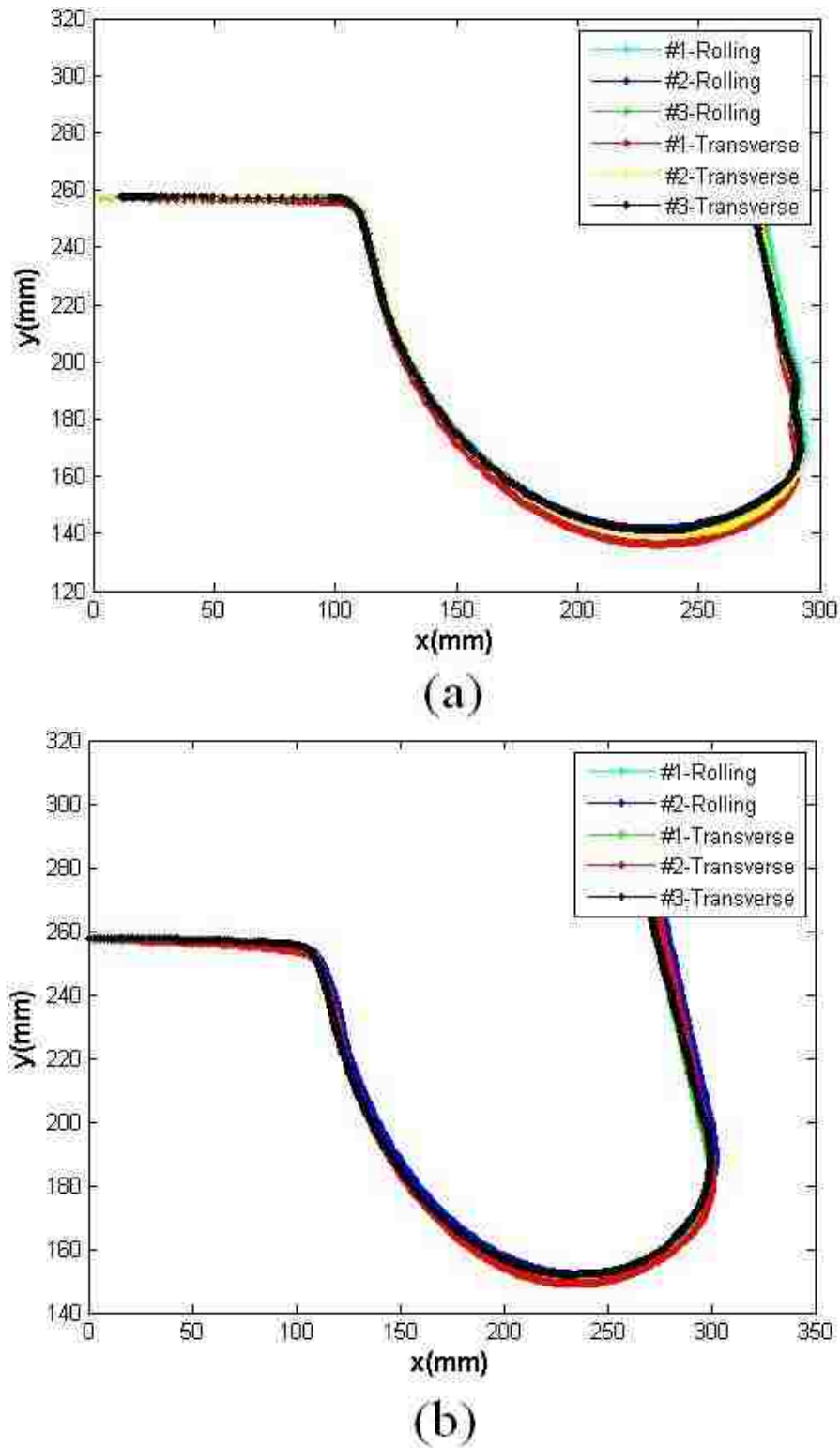


Figure 3.22: Sidewall profiles of channels made from TRIP780 blanks sheared in the rolling and transverse directions: a) with shallow bead penetration (20%) and b) no drawbeads and  $DER=12$  mm

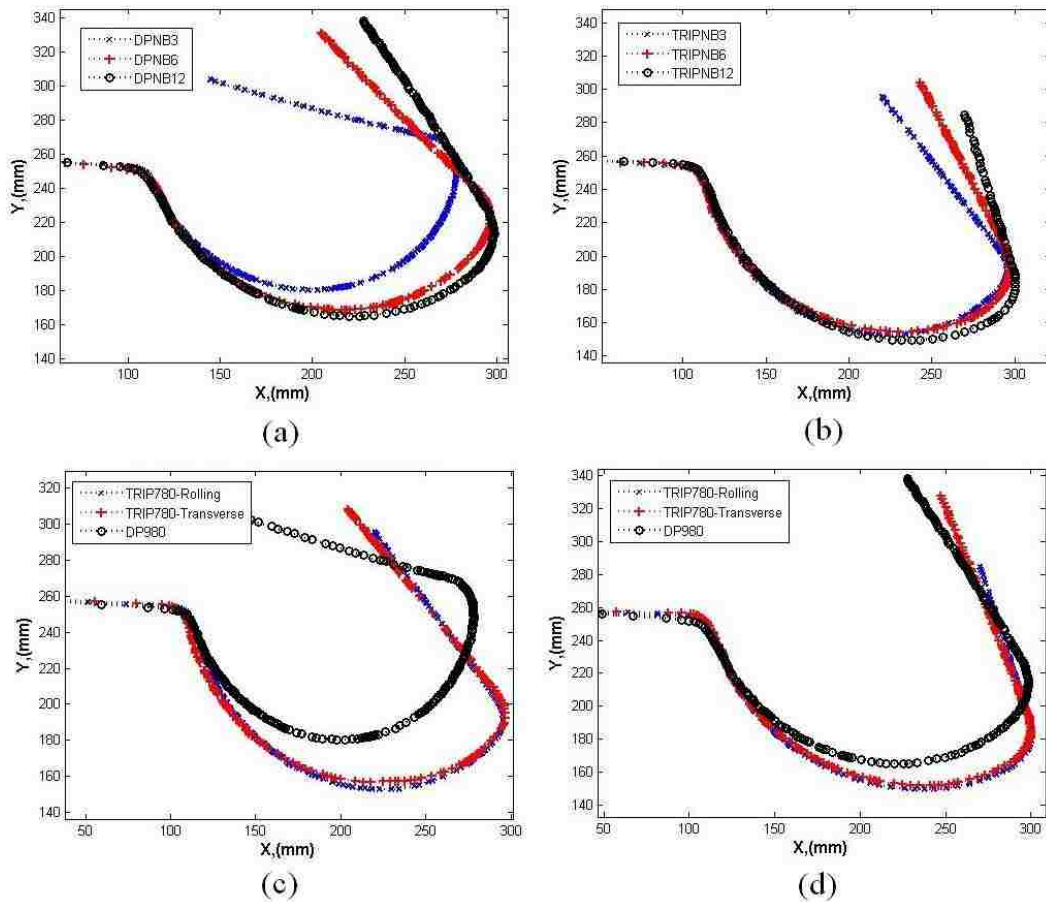


Figure 3.23: Comparison of sidewall profiles for channels drawn with various die entry radii and without drawbeads: a) DP980 with DER=12,6,3 mm, b)TRIP780 with DER=12,6,3 mm, c)TRIP780 in rolling and transverse and DP980 with DER=3mm, d)TRIP780 in rolling and transverse and DP980 with DER=12mm

### 3.3.3 Thickness reduction and strain distribution

After forming channel sections, principal strain measurements were carried out in the channel sidewalls. The major and minor strains were measured in the central part of the RHS channel sidewall (area A in Fig.3.24). These surface strains were measured with a flexible stainless steel ruler over a gauge length of 63 mm for greater accuracy, and the experimental measurement error was  $\pm 0.5$  mm.

### 3.3. Experimental results of channel draw for DP980 and TRIP780 76

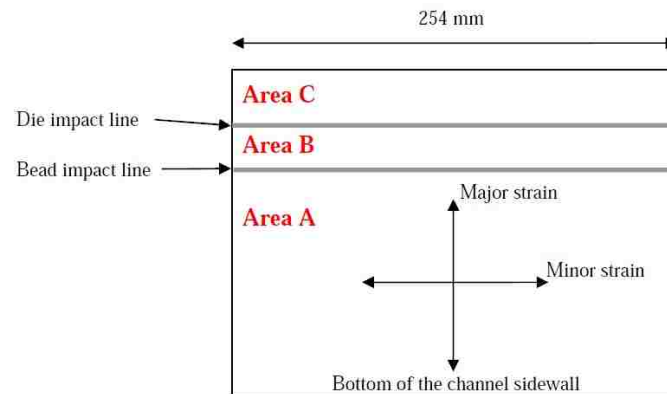


Figure 3.24: Location of surface strain measurements on the channel sidewalls

The thickness strains were measured in several locations uniformly distributed across areas A, B and C of the channel sidewalls (Fig.3.24) using a Krautkramer (CL5) ultrasonic thickness gauge (as shown in Fig.3.25) with a measuring resolution of 0.001 mm. For uniform referencing of these locations, a guide line was marked 20 cm from middle of the blank before deformation. An average of three measurements were done for thickness and principal strain and results were summarized in Table 3.5. Before measuring thickness with the CL5, the instrument and connected probe were calibrated using the zeroing block devised on the instrument, which is of known thickness.

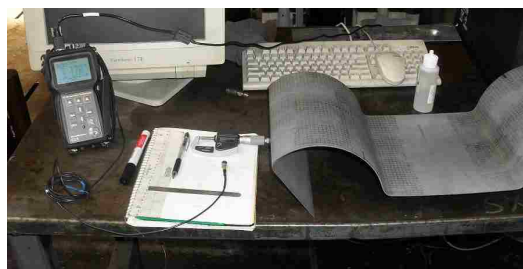


Figure 3.25: Thickness measurement of channel sections using an ultrasonic thickness device

The following observations can be made from the results in Table 3.5:

- Minor strains for all cases were close to 0 (within  $-0.5\% \leq \varepsilon_2 \leq 0.5\%$ ), therefore plane strain deformation prevails the forming conditions.

- Major strains were almost zero ( $\leq 0.8\%$ ) when no drawbeads were used. This confirms that drawbeads increase the major strain in the channel draw.
- When drawbeads were used, differences in thickness strains between areas A & C were observed and maximum sidewall thickness reduction of 8.8% was measured for deep bead penetration for channels made of TRIP780. For channels without drawbeads maximum thickness reduction was 1.25% of nominal stock (for TRIP780 with thickness of 1.2 mm).

Table 3.5: Principal strains and thickness of blanks measured in channel sidewalls. Accuracy of measurement was  $\pm 0.01\%$  strain.

	TRIP780-Rolling			
	Major strain %	Minor strain %	Thickness strain (%)	
			area C	area A
NB12	0.8	0	-0.85	-1.25
NB6	0.8	0	-0.7	-1.0
NB3	0.8	0	-0.75	-1.1
SB(20%)	4	-1.6	-1.0	-5.8
MB(25%)	6.5	-0.4	-0.8	-7.3
DB(40%)	9.8	-0.4	-0.5	-8.8
	TRIP780-Transverse			
NB12	0.5	0	-0.6	-1.0
NB6	0.4	0	-0.7	-0.8
NB3	0.5	0	-1.1	-0.8
SB(20%)	4	-1.5	-1.7	-3.9
	DP980			
NB12	0.8	0	-0.1	-0.6
NB6	0.81	0	-0.4	-0.6
NB3	0.81	0	-0.5	-0.5
SB(20%)	2.4	-0.4	-0.8	-3.4

### 3.4 Material characterization and mechanical properties

The experimental procedures and tests used to determine the mechanical properties of the materials included in this study are discussed in this section. As men-

tioned before, TRIP780 with 1.2mm thickness and DP980 with 1.5mm were used to produce channel sections. In order to characterize the mechanical and anisotropy properties of as-received sheets, specimens were cut at different angles to the rolling direction ( $0^\circ$ ,  $45^\circ$  and  $90^\circ$ ) and sets of uniaxial tension and tension compression tests were conducted.

### 3.4.1 Uniaxial tension tests

The tensile specimens were designed according to ASTM-E8 standard as shown in Fig.3.26 and machined by wire EDM. The tests were conducted to determine the stress-strain curves as well as anisotropy parameters with respect to the rolling direction.

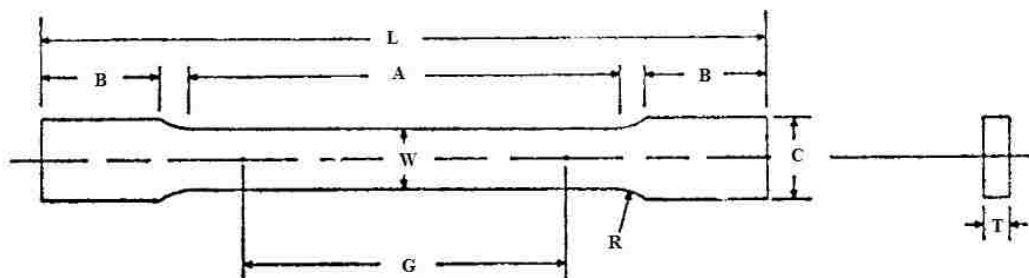


Figure 3.26: Specimen for uniaxial tension test designed according to ASTM-E8:  $G=50$ ,  $W=12.5$ ,  $R=12.5$  (mm)

Two sets of uniaxial tension experiments were performed at separate facilities and results were compared. A group of tests were conducted in an INSTRON 8562 machine at the University of Windsor on samples cut in rolling, transverse and diagonal directions. Extensions were measured by means of a 25.4 mm gauge extensometer along with the applied force at a constant cross-head velocity to maintain quasi-static conditions for the experiments. Recorded data were manipulated in

order to calculate the engineering stress-strain data using:

$$\sigma_{eng} = \frac{F_i}{A_0}, \varepsilon_{eng} = \frac{L_i - L_0}{L_0}$$

where  $F_i$  was the instantaneous tensile load,  $A_0$  the initial gauge cross-sectional area and  $L_0, L_i$  were the initial and instantaneous gauge length, respectively. True values of stresses and strains were then calculated considering constant volume assumption during plastic deformation, as:

$$\sigma = \sigma_{eng}(1 + \varepsilon_{eng}), \varepsilon = \ln(1 + \varepsilon_{eng})$$

Results of tensile tests for TRIP780 and DP980 are shown in Fig.3.27. It was observed that the stress-strain curves obtained from different orientations of the specimens are almost identical. Specimens showed consistency in their response for each orientation with respect to the rolling direction. It can be observed that the 45° specimens experience lower stresses than the 0° and 90° test specimens. Moreover, there was no significant difference between the behaviours of the latter two directions. These results were observed for DP980 as well as TRIP780.

The yield stress of the specimens were obtained from the stress - strain curves at a strain offset of 0.002. It was then used to determine the true stress - plastic strain curve required for simulation models using:

$$\varepsilon_P = \varepsilon - \frac{\sigma_Y}{E},$$

where  $\sigma_Y$  is the yield stress and  $E$  is the initial elastic modulus, assumed to be 207 GPa for both types of steels. The elastic modulus was also estimated by a linear fit to the beginning portions of the uniaxial test results between stresses of 0 and 200 MPa. The tangential modulus that was measured by this method ranged from 195 to 208 GPa for DP980 and 192 to 210 for TRIP780. The uniaxial curves were then averaged to a final flow curve up to the maximum strength for each material

type and compared with results from other sources. The second series of tensile tests were performed at US Steel, Automotive Center Laboratory, MI, in which anisotropy ratios were also measured. As mentioned in Chapter 2, at a given angle  $\phi$  to the rolling direction, the anisotropy of the sheet is characterized by the plastic strain ratio, r-value, and is defined as:

$$r_{\phi} = \frac{-\varepsilon_W}{\varepsilon_L + \varepsilon_W} = \frac{-\ln(\frac{W}{W_0})}{\ln(\frac{L}{L_0}) + \ln(\frac{W}{W_0})}$$

It is common to describe an average r-value,  $\bar{R}$ , (Hertzberg, 1995) obtained from three directions  $0^\circ$  (parallel),  $45^\circ$  (diagonal) and  $90^\circ$  (transverse) to the rolling direction that describes the normal anisotropy and is defined as:

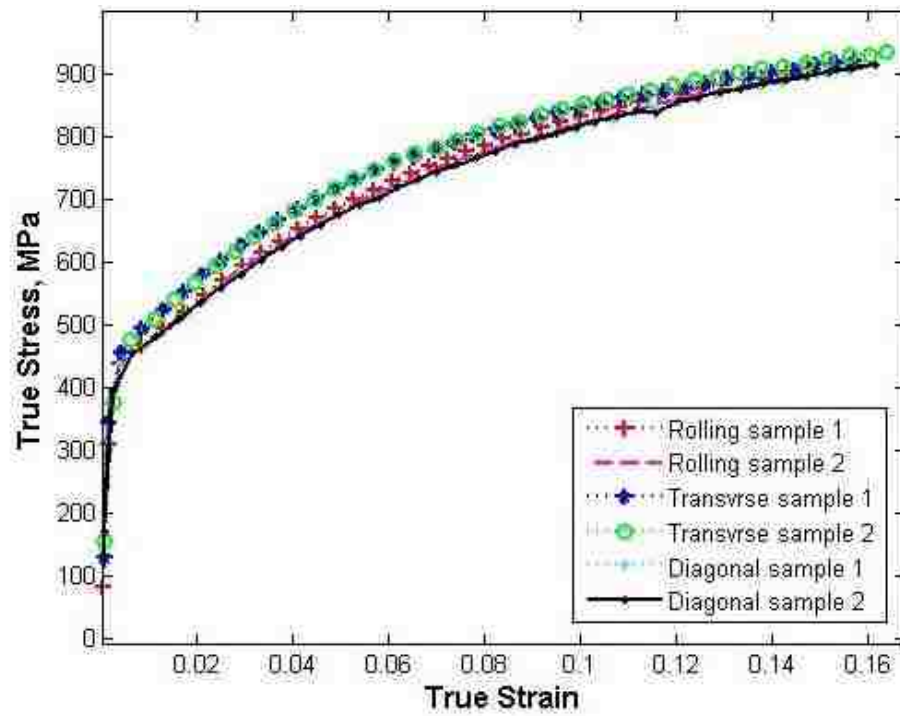
$$\bar{R} = \frac{r_0 + 2r_{45} + r_{90}}{4} \quad (3.1)$$

Also  $\Delta R$ , defined as a measure of the tendency of the sheet to draw in nonuniformly and form ears in the flange of deep-drawn cylindrical parts in the direction of the higher r-value was calculated by:

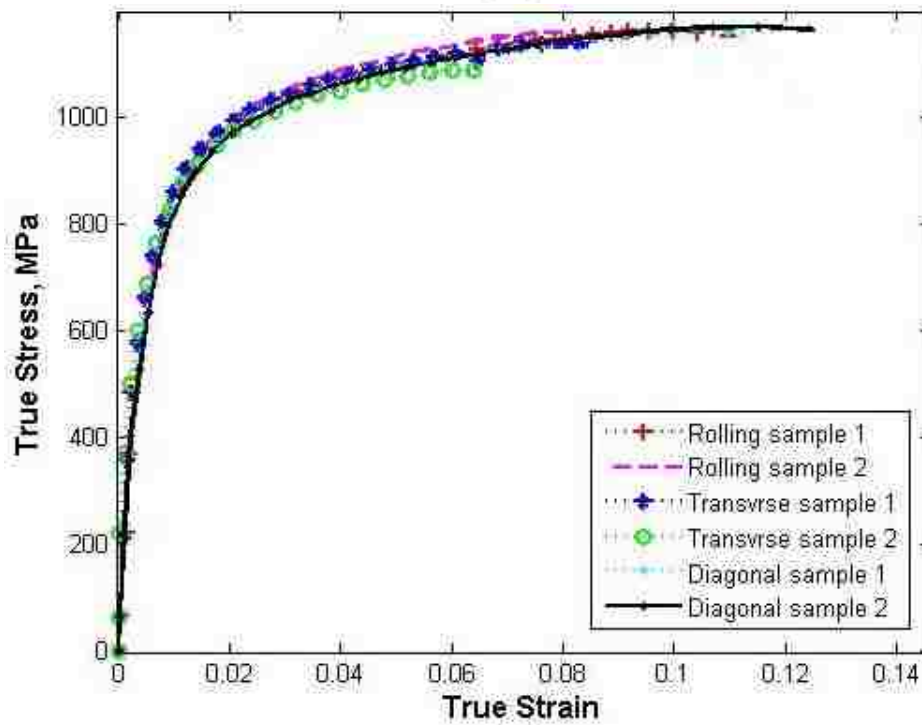
$$\Delta R = \frac{r_0 + r_{90} - 2r_{45}}{2} \quad (3.2)$$

Results from uniaxial tensile tests performed at USS are summarized in Table 3.6. It can be seen that the effect of orientation on the yield stress is relatively small. Therefore an average value of the yield stress can be used to characterize these two sheet steels. Also the plasticity curves obtained from tensile tests on samples in the rolling direction were compared with those performed at University of Windsor, as well as the power law  $\sigma = K * \varepsilon^n$ , as shown in Figs.3.28 and 3.29. The consistency between the results was reasonably good, therefore an average curve from the uniaxial test results was used to obtain a best fit of the power law function for each grade of steel, and these were used as input data in the numerical simulations.





(a)



(b)

Figure 3.27: Uniaxial tension test data obtained at the University of Windsor: a)TRIP780 and b)DP980

Table 3.6: Summary of mechanical properties measured by tensile tests at USSteel, R, T, D stand for the Rolling, transverse and diagonal directions of the blank, ASTM A370 and E8 test method with 50.8 mm gauge length; r-value based on ASTM E517; n-value based on ASTM E646

Material	ID	Thickness	Yld Strgth	Tensile Strgth	n-value	K	Strain range	r, $\Delta R$
Type		(mm)	0.2 % (MPa)	(MPa)		(MPa)	for n, K	
DP980	R	1.499	638.	1088.	0.104	1542	2.0 - 8.1%	0.96
	T	1.483	689.	1082.	0.112	1595	2.0 - 5.4%	0.56
	D	1.501	641.	1069.	0.114	1573	2.0 - 6.3 %	0.79
Avg (R+2D+T)/4		1.496	652.	1077.	0.111	1571		0.78/-0.03
TRIP780	R	1.176	451.	794.	0.202	1348	10.0 - 18.0%	0.65
	T	1.166	462.	808.	0.180	1320	10.0 - 16.9%	0.89
	D	1.176	443.	779.	0.191	1295	10.0 - 17.7%	1.00
Avg (R+2D+T)/4		1.173	449.	790.	0.191	1315		0.89/-0.23

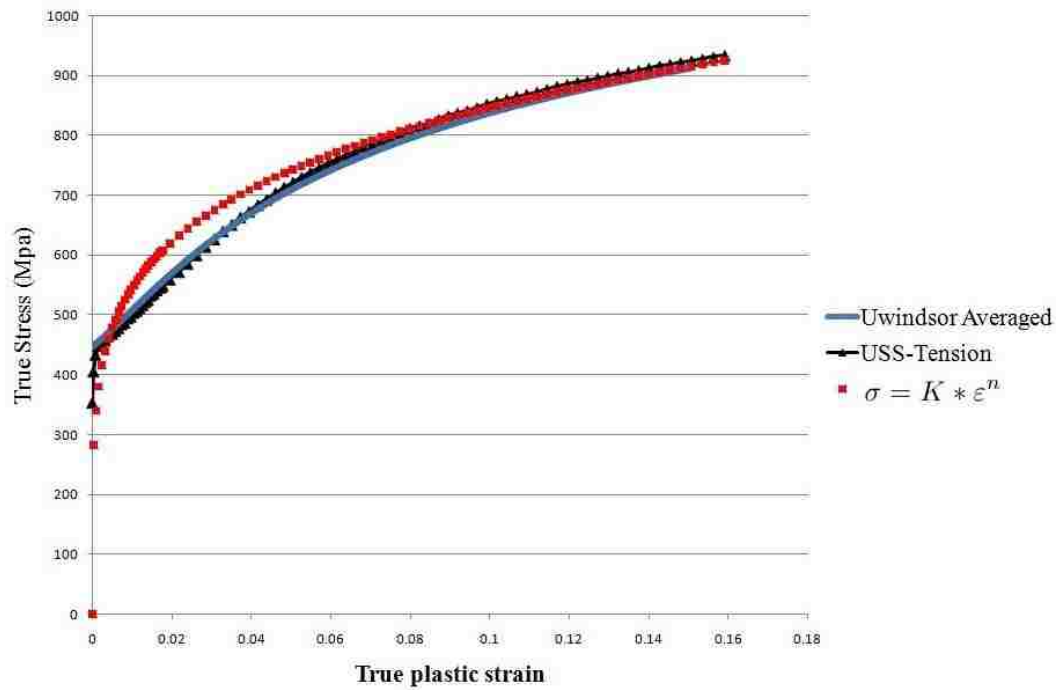


Figure 3.28: Plasticity curves for TRIP780 from uniaxial tests performed at University of Windsor, USSteel and a power law curve

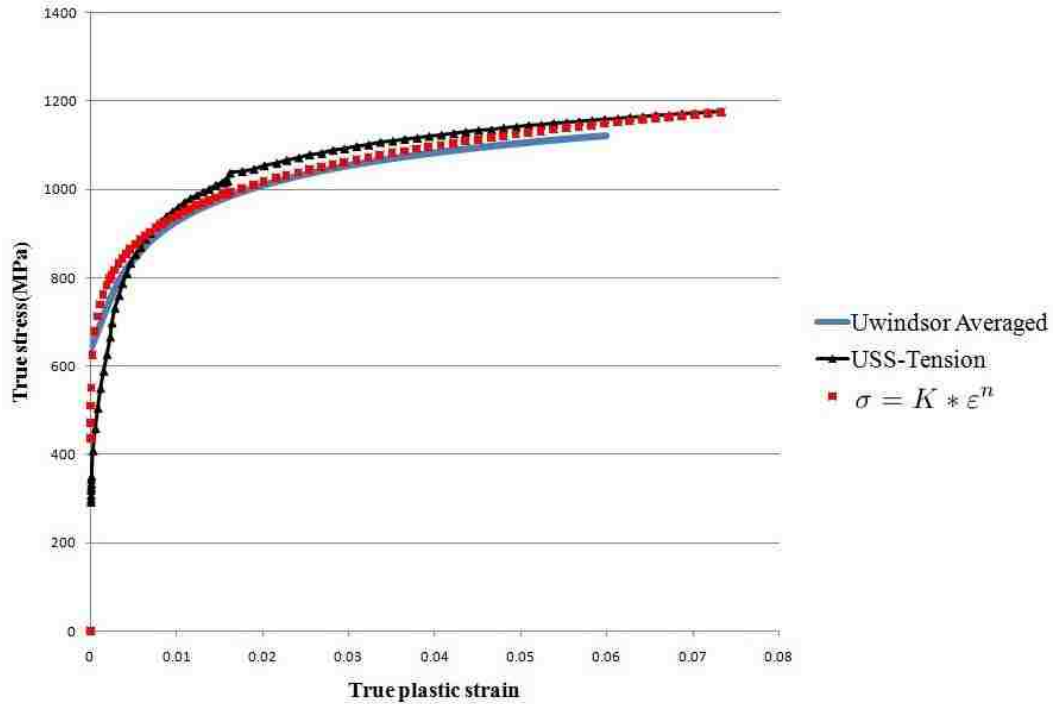


Figure 3.29: Plasticity curves for DP980 from uniaxial tests performed at University of Windsor, USSteel and a power law curve

### 3.4.2 Unloading elastic modulus

A series of uniaxial tests were performed on samples taken parallel to the rolling direction in order to study the evolution of the unloading elastic modulus of TRIP780 and DP980 sheet metals. Specimens were prepared according to the ASTM E8 standard, and tests were performed at the Colorado School of Mines. A series of specimens were strained to 1.5%, 2.5%, 3.5% and 4.5 % before they were unloaded, as it was expected from previous studies [36] that the unloading modulus follow an exponential decay function with saturation between 3 to 4% initial strain for high strength steels (such as DP600). For each material, tests were repeated three times for each of the prestrain levels. Representative engineering stress-strain curves of one set of the tests are shown in Figs.3.31.

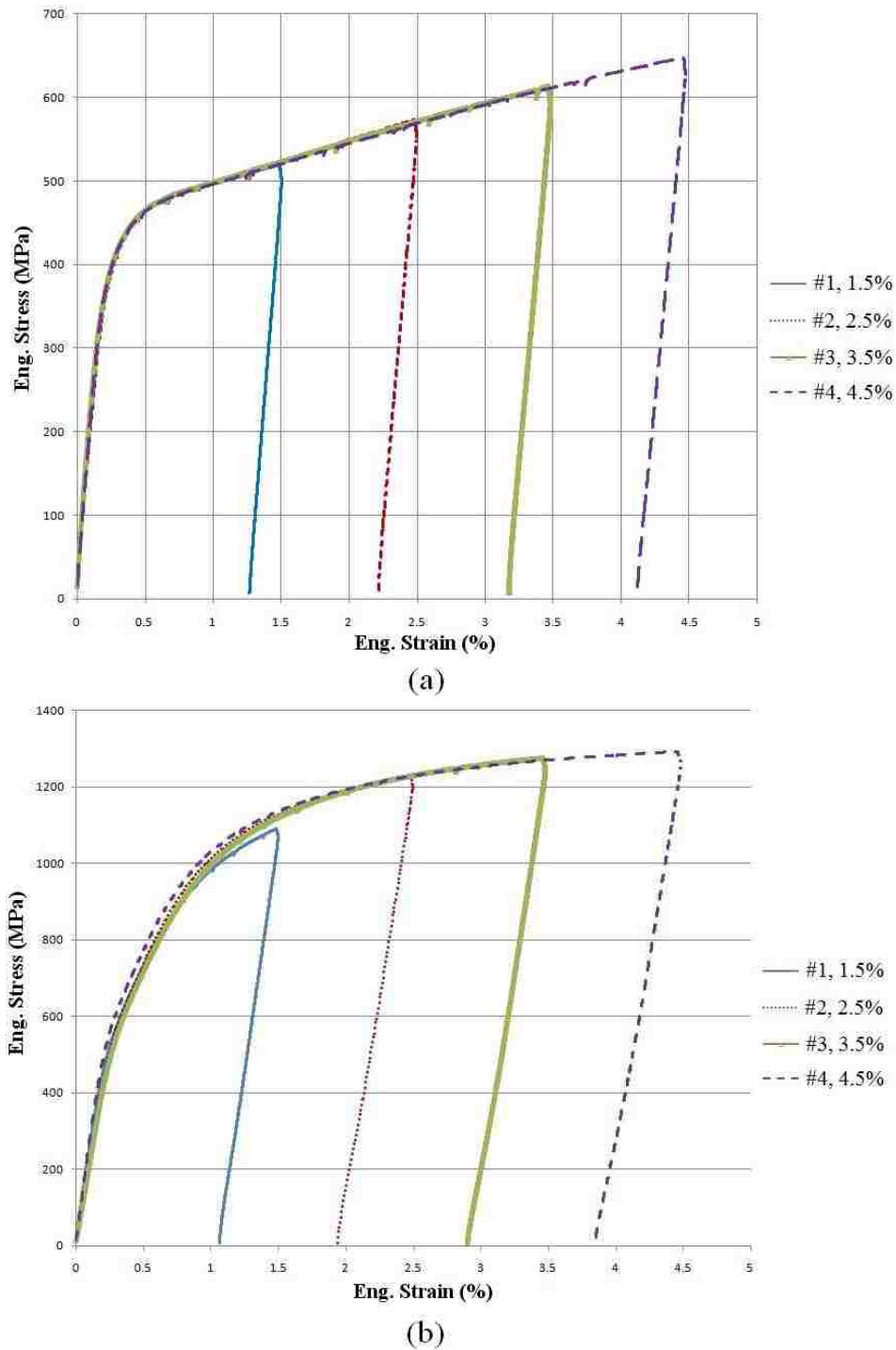


Figure 3.30: Engineering stress-strain curves for unloading elastic modulus of a)TRIP780 and b)DP980, performed at the Colorado School of Mines

Several user-developed Matlab functions were used to estimate the loading and

unloading elastic modulus of the experiments according to the criteria defined in Chapter 2, section 2.3.1. A sample of the output graphs for nominal engineering prestrain level of 4.5% for each material type is shown in Fig.3.31. Analysis of the average unloading modulus revealed a non-linear decrease with respect to prestrain levels with considerable scatter in the results. In order to minimize the effect of scattering, effective values for each level of pre-strain was calculated as in Table 3.7. The average data for each material type was fitted to the decaying function, Eq.2.18. The parameters of the best fit to this equation for each material type are summarized in Table 3.8.

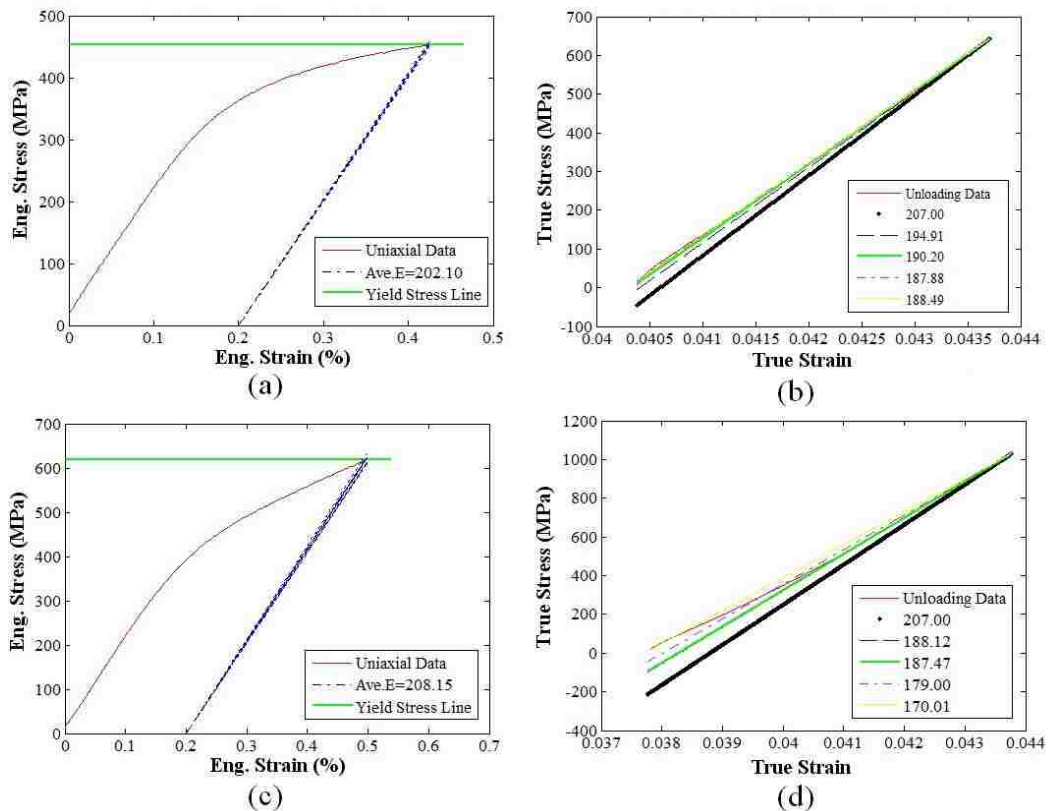


Figure 3.31: Sample calculation of elastic modulus from stress-strain curves: a) Initial elastic modulus of TRIP780, b) unloading elastic modulus of TRIP780, c) Initial elastic modulus of DP980, d) unloading elastic modulus of DP980.

Table 3.7: Average experimental results for Unloading Elastic Modulus, calculated from prestrained specimens up to 4.5% strain, obtained from the Colorado School of Mines

	Nominal strain level	plastic pre-strain $\varepsilon_0$	Unloading Stress level (MPa)	Average Unloading Elastic Modulus (GPa)
DP980	1.5%	0.010	888.5	199.5
	2.5%	0.019	1009.9	193.3
	3.5%	0.028	1061.2	185.3
	4.5%	0.038	1083.5	181.2
TRIP780	1.5%	0.012	527.7	211.7
	2.5%	0.021	587.8	200.0
	3.5%	0.031	634.7	198.2
	4.5%	0.040	677.2	190.4

Table 3.8: Identified parameters for decay formula of unloading elastic modulus for prestrains up to 4.5%

	$E_0$ (GPa)	$E_{sat}$ (GPa)	$\xi$	Fit $R^2$	RMSE
TRIP780	210.7	160.3	16.58	0.768	3.978
DP980	200	158	11.27	0.894	1.712

However, it should be mentioned that prestrain levels in the aforementioned experiments were not sufficient to identify the saturated value for the unloading elastic moduli. It is expected to observe even more decrease in the unloading modulus even up to strains of 0.1. It is anticipated that the limited amount of ferrite in DP980 and the transformation from austenite to martensite in the TRIP steel are responsible for the difference with other high strength steel grades such as DP600. From a metallurgical perspective, it was thought that the saturation is related to the amount of deformed ferrite. Once a critical amount of strain is reached, the ability of the dislocations in the ferrite to relax upon unloading becomes more or less constant, leading to a fixed amount of decrease in the unloading modulus. It should be mentioned that the tests were done at sufficiently slow rates that adiabatic heating and the time dependency of the unloading modulus should not affect the results.

In order to identify the difference in the behaviour of TRIP780 and DP980, another set of experiments was performed on specimens prepared in similar fashion. For each material a single specimen was loaded and unloaded in multiple cycles up to higher strain levels than 4.5% as shown in Figs.3.32 with a detailed graph showing how the slope of the secant line to the nonlinear unloading path was calculated. By fitting the data points of unloading elastic modulus vs. effective plastic strain to the analytical function proposed by Yoshida (Eq.2.18), saturated values for unloading elastic modulus and the decaying coefficient were identified for each material type, as shown in Fig.3.33. The identified parameters are summarized in Table 3.9. The coefficients of determination,  $R^2$ , for both fitted curves to the unloading data are positive values of 0.66 and 0.68 for TRIP780 and DP980, respectively. These values suggest that the goodness of the fit is not as strong as could be expected. This is also evident from the deviation of the data points from the fitted curve and the decrease in the unloading modulus even at higher plastic strains. However, the confidence intervals are not wide and reasonably near the estimated values of the saturated unloading moduli of the materials. Further studies in this regard have shown a linear relationship between the unloading modulus and the strength of the material just before the unloading for both TRIP780 and DP980. However this relation is not yet implemented in a material model. Therefore, the identified parameters from Table 3.9 were used in the simulation part of the current study.



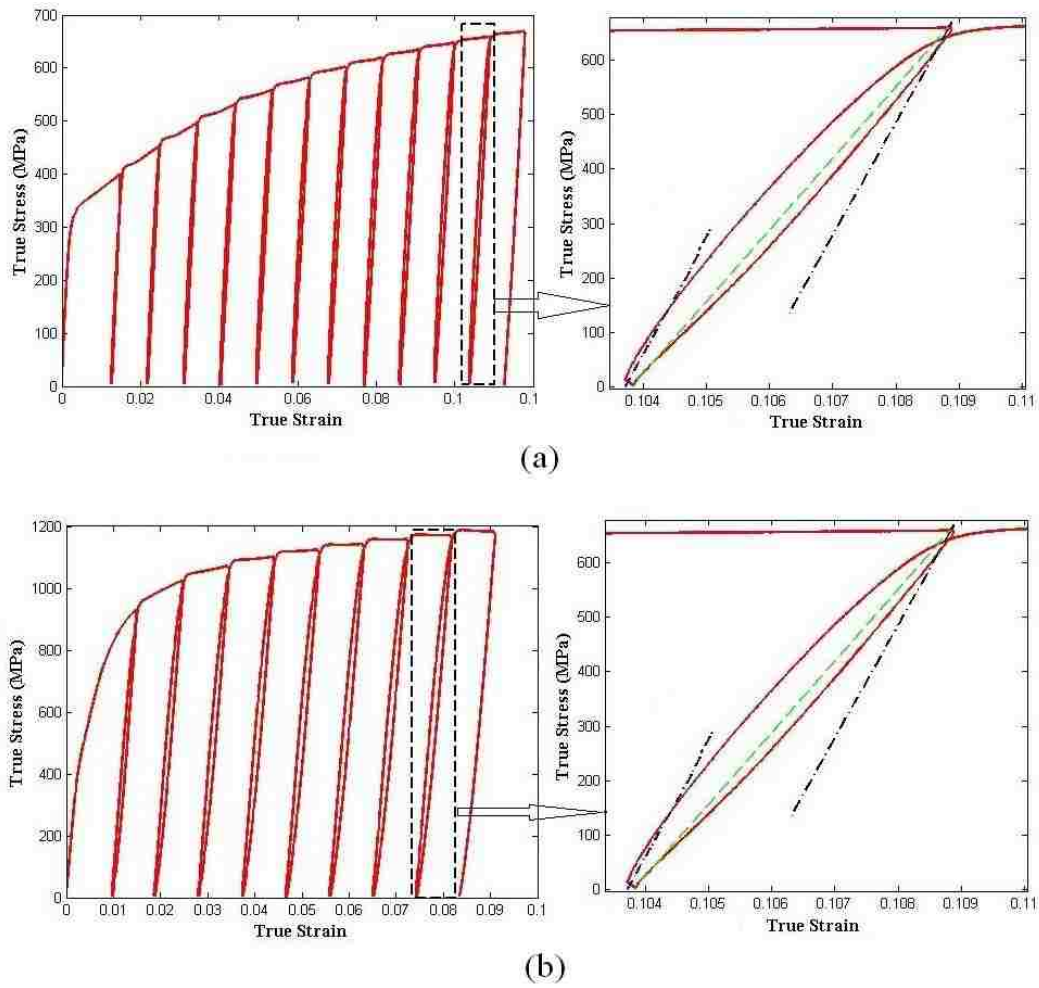


Figure 3.32: Multiple loading and unloading cycles performed at the Colorado School of Mines to estimate saturated unloading elastic modulus: a)TRIP780, b)DP980

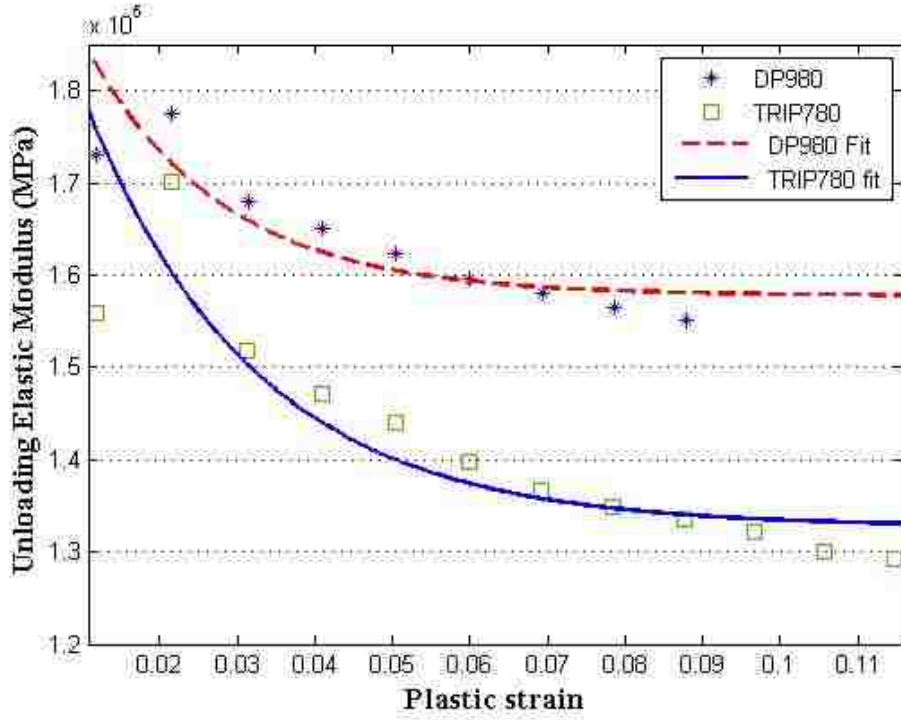


Figure 3.33: Fitting analytical decay function to unloading elastic modulus of TRIP780 and DP980

Table 3.9: Identified parameters for decay formula of unloading elastic modulus with prestrain 12% for TRIP780 and 9% for DP980

	$E_0$ (GPa)	$E_{sat}$ (GPa)	$\xi$	Fit $R^2$	95% Confidence interval (GPa)	$E_{sat}$
TRIP780	207	132.7	46.1	0.665	(124.8, 140.6)	
DP980	207	157.8	57.5	0.682	(151.6, 163.9)	

In a recent study presented by Kuwabara at the ESAFORM conference in Belfast, 2011, the unloading modulus data for DP980 saturated at an effective strain around 0.1. The equation provided was :

$$E(\text{MPa}) = 153.934 + 53.918 * e^{(-57.4 * \epsilon_p)} \quad (3.3)$$

The values reported in Eq.3.3 are in good agreement with the parameters found

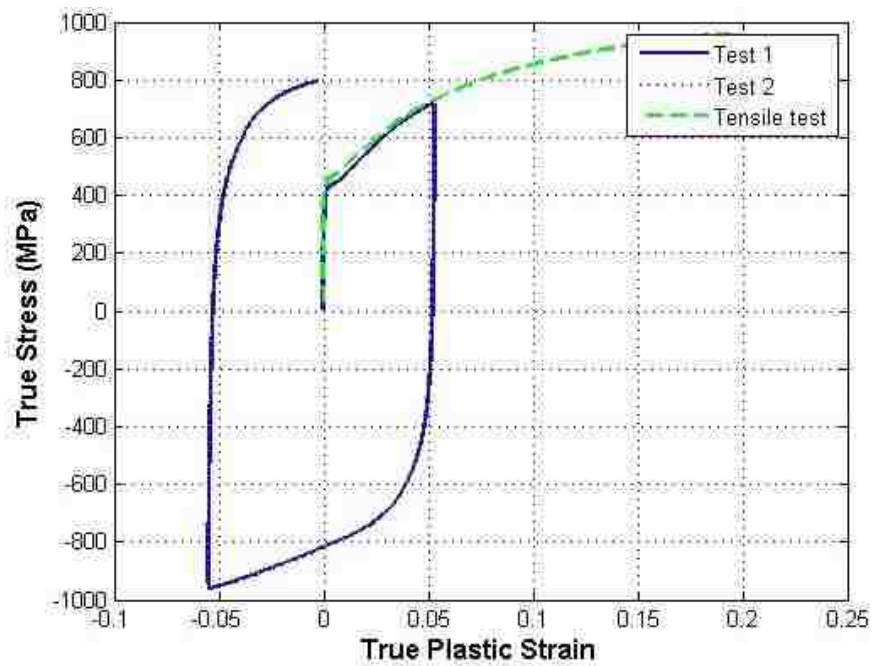
in the current study. The identified unloading parameters from Table 3.9 are used for the parameters optimization study in the subsequent chapter.

### **3.4.3 Cyclic Tension and Compression tests**

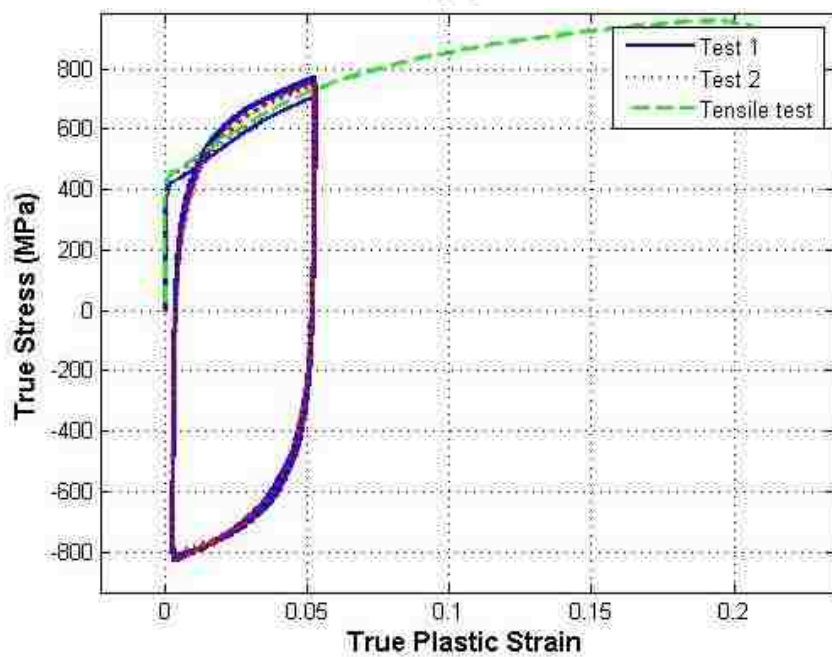
Different tension and compression tests were performed at USSteel on tensile samples of DP980 and TRIP780 in order to identify material hardening parameters. These tests included :

- a single cycle tension and compression test starting in tension and then, at a certain strain level, reversing to compression until the strain reaches zero;
- a single full cycle tension and compression test starting at tension and then, at a certain strain level, reversing to compression until the compression strain reaches the same amount of positive strain in tension and at this compression strain level, re-loading in tension until the net strain reaches zero
- a multiple cycle tension and compression test repeating a single cycle tension and compression test several times.

For each material type, all of the tests were repeated twice. Results of the single and multiple cycles until zero strains (type 1 and 3) were identical. Therefore results of complete single cycle as well as multiple cycles are shown in Figs.3.34 and 3.35. Strain memory as well as prestrained tension and compression tests were not performed.

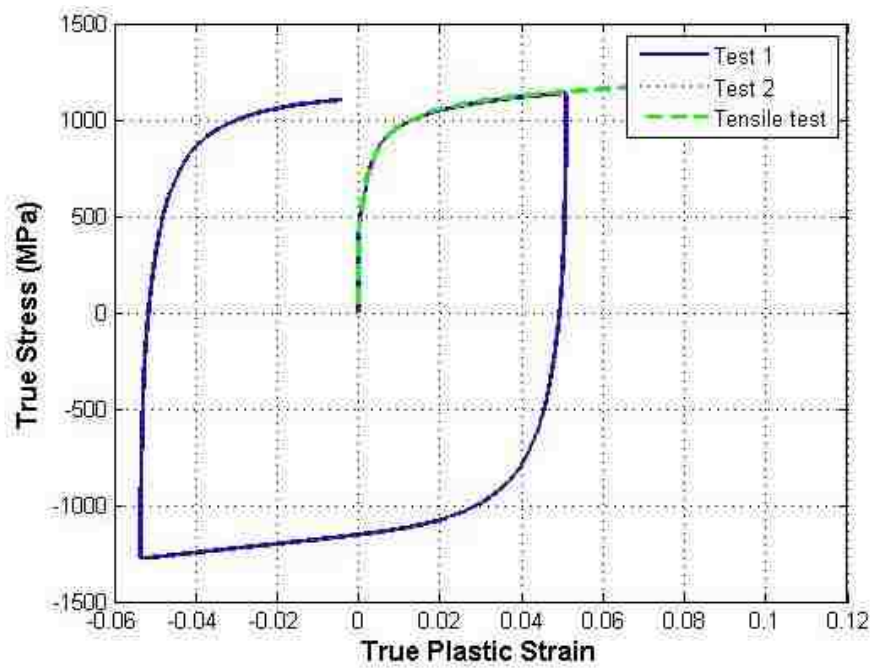


(a)

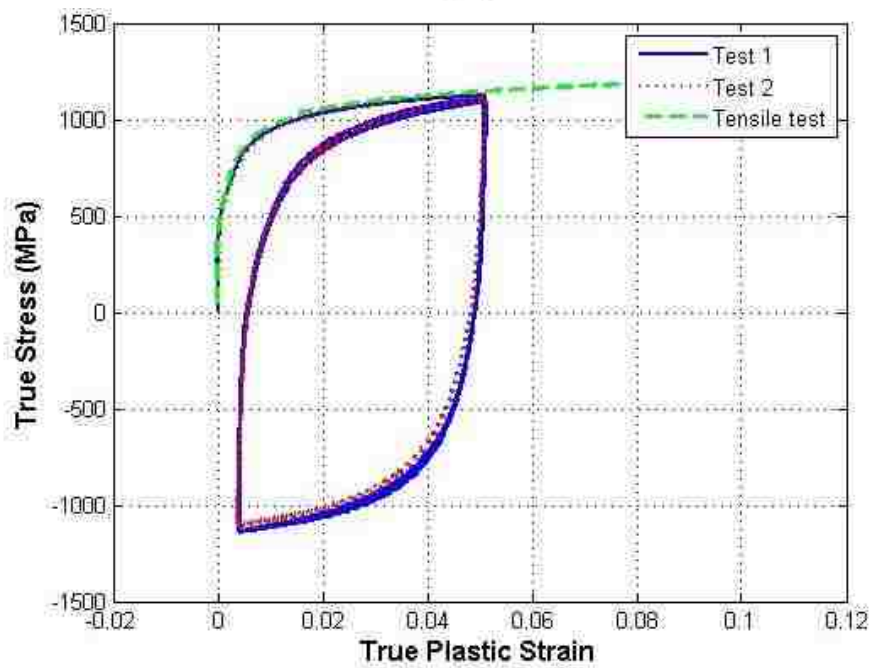


(b)

Figure 3.34: Cyclic tension - compression tests of TRIP780: a) Single cycle, b) Multiple cycles



(a)



(b)

Figure 3.35: Cyclic tension - compression tests of DP980: a) Single cycle, b) Multiple cycles

The graphs clearly show the repeatability of the tests results. Different regions of cyclic loading can be distinguished as discussed in Chapter 2. For DP980, the region of permanent softening is evident after the transient stage, but for TRIP780 the transient region extends well into the compressive zone. An average of the cyclic stress-strain data was used to determine the parameters required in the constitutive models which is explained in Chapter 4.

#### **3.4.4 Friction coefficient**

Specimens of each material type in form of square plates (760 mm by 760 mm) were used for friction tests at Arcelor Mittal Dofasco R&D centre in Hamilton, ON. Tests were conducted perpendicular to the sheet rolling direction (i.e. transverse) using a drawbead simulator.

All of the test specimens exhibited good surface quality (free of mechanical interference - scratches, gouges, heavy dirt, etc.). The drawbeads were cleaned with mineral oil, wiped dry with a lint free tissue, and lubricated with the wealth oil prior to testing. The depth of penetration for the male Roller and Fixed bead was reduced by around 50%. Five repeat tests were done for each material type to permit conditioning of the beads which were not used to characterize the frictional performance of the material. The next five tests were used as the “steady state” components of the test matrix. An average value of 0.097 and 0.102 were determined for TRIP780 and DP980, respectively.

# Numerical Analysis

---

## 4.1 Introduction

LS-DYNA explicit/implicit solver (version 971) was used in this study to simulate the forming and springback stages of a channel draw process. Three-dimensional shell models for each drawbead configuration of TRIP780 and DP980 were created using a python script in ABAQUS 6.9. Geometrical parameters for channels with and without drawbeads as well as the explicit simulation variables required to setup the forming step in ABAQUS, were defined as the input parameters in this script. Therefore, a variety of models can be created in a short time. Different constitutive models from LS-DYNA library - explained in chapter 2- were used in the simulations. Modeling parameters such as the number of integration points, element formulations, contact types and properties were also analyzed. For selective cases, simulations in LS-DYNA were compared with results from ABAQUS and a user-defined subroutine of the YU material model. Input parameters for the material models were determined using the experimental results from tensile tests and cyclic tension-compression tests. The optimization method used to identify the hardening parameters from tension-compression tests, is explained and compared with results reported by other studies for TRIP780 and DP980. Various results from both the forming and subsequent springback stages of the simulations were obtained and compared with the experimental values in order to identify the ability of each modeling technique to predict sidewall curl results of the channels.

## 4.2 Determination of Constitutive Material Parameters

For material models with isotropic hardening, plasticity curves of TRIP780 and DP980 (Fig.3.27) were used as the stress-strain curves. Other numerical parameters such as the yield strength, r-value and elastic modulus were assigned from Table 3.6 and the initial elastic modulus of steel is 207 GPa.

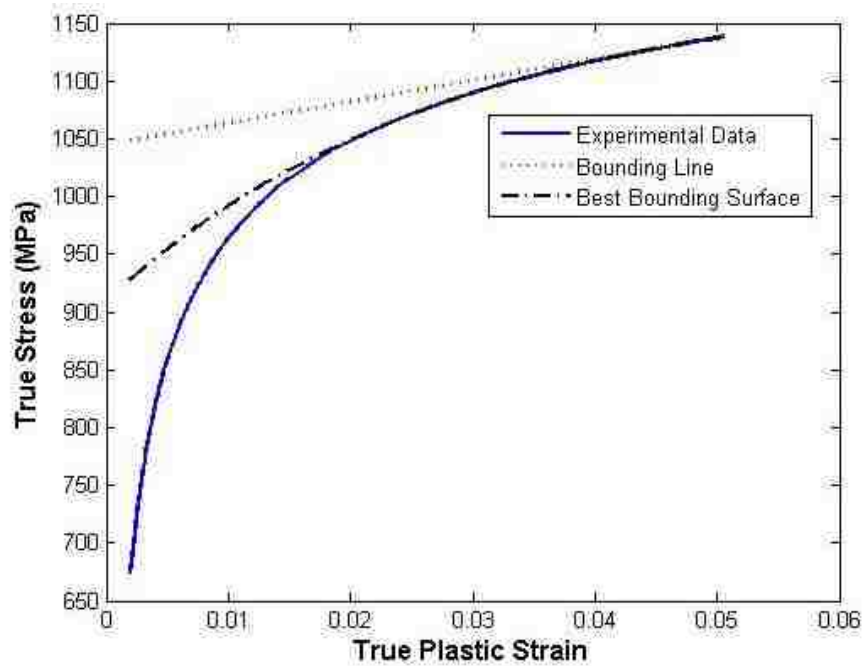
The systematic approach that was explained in Chapter 2, was used in order to determine the preliminary hardening parameters for the YU material model in LS-DYNA. A user-developed Matlab code helped to estimate these parameters from the tension-compression graphs of TRIP780 and DP980 as shown in Figs.4.1 and 4.2. The estimated parameters are summarized in Table 4.1.

Table 4.1: Intermediate YU model parameters from systematic analysis of tension compression test

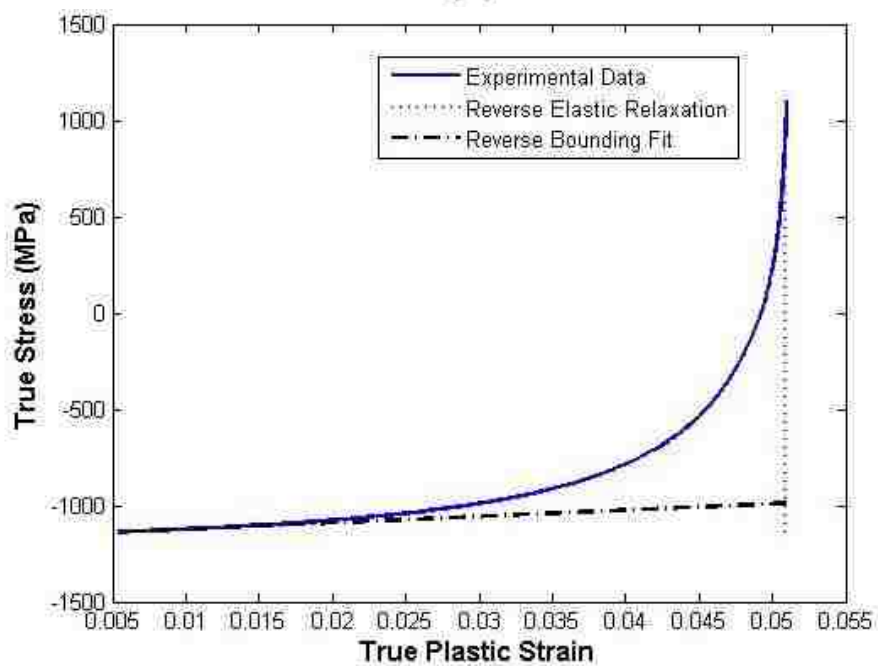
Material	B	$R_{sat} + b$	k	Re-yield stress (MPa)	$\sigma_{B0}^p$	b	$R_{sat}$
DP980	909.3	272.5	36	-203.4	155.1	92.3	180.2
TRIP780	429.8	862.7	8	-151.9	49.2	71.6	791.1

Tension-compression tests were then simulated in LS-DYNA by a single plane stress shell element model. This model consisted of a square element with a 1-mm side. The bottom side was fixed in the Y-direction and the left bottom corner fixed both in X- and Y directions, while the top side was extended and then compressed 0.1 mm in each stage in the Y-direction. Element formulation 2 (Belytschko-Tsay) with one integration point through the thickness was used to mesh the part. The schematic of this model is shown in Fig.4.3.





(a)



(b)

Figure 4.1: Fitting surfaces to experimental tension-compression data of DP980: a) forward bounding, b) reverse bounding

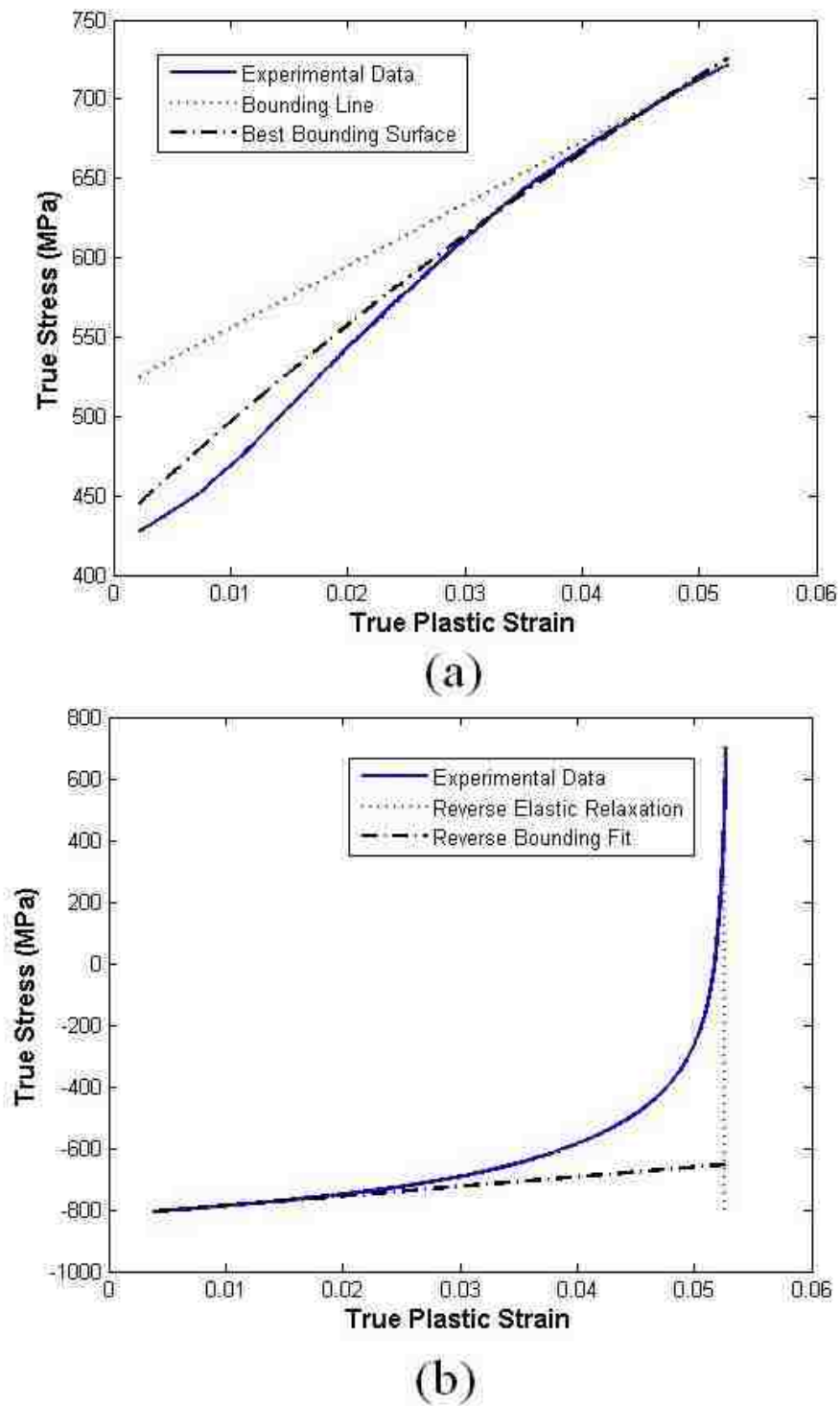


Figure 4.2: Fitting surfaces to experimental tension-compression data of TRIP780: a)forward bounding, b)reverse bounding

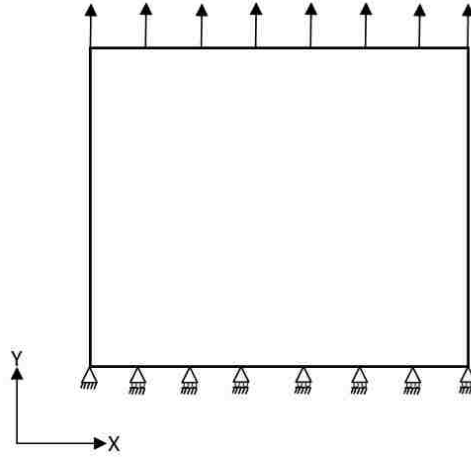
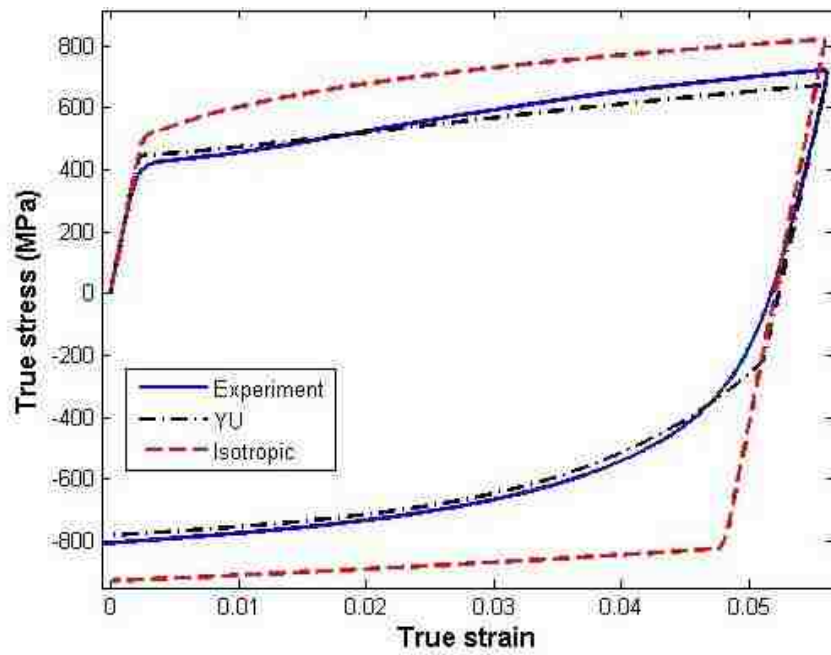


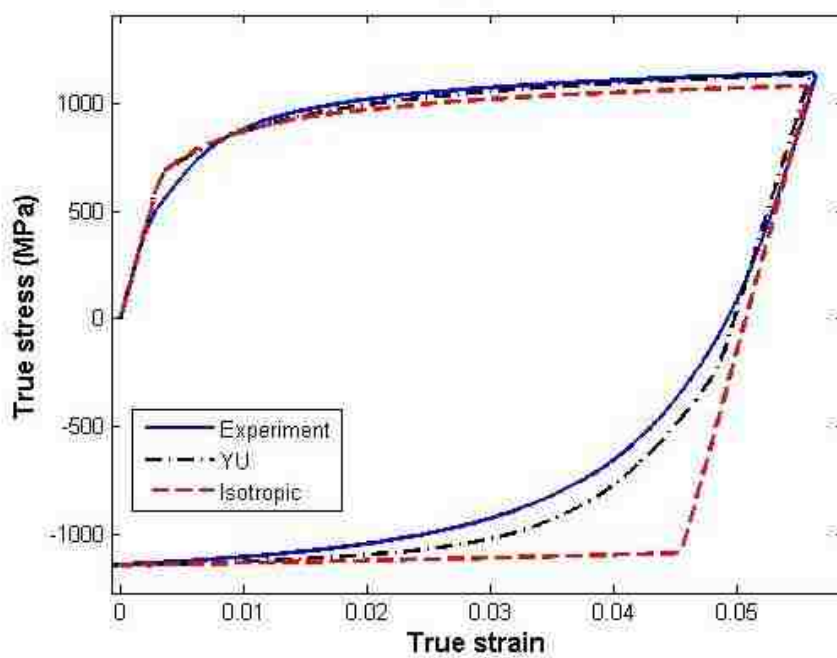
Figure 4.3: Schematic representation of the finite element model for tension compression test

The base simulations with the preliminary set of material parameters from Tables 3.6, 3.8 and 4.1 were assigned to material type 125 (YU model) for TRIP780 and DP980 as well as an isotropic hardening model (Mat 24). The predicted stress vs. strain outputs were then compared with the experimental test results in Fig.4.4. It was observed that the simulation results for an isotropic hardening model could not capture the response of the materials during cyclic loading particularly during the compression cycle. The YU simulations did not correlate well with the experimental values and therefore an optimization of the parameters was required to obtain a more accurate description of the cyclic behaviour.

In order to optimize the YU model parameters, the developed models in LS-DYNA with Mat125 were used in a Metamodel-based optimization project with LS-OPT 4.2 software. A sequential strategy with domain reduction (SRSM) method was used assuming normal distribution of the model variables. Linear order polynomial meta-model with D-Optimal selection of simulation points and default number of 11 iterations per case along with radial basis function for approximation of histories were incorporated to compare the cross-plot of Y-stress vs. Y-strain of the middle surface of the element with the experimental values of a single cycle tension-



(a)



(b)

Figure 4.4: Comparison of experimental tension and compression tests with isotropic hardening and YU models (Mat 125) for: a)TRIP780,b)DP980

compression test for TRIP780 and DP980. For comparison of the experimental and simulation curves a special function ‘MeanSqErr’ has been frequently used to compute the mean square error for the discrepancy between the output curve and the target curve:

$$\varepsilon = \frac{1}{P} \sum_{p=1}^P W_p \left[ \frac{f_p(\mathbf{x}) - G_p}{s_p} \right]^2 = \frac{1}{P} \sum_{p=1}^P W_p \left[ \frac{\varepsilon_p(\mathbf{x})}{s_p} \right]^2, \quad (4.1)$$

It is constructed so that  $G_p, p = 1 \dots P$  are the values on the target curve  $G$  and  $f_p(\mathbf{x})$  the corresponding components of the computed curve  $f$ .  $f_p(\mathbf{x})$  are represented internally by the response surface values.  $\mathbf{x}$  is the design vector. Recently, it has been argued that the mean square error function is suitable for ordinate-based curve matching. However a major difficulty is that steep parts of the target curve are difficult to incorporate in the matching. These kinds of problems present a strong case for incorporating the abscissa into the curve-matching metric. In our case, cyclic material models (hysteric curves) with more than one possible y-value for some of the x-values present more difficulty as they can not be quantified because of the non-uniqueness of the ordinate values of the computed curve with respect to the target curve. A logical approach to comparison of the two curves is to map one of the curves onto the other using Frechet distance. The analogy is that of a dog walking along one curve and the dog’s owner walking along the other connected by a leash. Both walk continuously and monotonically along the curve from the start point to the end point and can vary their velocities. The Frechet distance is the length of the shortest leash that is sufficient for transversing both curves in this manner. In version 4.2 of LS-OPT software, this method is implemented by mapping the points of one curve onto the second curve and computing the volume (area) between the two curves. When both curves are normalized, this typically yields a mismatch error with values much less than 1 for two reasonably matching curves [47].

Therefore, the curve mapping method was used as the weighted objective for

optimizing YU parameters in material type 125 for cyclic tension-compression tests of TRIP780 and DP980. Results of the optimization are shown in Fig. 4.5 and the identified parameters are summarized in Table 4.2. However, it should be taken into consideration that the prediction errors not only come from the variance error due to the intrinsic noise and unreliabilities in the measurement of the dependent variables but also from the systematic (bias) error due to model mis-specification. To be genuinely useful, a fitting procedure should provide the means to assess whether or not the model is appropriate and to test the goodness-of-fit against some statistical standard.

Table 4.2: Optimized YU model parameters for LS-DYNA with material type 125

Material	Y (MPa)	c	B (MPa)	$R_{sat}$ (MPa)	b (MPa)	k	h	$E_0$ (GPa)	$E_a$ (GPa)	$\xi$
DP980	670.7	156.3	909.3	161.7	121.2	36.5	0.05	207	157.8	57.5
TRIP780	452.2	205.5	489.8	587.6	178.7	10.05	0.03	207	132.7	46.1

The correlation matrices between Mat 125 parameters and the mapping error of the network response for each of the sheet metals are shown in Fig.4.6. A strong positive correlation was found between the response error and  $R_{sat}$ ,  $b$  and  $k$  parameters while a negative correlation was observed with  $h$ , for both material types. Mean square error was also compared against the curve mapping error. The correlation coefficient is a measure of how well the variation in the output is explained by the targets. Outliers can greatly affect the magnitudes of correlation coefficients. Of course, the larger the sample size, the smaller is the impact of several outliers.

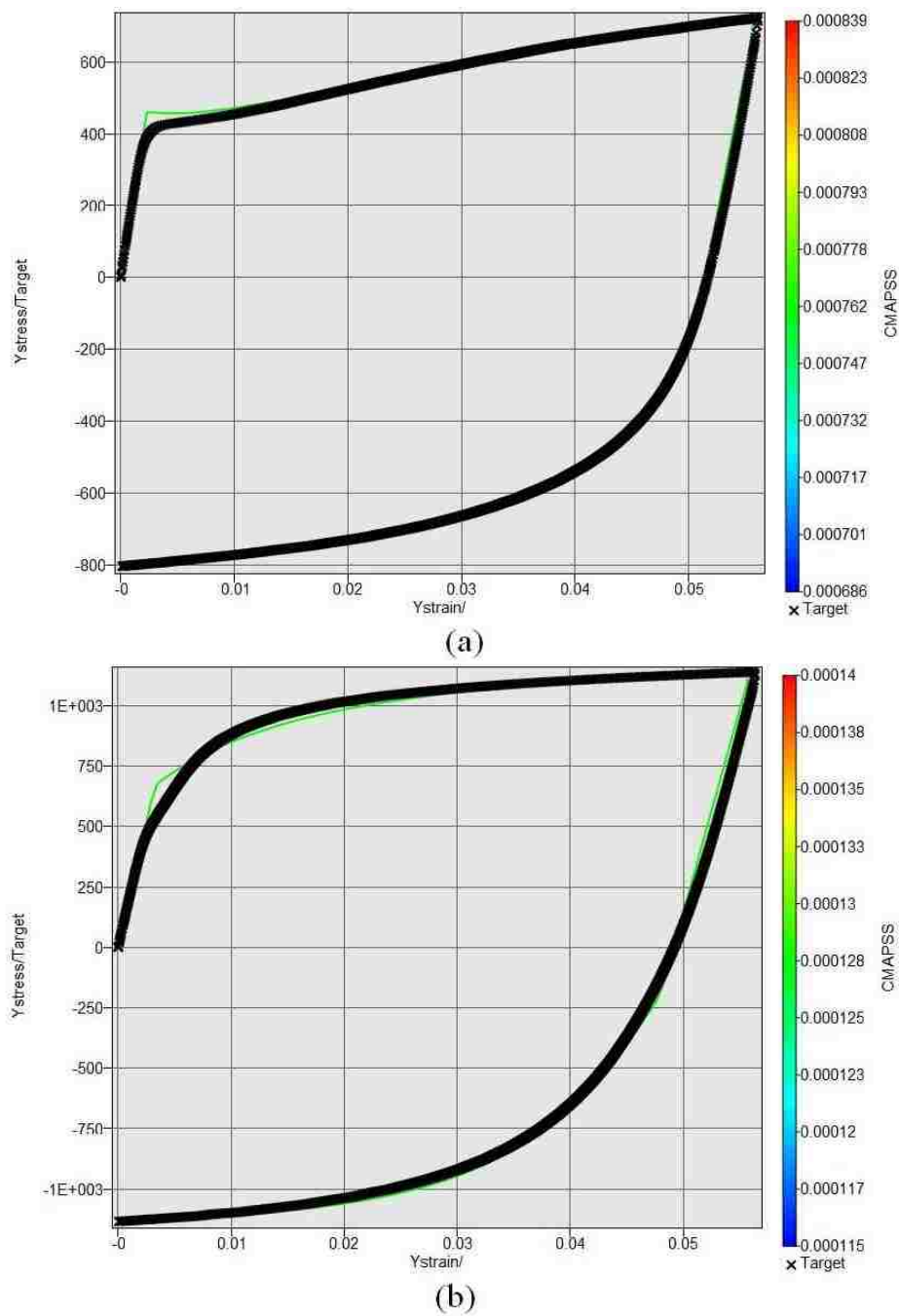


Figure 4.5: Optimized simulations with Material type 125 for tension compression tests of: a)TRIP780, b)DP980

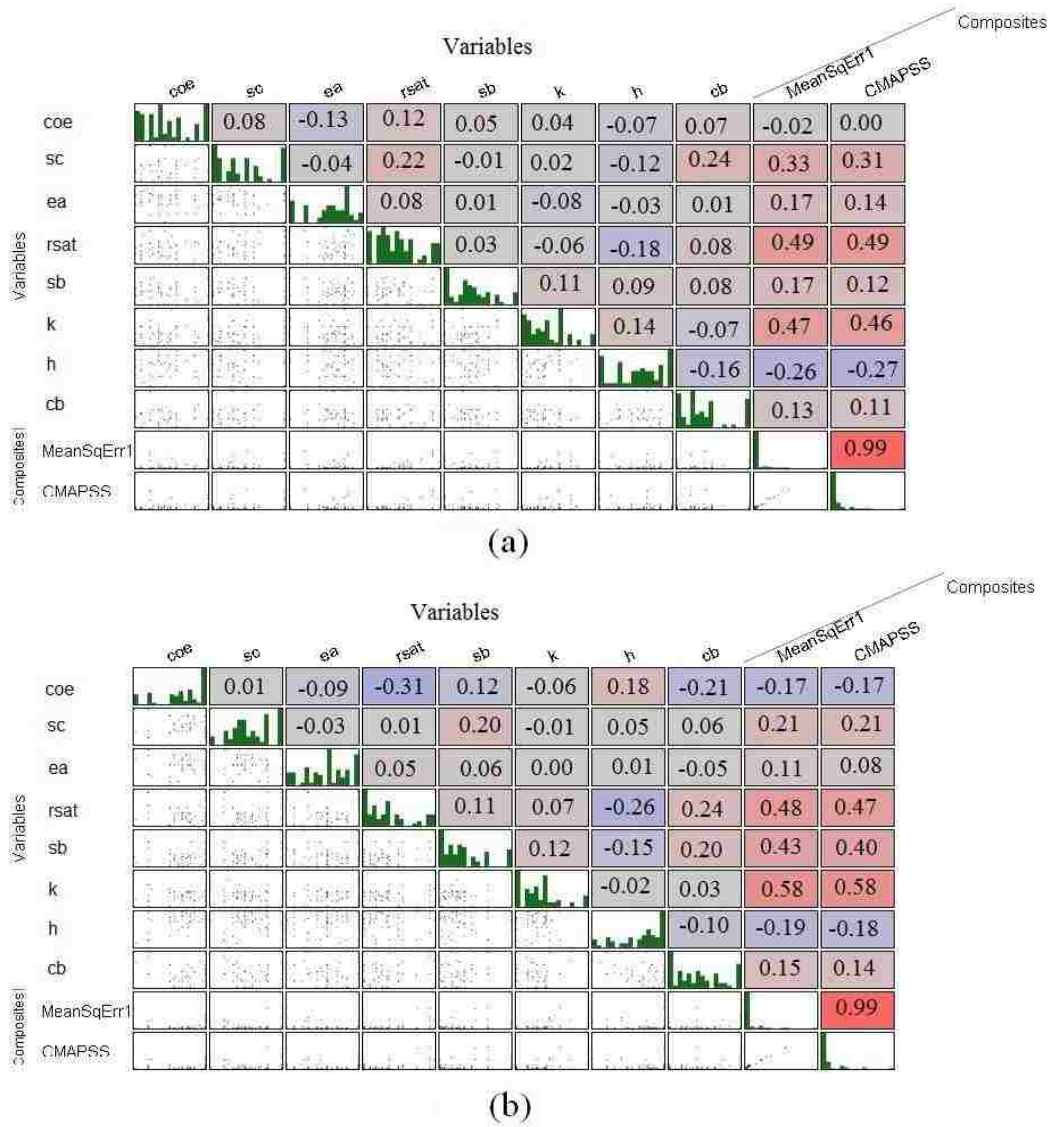


Figure 4.6: Correlation matrices between Mat125 parameters and curve mapping error response for: a)TRIP780, b)DP980

It should be mentioned that the optimized parameters found for DP980 sheets, were somewhat different from the values reported in another study. Shi et al. [46] identified parameters for both the original and modified YU models for a group of AHSS materials through similar tension-compression tests . The parameters for the original YU model for two grades of steel sheets similar to those used in our study are summarized in Table 4.3 . It was reported that the DP980 material exhibited



a pure kinematic hardening behaviour of the boundary surface where  $R_{sat} = 0$  and both the original and modified YU models yielded equivalent parameters. Also, it was observed that the impact of kinematic hardening components of the boundary surface become more important for AHSS than for conventional steels. However the reported yield strengths are not near the expected values and the unloading modulus parameters were not reported. For our current study, the optimized parameters found with LS-DYNA were used for subsequent analysis of the channel draw forming process, but for selective cases a comparison was performed in which parameters from Table 4.3 were used with ABAQUS solver.

Table 4.3: Original YU parameters reported in another study [46]

Material	Y (MPa)	c	B (MPa)	$R_{sat}$ (MPa)	b (MPa)	k	h
DP980	399.1	275.4	822.2	0.0	405.1	44.0	0.02
DP780	291.6	460.7	465.1	52.5	444.7	56.5	0.95

### 4.3 Finite element model of channel draw

A user-defined python script was developed to create FE models for various channel draw configurations mentioned in Tables 3.2 and 3.3. Using specific input parameters for die entry radius (DER), drawbead penetrations and other geometrical parameters from Table 3.1, the script can create a 3D finite element model of all the tooling and the sheet metal, define material models, assign section and coordinate system definitions, mesh the part with required mesh size and prepare a two-step explicit forming analysis with appropriate output requests. Considering the symmetry of the problem, only a quarter of the channel was modeled. The shell element type S4R was selected to mesh the blank and due to its large width, only a small portion of the blank was modeled with appropriate symmetry boundary conditions to ensure plane strain deformation. Another set of scripts were also

developed to create 2D and 3D solid models, but are not reported in this study. Previous studies have indicated that both solid and shell elements with sufficiently fine mesh would produce the same springback profile for the channel draw process [25].

In these FE models, all the tools, die, punch and binder were modeled as rigid bodies. The forming simulation was defined in two steps; first, the drawbeads and the die part were moved on to the panel up to a constant clearance and then drawing was simulated by movement of the punch while the die and binder remain fixed relative to the punch. Once the forming stage was completed, the part with its stress-strain state was transferred to an implicit springback analysis in which specific nodes of the part were constrained in order to eliminate the rigid body motion of the part and allow it to naturally springback to its final shape, just as when the part is removed from the tools.

The parts created by the script file in ABAQUS were then exported in IGES format to prepare the required surfaces for the models in LS-DYNA. An initial mesh size of 2.5 mm was used for tools and a mesh size of 3 mm for the blank, as shown in Fig.4.7. Mesh adaptivity was used for all the models up to 4 levels with 5 degrees of adaptive error tolerance relative to the surrounding elements for each element of the blank to be refined. The recommended one-pass with look-forward active parameters were also considered for the adaptive re-meshing.

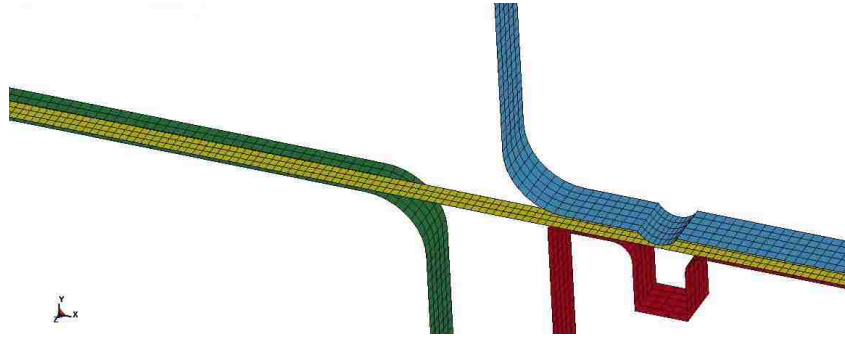


Figure 4.7: Finite element model of the channel draw forming in LS-DYNA

Shell elements were used to model the blank with element formulation 2 (Belytschko-Tsay) and 9 integration points through the thickness. Quadrilateral element type 2 was used due to its efficiency, although it requires one-point integration, does not pass the patch test and performs poorly on warped geometries. Therefore a comparison was also made when full integration elements were used. The problem with reduced integration and kinematic modes were resolved partially by hourglass control, which leads to satisfactory results in most situations. The shear correction factor was set equal to  $\frac{5}{6}$  which is valid for isotropic materials but not for sandwich and laminated shells. The shell formulations in LS-DYNA, with the exception of BCIZ triangular shells and DK fully integrated linear quadrilateral/triangular shell elements (formulations 3 and 18, respectively), are based on a first order shear deformation theory that yields constant transverse shear strains which violates the condition of zero traction on the top and bottom surfaces of the shell. The shear correction factor is an attempt to compensate for this error.

For treating the interaction between tools and the blank, three contact interfaces with algorithm type “FORMING\_ONE\_WAY\_SURFACE\_TO\_SURFACE” were defined in which the blank was the slave part set and tools were the master, using the standard formulation of the penalty method. Viscous damping coefficient was set as 20% of the critical in order to avoid undesirable oscillations in contact dur-

ing forming simulations and was applied perpendicular to the contacting surfaces. Suitable velocity curves in the Y-direction were defined for the forming steps with prescribed rigid body motions as well as a load curve for the binder force. One way contact types allow for compensation loads to be transferred between the slave nodes and the master segments. Tangential loads are also transmitted if relative sliding occurs when contact friction is active. The one-way term in one-way contact is used to indicate that only the user-specified slave nodes are checked for penetration of the master segments. One-way contacts may be appropriate when the master side is a rigid body, e.g., a punch or die in a metal stamping simulation. A situation where one-way contact may be appropriate for deformable bodies is where a relatively fine mesh (slave) encounters a relatively smooth, coarse mesh (master). Orientation is automatic with forming contacts. The rigid tooling surface can be constructed from disjoint element patches where contiguous nodal points are sometimes merged out, but not always. These patches are not assumed to be consistently oriented; consequently, during initialization, the reorientation of these disjoint element patches is performed. Forming contact tracks the nodal points of the blank as they move between the disjoint element patches of the tooling surface. Penalty forces are used to limit penetrations. Generally the `ONE_WAY_SURFACE_TO_SURFACE` option is recommended since the penetration of master nodes through the slave surface is considered in adaptive re-meshing. Without this feature, adaptive re-meshing may fail to adequately refine the mesh of the blank to capture sharp details in the master surface, and the master surface will protrude through the blank.

The friction between the blank and the tools was modeled as a constant coefficient of static friction identified from the friction test results. It should be mentioned that there are still major uncertainties in the description of friction-contact phenomena in simulation of sheet metal forming processes. Simulation calculations show that a small change in the friction-contact situation can have a significant effect

on the springback. However, the coefficient of friction is an experimental factor over which relatively minimal control is available in FE simulations. Researchers often use a coefficient value that best simulates the blank-tool interaction. For the channel draw process, a constant kiss gap of around 30% of the sheet thickness was maintained throughout the forming stage (Table 3.2), therefore the effect of friction was expected to have a minor effect on springback in this problem. Besides, punch velocity and binder pressure were kept constant during the forming and no dependency could be assumed between friction and relative velocity and pressure. Since only a limited area of the blank was in contact with the die radius and draw beads when present, and the contact area did not change significantly during the drawing stage, it was reasonable to assume a steady state kind of problem for the forming phase. The experimental punch force results shown in chapter 3, also confirm that the forming stage was nearly a quasi-static process. This suggests that a constant friction coefficient is valid for this problem. However, different values were used in the simulations to investigate the sensitivity of the predicted profiles to the coefficient of friction. This analysis showed that a higher value of the friction coefficient than the experimental results, best simulates the channel forming and springback stages when no drawbeads are used. For channels formed with drawbeads, friction coefficient had minimal effect on the results.

After the forming stage was completed, all the contact pairs defined between the blank and tools were removed allowing the channel to deform freely to its final sprungback shape.

As mentioned before, the models in ABAQUS were created using a user-defined script. Material models with isotropic hardening as well as the YU model accompanied by a user subroutine (UMAT) from a previous study [25] were compared for selected cases. For the user subroutine of the YU model, two sets of parameters

should be identified: *a*) the anisotropic coefficients, *b*) the YU hardening parameters.

YU model parameters were identified as described here. Anisotropic yield behaviour was modeled through the use of yield stress ratios,  $R_{ij}$  which are defined with respect to a reference yield stress,  $\sigma^0$ , such that if  $\sigma_{ij}$  is applied as the only non-zero stress, the corresponding yield stress is equal to  $R_{ij}\sigma^0$ . A local orientation must be used to define the direction of anisotropy. The Anisotropic parameters for the materials in the current study were determined from Hill's 1948 yield function as mentioned in Eq. 2.25 as F, G, H, L, M and N. Their definition from Eq.2.26 could be rewritten as:

$$\begin{aligned}
 F &= \frac{(\sigma^0)^2}{2} \left( \frac{1}{\sigma_{22}^2} + \frac{1}{\sigma_{33}^2} - \frac{1}{\sigma_{11}^2} \right) = \frac{1}{2} \left( \frac{1}{R_{22}^2} + \frac{1}{R_{33}^2} - \frac{1}{R_{11}^2} \right), \\
 G &= \frac{(\sigma^0)^2}{2} \left( \frac{1}{\sigma_{33}^2} + \frac{1}{\sigma_{11}^2} - \frac{1}{\sigma_{22}^2} \right) = \frac{1}{2} \left( \frac{1}{R_{33}^2} + \frac{1}{R_{11}^2} - \frac{1}{R_{22}^2} \right), \\
 H &= \frac{(\sigma^0)^2}{2} \left( \frac{1}{\sigma_{11}^2} + \frac{1}{\sigma_{22}^2} - \frac{1}{\sigma_{33}^2} \right) = \frac{1}{2} \left( \frac{1}{R_{11}^2} + \frac{1}{R_{22}^2} - \frac{1}{R_{33}^2} \right), \\
 L &= \frac{3}{2} \left( \frac{\tau^0}{\sigma_{23}} \right)^2 = \frac{3}{2R_{23}^2}, \\
 M &= \frac{3}{2} \left( \frac{\tau^0}{\sigma_{13}} \right)^2 = \frac{3}{2R_{13}^2}, \\
 N &= \frac{3}{2} \left( \frac{\tau^0}{\sigma_{12}} \right)^2 = \frac{3}{2R_{12}^2}.
 \end{aligned} \tag{4.2}$$

where each  $\sigma_{ij}$  is the measured yield stress when  $\sigma_{ij}$  is applied as the only non-zero stress component;  $\sigma^0$  is the user-defined reference yield stress specified for the metal plasticity definition; and  $\tau^0 = \frac{\sigma^0}{\sqrt{3}}$ . These anisotropic yield stress ratios are calculated as :

$$R_{11} = \frac{\sigma_{11}}{\sigma^0}, R_{22} = \frac{\sigma_{22}}{\sigma^0}, R_{33} = \frac{\sigma_{33}}{\sigma^0}, R_{12} = \frac{\sigma_{12}}{\tau^0}, R_{13} = \frac{\sigma_{13}}{\tau^0}, R_{23} = \frac{\sigma_{23}}{\tau^0}. \tag{4.3}$$

In a general 3D stress space, all six coefficients are used whereas in the case of sheet metal forming applications, as in the current U-channel forming process, the plane

stress assumption is generally adopted and Hill's 1948 yield criterion simplifies to:

$$f(\sigma_{ij}) = \sqrt{\frac{1}{2}[(G + H)\sigma_{11}^2 - 2H\sigma_{11}\sigma_{22} + (H + F)\sigma_{22}^2 + 2N\tau_{12}^2] - 1}, \quad (4.4)$$

In practice, it is more convenient to find the anisotropic material data given in terms of ratios of width strain to thickness strain (Lankford's r-values). Mathematical relationships are then necessary to convert the strain ratios to stress ratios that can be input into ABAQUS. Considering  $x$  and  $y$  to be respectively the "rolling" and "transverse" directions in the plane of the sheet and  $z$  as the thickness direction, the ratio of width-to-thickness strains is calculated from simple tension tests performed on standard specimens. For a tension test in the x-direction, Lankford's r-value is defined as:

$$r_x = \frac{d\varepsilon_{22}}{d\varepsilon_{33}} = \frac{H}{G}$$

Similarly, for a simple tension test performed in the y-direction in the plane of the sheet,

$$r_y = \frac{d\varepsilon_{11}}{d\varepsilon_{33}} = \frac{H}{F}$$

$r_x$ ,  $r_y$  are usually referred to as  $r_0$ ,  $r_{90}$ . For a more general case where the tension test is performed on a sample at an angle  $\alpha$  with respect to the rolling direction, Lankford's r-value is:

$$r_\alpha = \frac{d\varepsilon_{\alpha+\frac{\pi}{2}}}{d\varepsilon_{33}} = \frac{H + (2N - F - G - 4H)\sin^2\alpha\cos^2\alpha}{F\sin^2\alpha + G\cos^2\alpha}$$

For a commonly performed tension test in  $45^\circ$  with respect to the rolling direction, the r-value would be calculated as:

$$r_{45} = \frac{d\varepsilon_{11}}{d\varepsilon_{33}} = \frac{2N - (F + G)}{2(F + G)}$$

It is now possible to derive the equations for calculating anisotropy parameters for

orthotropic materials in plane stress deformations:

$$\begin{aligned}
 F &= \frac{r_0}{(1+r_0)r_{90}}, \\
 G &= \frac{1}{(1+r_0)}, \\
 H &= \frac{r_0}{(1+r_0)}, \\
 N &= \frac{1}{(1+r_0)}\left(\frac{1}{2} + r_{45}\right)\left(1 + \frac{r_0}{r_{90}}\right).
 \end{aligned} \tag{4.5}$$

Using Eq.4.5 and 4.2 and selecting direction 1 to be the reference, stress ratios will be calculated for plane stress case as in equations 4.6. Tables 4.4 and 4.5 summarize the values for Hill's anisotropic parameters and stress ratios of TRIP780 and DP980 respectively, using r-values from Table 3.6.

$$\begin{aligned}
 R_{11} &= 1.0, \\
 R_{22} &= \frac{1}{\sqrt{F+H}} = \sqrt{\frac{r_{90}(r_0+1)}{r_0(r_{90}+1)}}, \\
 R_{33} &= \frac{1}{\sqrt{F+G}} = \sqrt{\frac{r_{90}(r_0+1)}{(r_0+r_{90})}}, \\
 R_{12} &= \sqrt{\frac{3}{2N}}, \\
 R_{13} &= 1.0, \\
 R_{23} &= 1.0.
 \end{aligned} \tag{4.6}$$

Table 4.4: Coefficients for Hill's 1948 yield function

Material	F	G	H	N
TRIP780	0.44	0.61	0.39	1.57
DP980	0.87	0.51	0.49	1.79



Table 4.5: Stress anisotropic ratios for channel model in ABAQUS

Material	$R_{11}$	$R_{12}$	$R_{22}$	$R_{33}$
TRIP780	1.00	0.98	1.09	0.98
DP980	1.00	0.92	0.86	0.85

When using shell elements in ABAQUS (and LS-DYNA), which are based on first-order transverse shear flexible theory with constant through thickness shear strains, transverse shear, correction factors should be used to compensate for this assumption. For a homogeneous shell made of a linear, orthotropic elastic material, where the strong material direction aligns with the element's local 1-direction, the transverse shear stiffness should be:

$$K_{11}^{ts} = \frac{5}{6}G_{13}^Et, K_{22}^{ts} = \frac{5}{6}G_{23}^Et, \text{ and } K_{12}^{ts} = K_{21}^{ts} = 0.$$

where  $G_{13}^E$  and  $G_{23}^E$  are the material's shear modulus in the out-of-plane direction. The correction factor  $\frac{5}{6}$  results from matching the transverse shear energy to that for a three-dimensional structure in pure bending. For our study, the shear modulus was defined as:

$$G = \frac{E}{2(1 + \nu)}$$

and the values of the transverse shear stiffness were calculated as in Table 4.6.

Table 4.6: Transverse shear stiffness for channel model in ABAQUS, ( $\frac{N}{mm}$ )

Material	thickness	$K_{11}$	$K_{12}$	$K_{22}$
TRIP780	1.2	79000	0	79000
DP980	1.5	101000	0	101000

## 4.4 Results of channel forming simulations

Simulation results from FE models developed in LS-DYNA for each configuration of the channel draw are presented in this section. Comparison with related experimental results are also made.

### 4.4.1 Punch Force vs. Displacement curves

Punch force results were calculated from the contact forces of forming simulations of channels. For the cases with drawbeads, sufficient stretch was available to form the sidewalls. As shown in Figs.4.8 and 4.9, the punch force is overestimated by material models 24, 36 and 37 (with isotropic hardening [IH]) and underestimated by Mat 125 model for both TRIP780 and DP980 when drawbeads are used. Overestimation of IH models could be attributed to the failure of such hardening to capture the Bauschinger effect, and therefore the material response is over-predicted during cyclic loading.

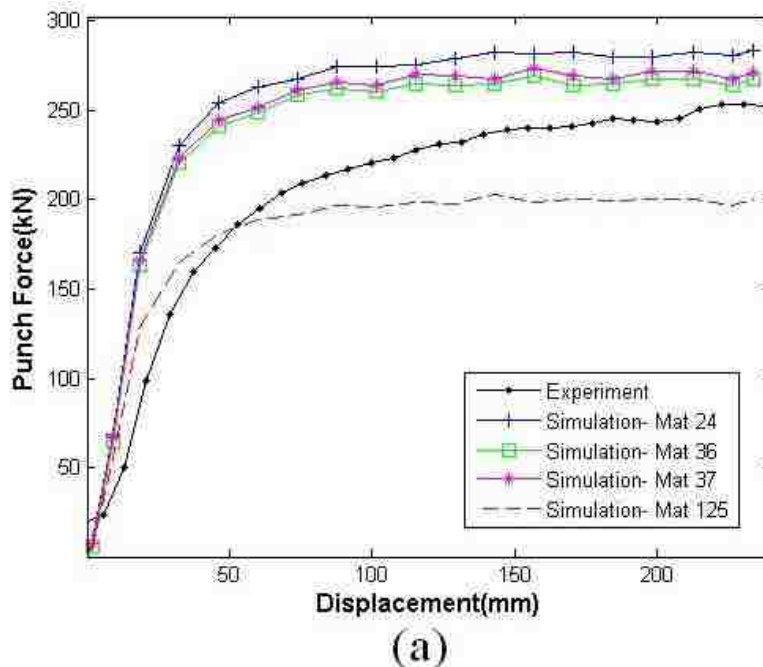
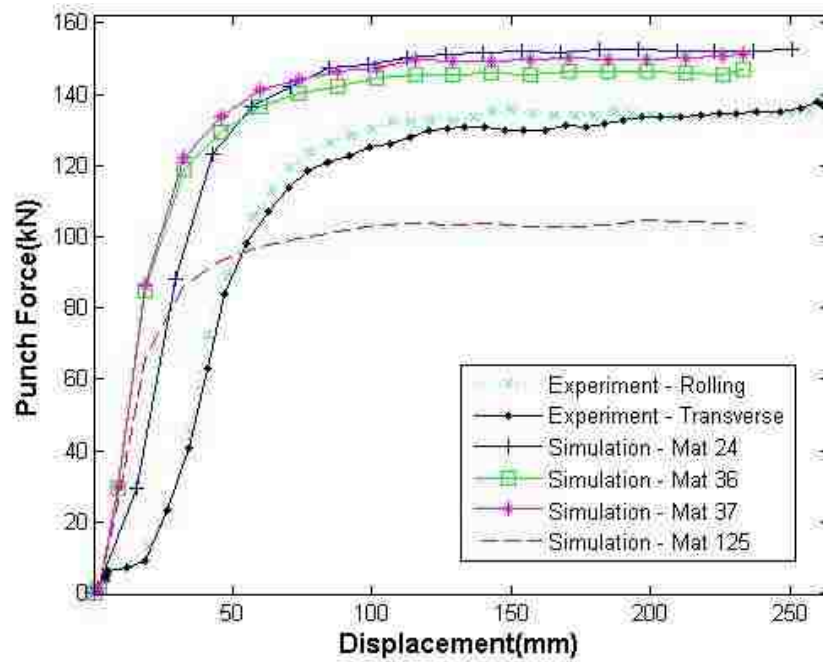
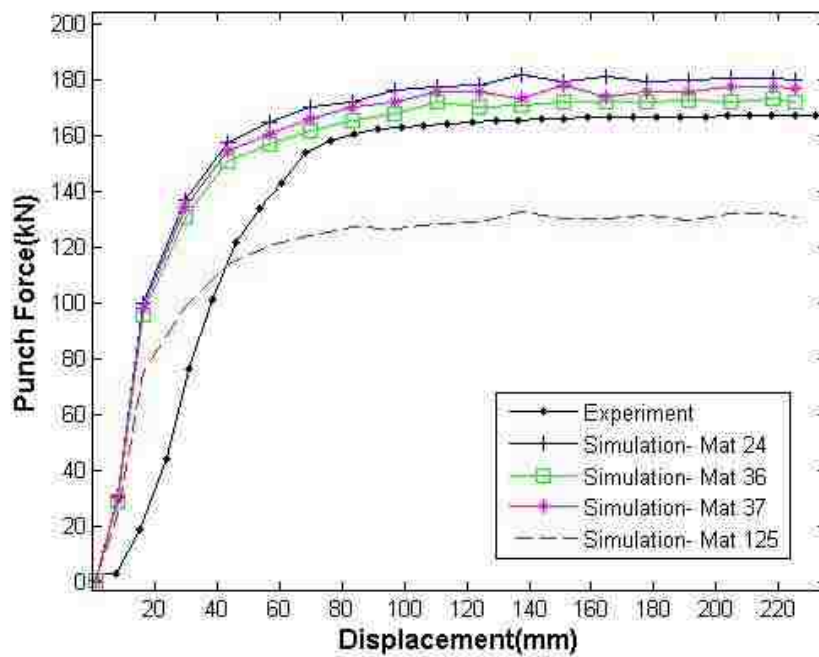


Figure 4.8: Comparison of predicted and experimental punch force results for DP980 with various material models



(a)



(b)

Figure 4.9: Comparison of predicted and experimental punch force results for TRIP780 with various material models and different drawbead penetrations: a)TPSB(20%), b)TPMB(25%)

However, more accurate results were expected for the YU model (Mat 125). Results of YU model in ABAQUS were compared against LS-DYNA results in Fig.4.10 which demonstrate better conformity of the converged punch force. Data set from ABAQUS was smoothed using curve fitting tool of Matlab. The smoothing was performed by using a piecewise polynomial computed from parameter  $p$  which was set to 0.8 and the resulting  $R^2$  of the fit was 0.997.

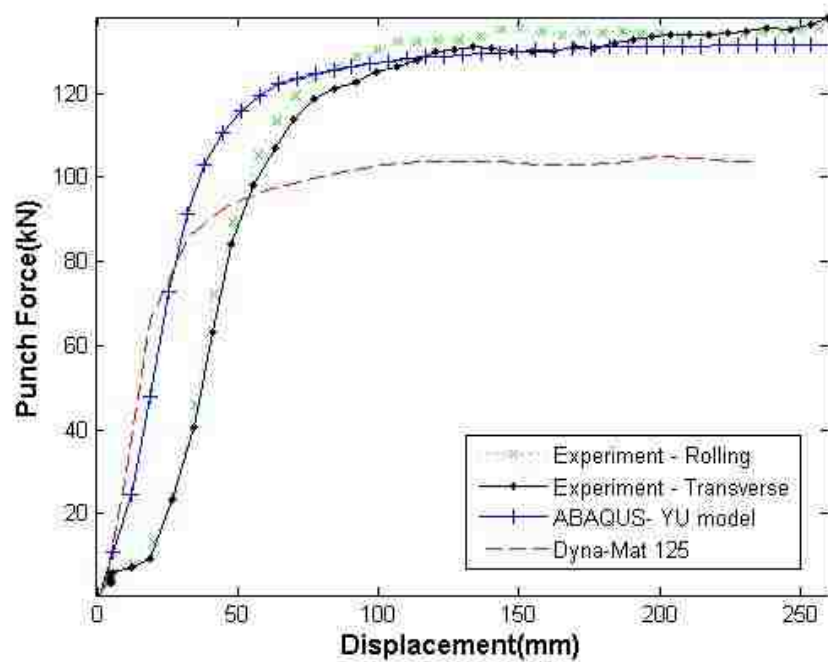


Figure 4.10: Comparison of experimental and predicted punch force results for TRIP780 with shallow beads using the YU model in ABAQUS and LS-DYNA

In order to identify the problem with simulations of Mat 125, energy balance of the simulations were checked and compared with those from other material models. As shown in Fig.4.11, energy levels of the simulations with Mat 125 demonstrate a mismatch between the total energy and the external work delivered to the system. For every correct simulation in LS-DYNA the energy levels should balance according to Eq.4.7:

$$\underbrace{E_{kin} + E_{int} + E_{si} + E_{rw} + E_{damp} + E_{hg}}_{\text{Total Energy: } E_{total}} = E_{kin}^0 + E_{int}^0 + W_{ext} \quad (4.7)$$

where suffixes on the left hand side represent Kinetic, Internal, Sliding interface (including Friction), rigid wall, damping and hourglass energies which should balance with the sum of initial values plus the external work on the right hand side. No rigid wall, damping and hourglass energies were present in the aforementioned simulations. The energy ratio is thus defined as:

$$e_{ratio} = \frac{E_{total}}{E_{total}^0 + W_{ext}}$$

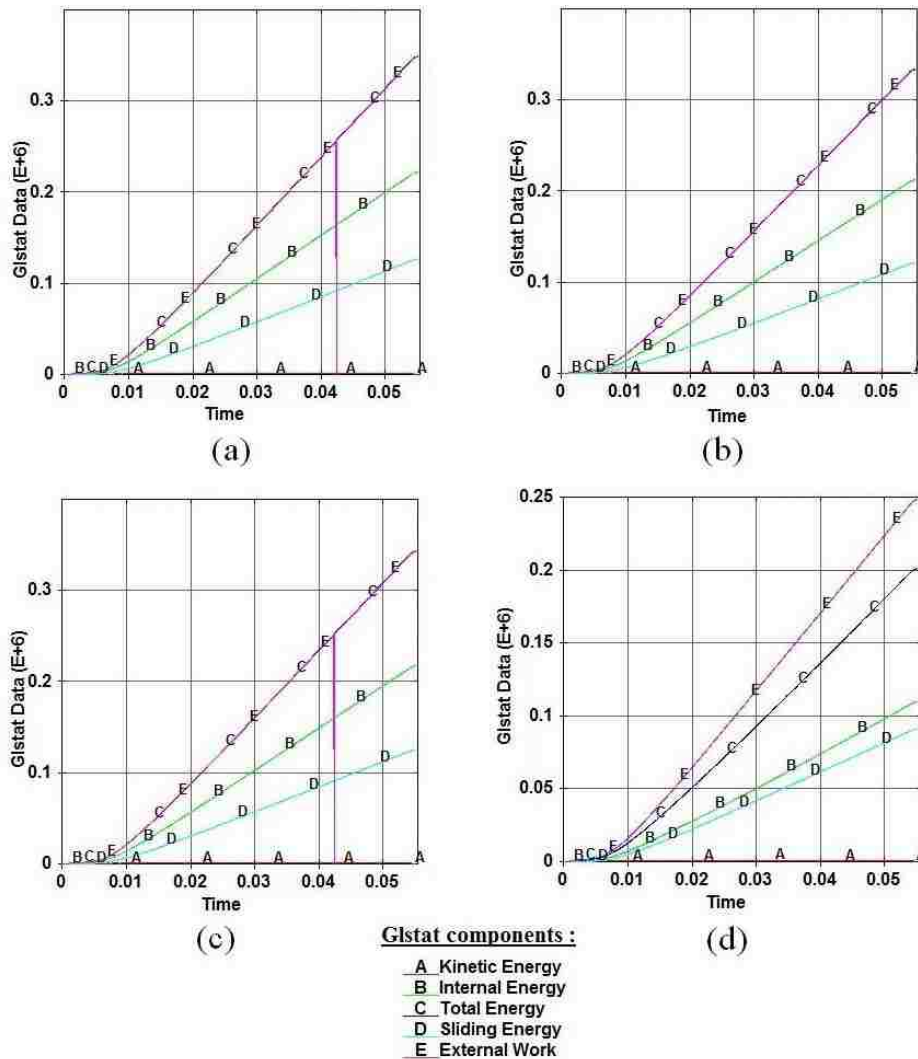


Figure 4.11: Energy balance for TPSB case with various material models: a)Mat24, b)Mat36, c)Mat37, d)Mat125

As can be seen in Fig.4.12, energy ratio for simulation with material type 125 fell well below unit and leveled off near 0.8 which confirmed the mismatch between total energy and the external work. In other words, part of the external work transferred to the system was not converted to increase in internal energy nor dissipated by the sliding. Such a situation is referred to as ‘artificial absorption’ of the energy. It could result from many sources, however in this case the only difference between multiple simulations was the material model. The energy balance equation was validated for other material types with the same mesh, contact definition and other model

parameters, as explained before.

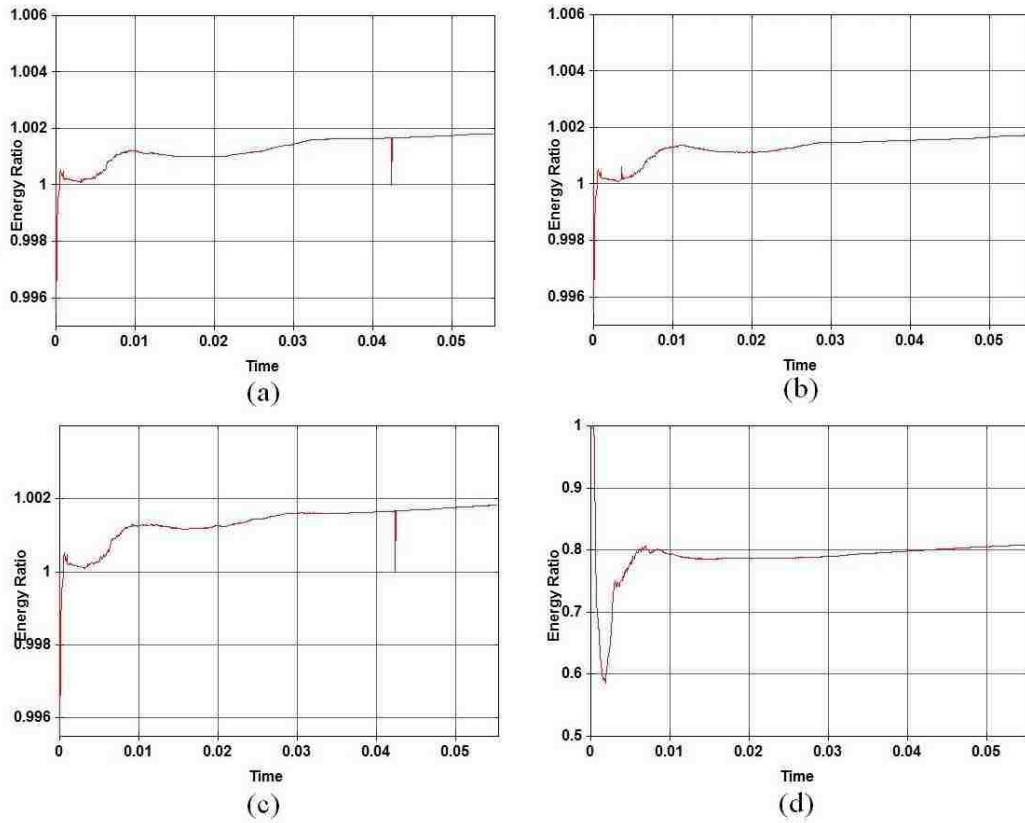


Figure 4.12: Energy ratio for TPSB case with various material models: a)Mat24, b)Mat36, c)Mat37, d)Mat125

Fig.4.13 shows the energy balance for YU model implemented in ABAQUS for the same TPSB configuration. It can be seen that the energy levels are comparable to the levels obtain in correct simulations by material models 24, 36 and 37 in LS-DYNA.

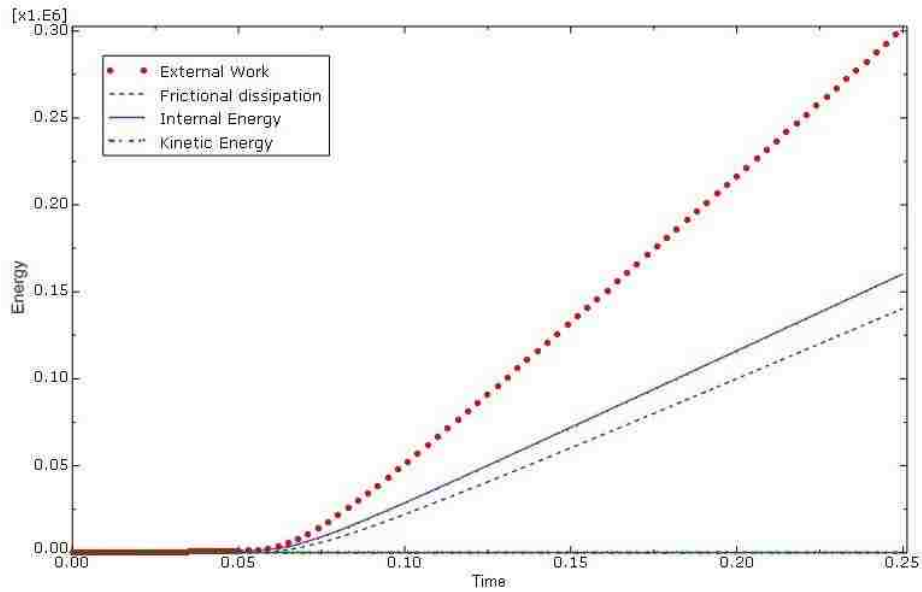


Figure 4.13: Energy balance for TPSB case in ABAQUS - YU model

Also results for energy balance and ratio for DPSB case were checked with various material types, shown in Figs.4.14 and 4.15 which confirm that the problem with Mat 125 is not related to numerical parameters. To further investigate this problem, simulations for DPSB and Mat125 were altered by changing element formulation from 2 to 16 (Fully integrated shell elements), increasing the number of integration points from 9 to 19, 29 and 49, eliminating mass scaling and mesh adaptivity while refining meshes of blank and tools to an approximate size of 0.5, using other contact types ‘FORMING\_SURFACE\_TO\_SURFACE’, ‘SURFACE\_TO\_SURFACE’ and several values of friction coefficient (0.0, 0.07, 0.125, 0.15, 0.2, 0.25). Simulation results for the both shell and solid elements of the single element model were also checked. However the energy balance problem persisted for all of these simulation with material type 125. This problem was reported to LSTC representative and was confirmed to be an issue that should be rectified. This problem leads to erroneous stress-strain results in the final stage of the forming which would be transferred to the implicit scheme for springback calculation. It is evident that the absorbed internal plastic energy is not at the same level as predicted by other material types.



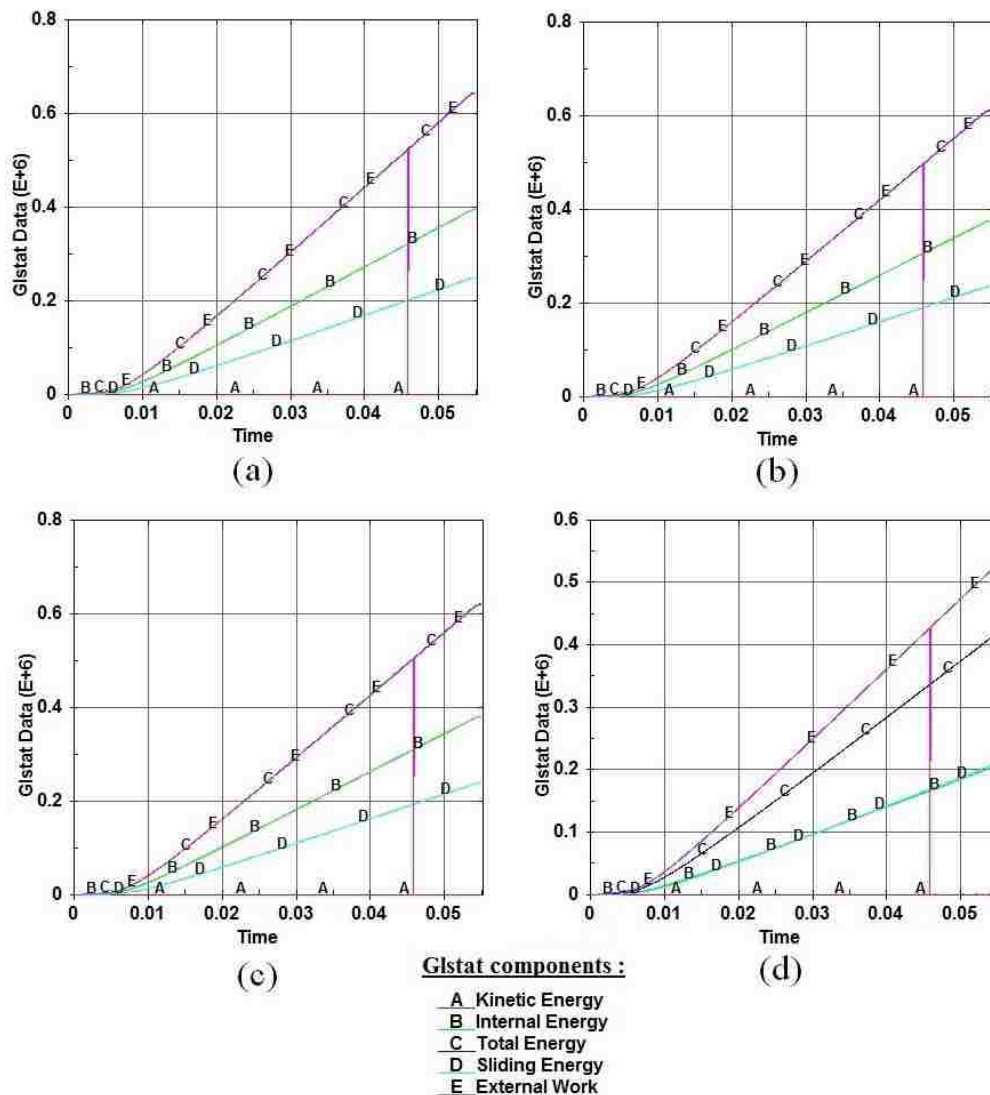


Figure 4.14: Energy balance for DPSB case with various material models: a)Mat24, b)Mat36, c)Mat37, d)Mat125

For the cases without drawbeads as shown in Fig.4.16, punch forces were under-predicted by Mat125 compared to the other material models which in turn failed to capture correct results either in LS-DYNA. This deviation from the experimental results was observed for all material models and for both DP980 and TRIP780 channels with the predefined contact parameters. The beginning portion of the curves conformed with the experimental data as the impact of the punch formed

---

the blank. After this initial step, the normal force that was exerted on the blank by the die was limited to a small contact area of the die radius region. With the default values of static coefficient of friction, the stretching force was not sufficient to maintain the required tension in the blank during the forming stage. When the movement of the blank was observed during the forming simulation, it became evident that the blank was under-constrained along its length. In this case, it was possible to calibrate the friction coefficient of the contact algorithms so that the predicted punch force correlated with the experimental results. A study with various friction coefficients was performed with material model 24, as shown in Fig.4.17. This suggests that friction forces at the contact interface between the blank and die radius would be more prominent in cases where no draw beads were present. A friction coefficient equal to 0.19 best conformed with the experimental data.

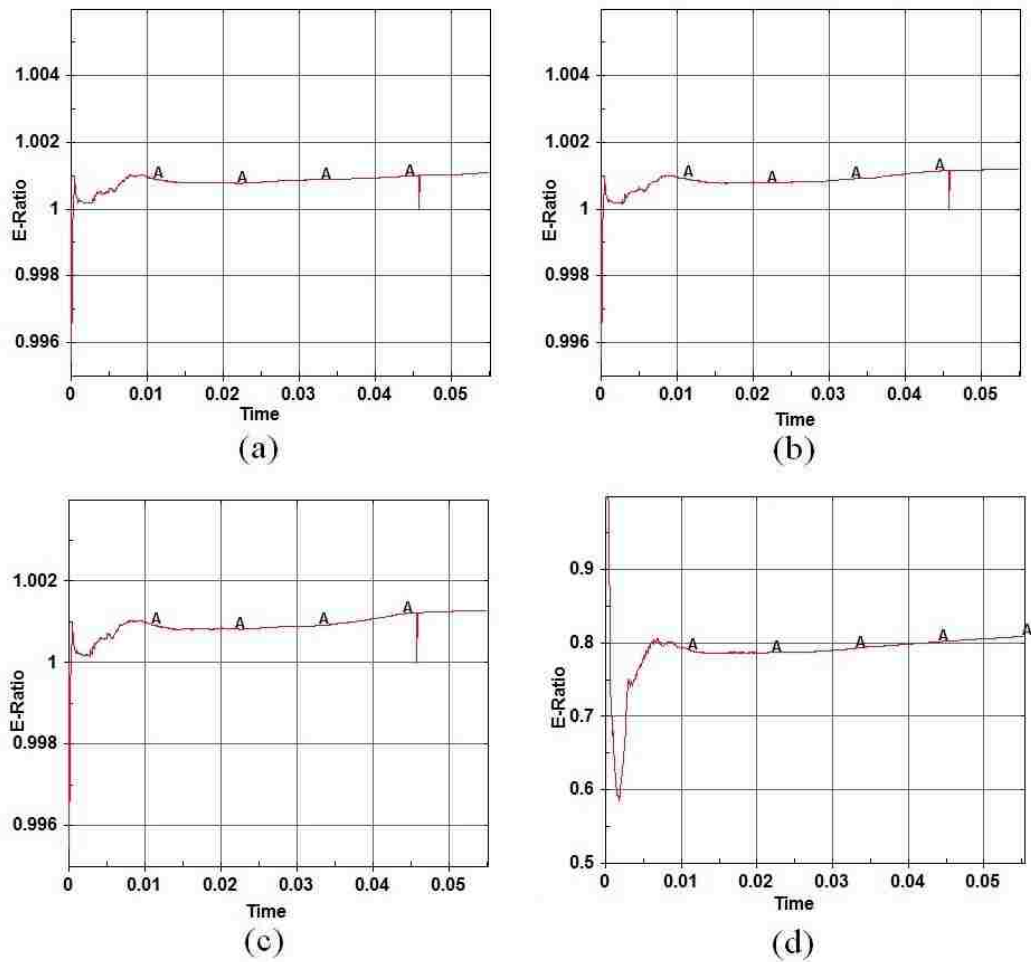


Figure 4.15: Energy ratio for DPSB case with various material models: a)Mat24, b)Mat36, c)Mat37, d)Mat125

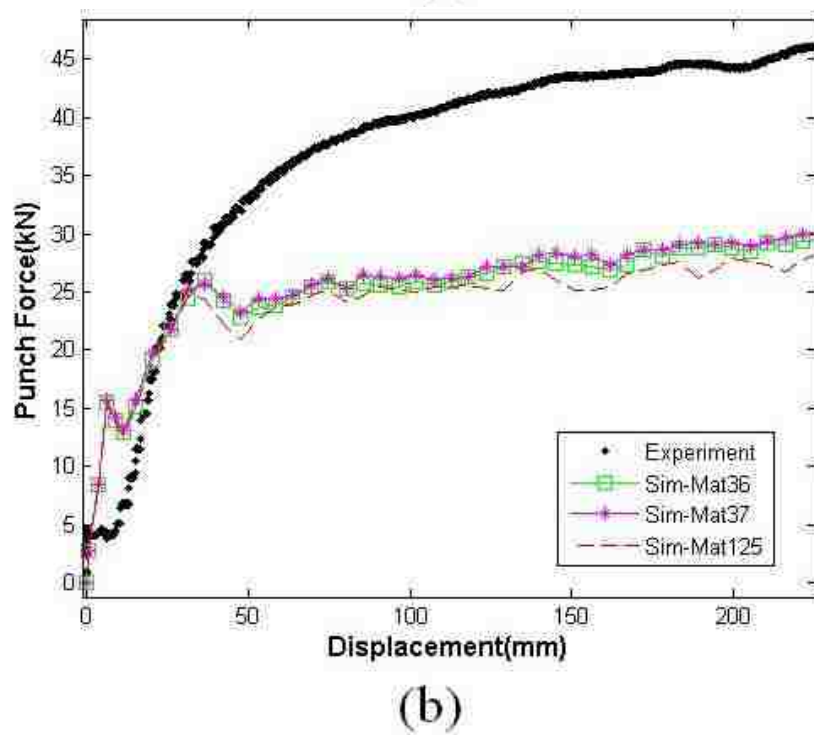
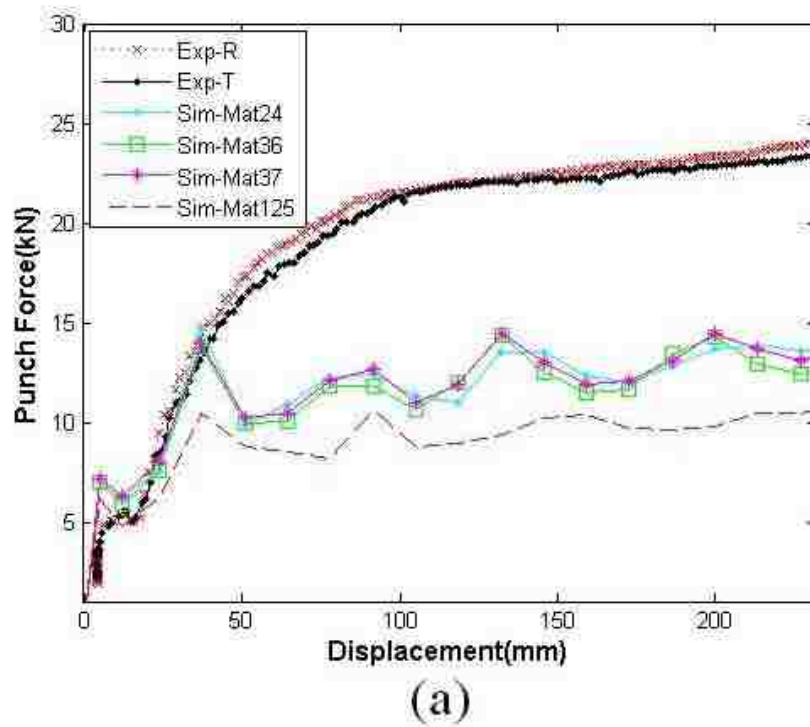
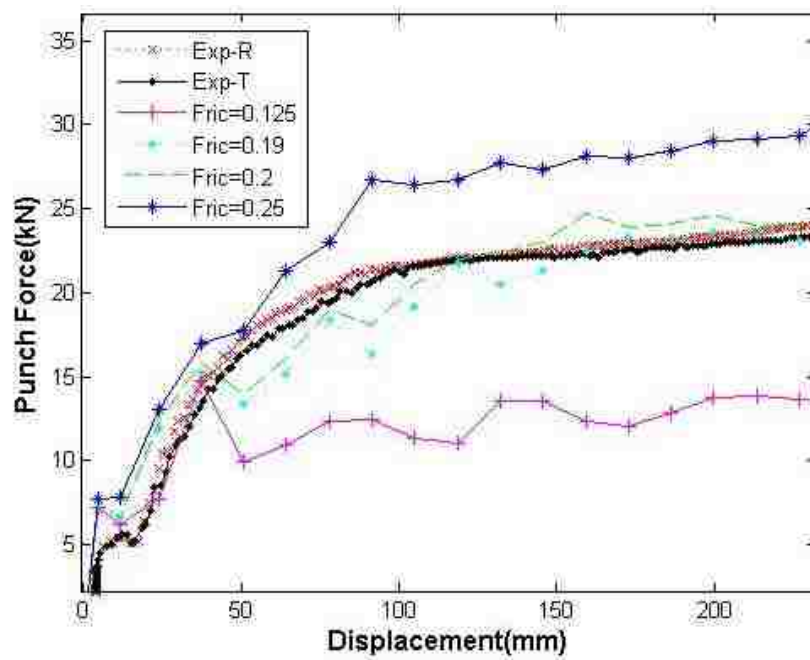
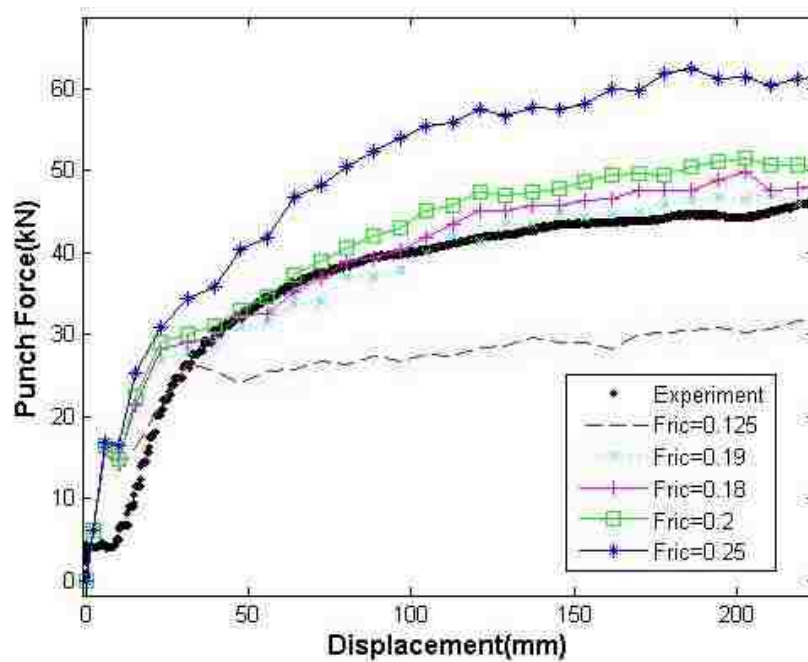


Figure 4.16: Comparison of predicted and experimental punch forces for channels without draw beads and with DER=12mm: a) TRIP780, b) DP980



(a)



(b)

Figure 4.17: Comparison of predicted and experimental punch forces for cases without beads, DER=12mm and Mat 24 for various coefficients of friction: a) TRIP780, b) DP980

#### 4.4.2 Channel sidewall profiles

The final geometry of the parts after springback is an important measure for comparison between different models. Sidewall opening angle, flange tip angle and curl radius as defined in Fig.3.18 provide appropriate measures for comparing U-channels parts. However it should be noted that for such open channel geometries a fairly small angular difference coupled with different sidewall curvatures may bring about a relatively large change in the overall dimensions of the channel. Moreover they do not provide a single criteria for comparison. For this sake, an area integration method, used in previous studies, was also further developed as a measure to estimate the error between simulated and experimental sidewall curl results. For more elaborate parts or surfaces a cross correlation method might be more appropriate.

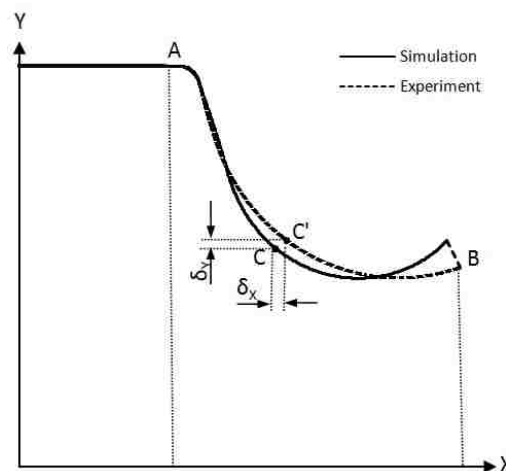


Figure 4.18: Schematic illustration of sidewall comparison between simulated and experimental curves

The error between simulated and experimental channel profiles was quantified by computing the area under the curves of both profiles drawn on a 2D diagram, as

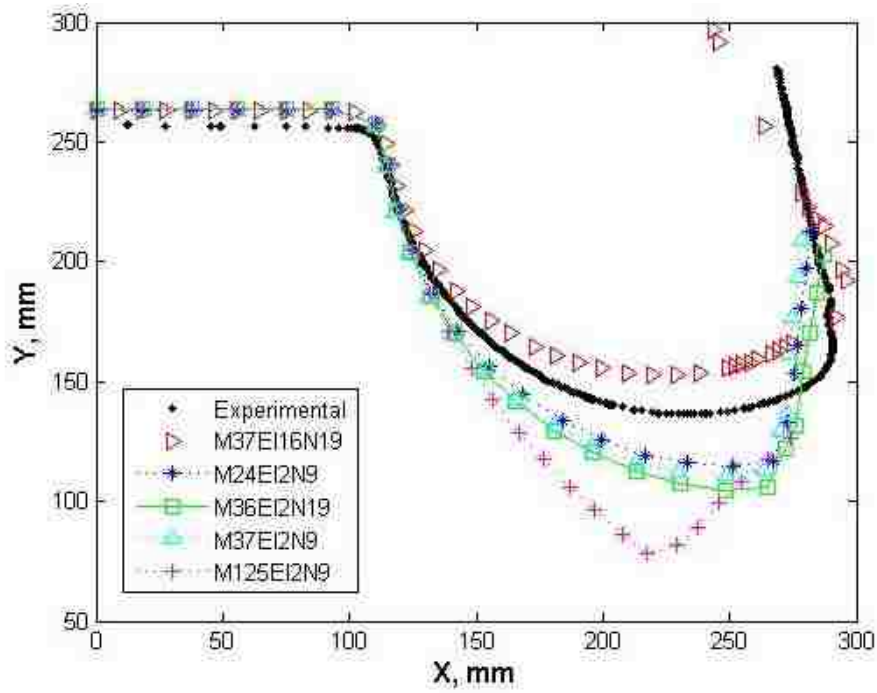
shown in Fig. 4.18. As the experimental and simulated profiles might not necessarily have one-to-one analogy, an interpolated profile was constructed on each of the curves on their common range for more accurate comparison using a Matlab code. The difference between each point  $C$  on experimental curve can be obtained with respect to its counterpart point  $C'$  on the simulated curve. Simulated curves were constructed from nodal coordinates read from the final geometry of the channels after springback. Therefore, the error at each point was calculated as  $\delta_C$  from difference in both X- and Y- directions:

$$\delta_C = \sqrt{(X_C - X_{C'})^2 + (Y_C - Y_{C'})^2},$$

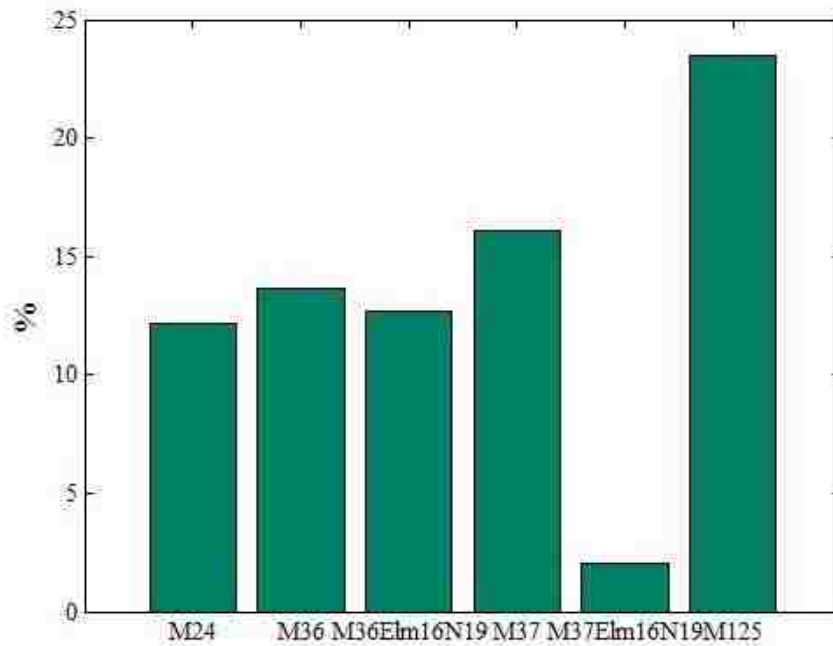
The sum of errors over the common portion of the sidewall curves was calculated by line integral method. By dividing the sum of errors by the area under the experimental curve from point  $A$  to  $B$ , the normalized error between corresponding experimental and simulated sidewall profiles can be calculated:

$$\text{Sidewall error(\%)} = \frac{\text{Area between curves, integral of } \delta_C}{\text{Area under experimental curve from A to B}} \quad (4.8)$$

Results of channel sidewall comparison for various configurations are shown in Figs.4.19 and 4.20 for channels with shallow beads and in Figs.4.21 and 4.22 for cases without drawbeads and a die entry radius of 12 mm. It can be seen that although material model 125 (YU) was expected to produce more accurate results, it fails to predict sidewall curl correctly, most probably from an incorrect integration scheme as the results on energy balances were explained before. However for material model 37, with increasing through-thickness integration points as well as changing element formulation to type 16 which is a fully integrated element type, the error in predicting sidewall curvatures was substantially reduced for shallow bead cases. Sidewall profiles of cases without drawbeads are less accurate in visual terms, mainly due to insufficient stretch force on the blank as explained previously.



(a)



(b)

Figure 4.19: Comparison of simulated and experimental sidewall profiles for TRIP780 channels with shallow beads: a) different material models, b) sidewall error (Eq. 4.8)



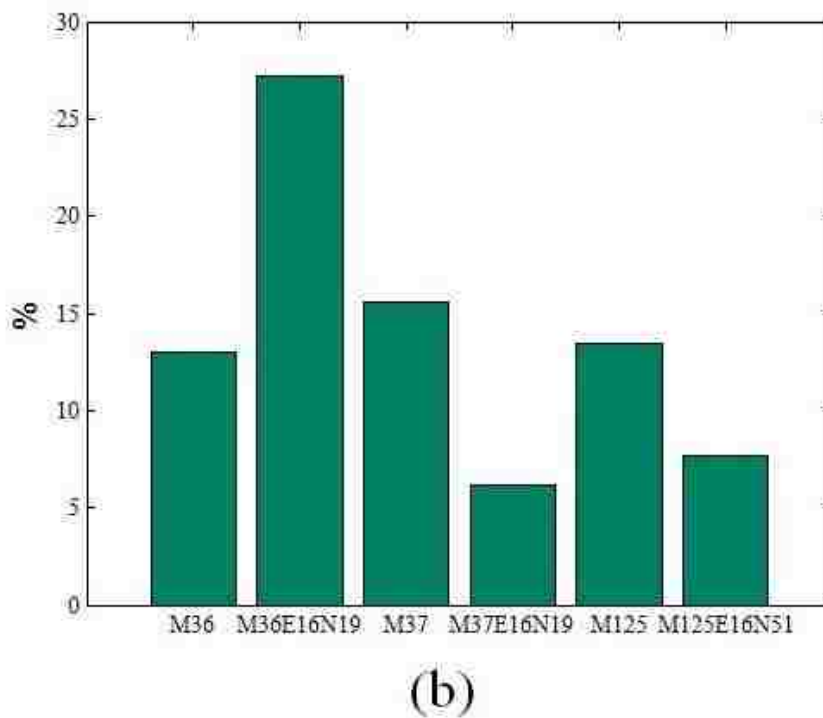
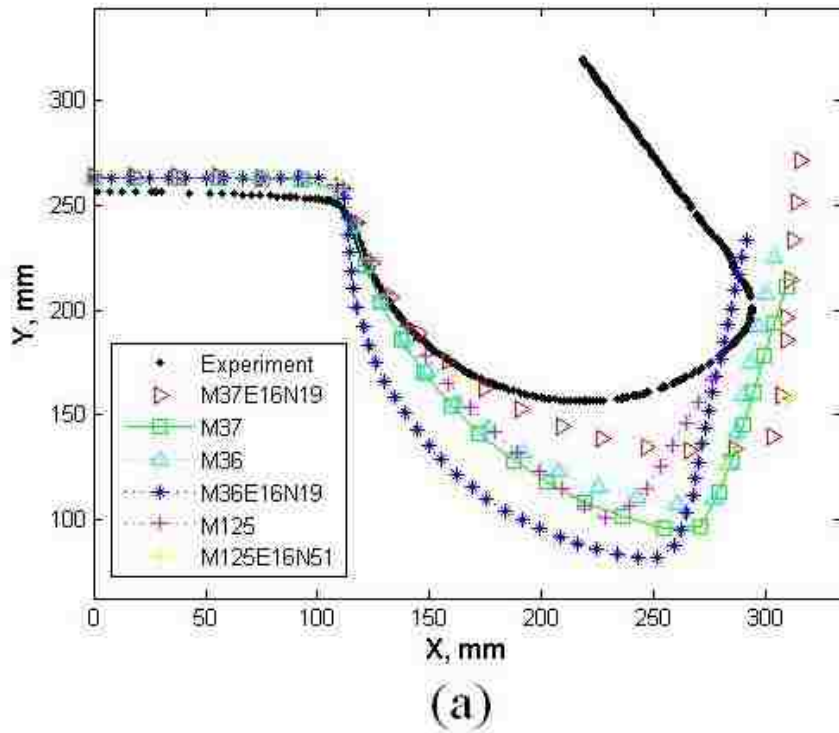
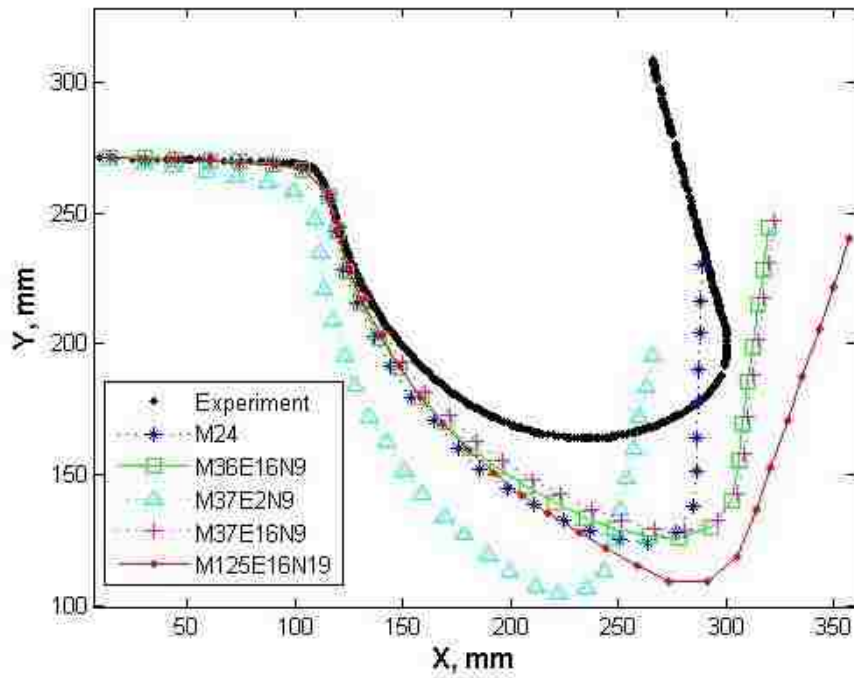
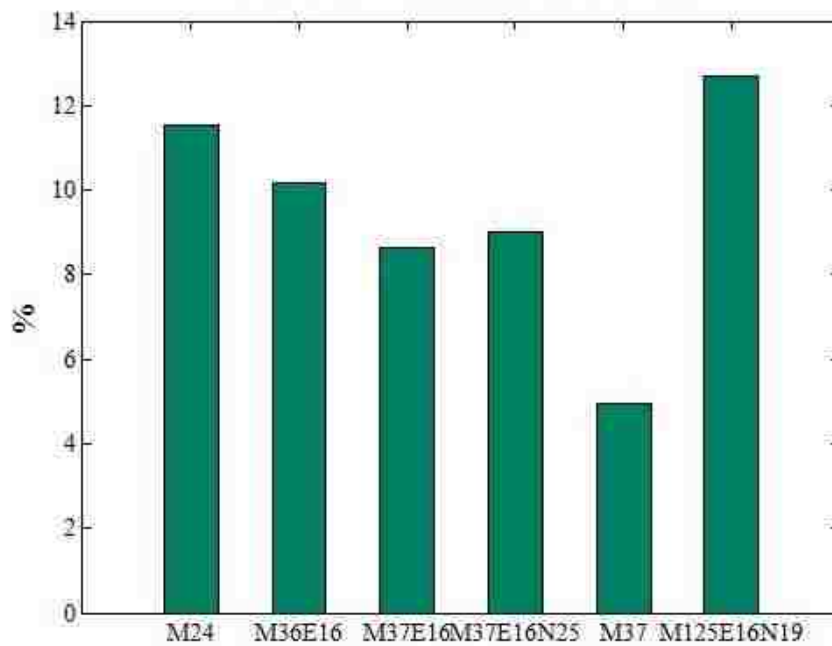


Figure 4.20: Comparison of simulated and experimental sidewall profiles for DP980 channels with shallow beads: a) different material models, b) sidewall error (Eq. 4.8)



(a)



(b)

Figure 4.21: Comparison of simulated and experimental sidewall profiles for TRIP780 channels without beads and DER=12mm: a) different material models, b) sidewall error(Eq.4.8)

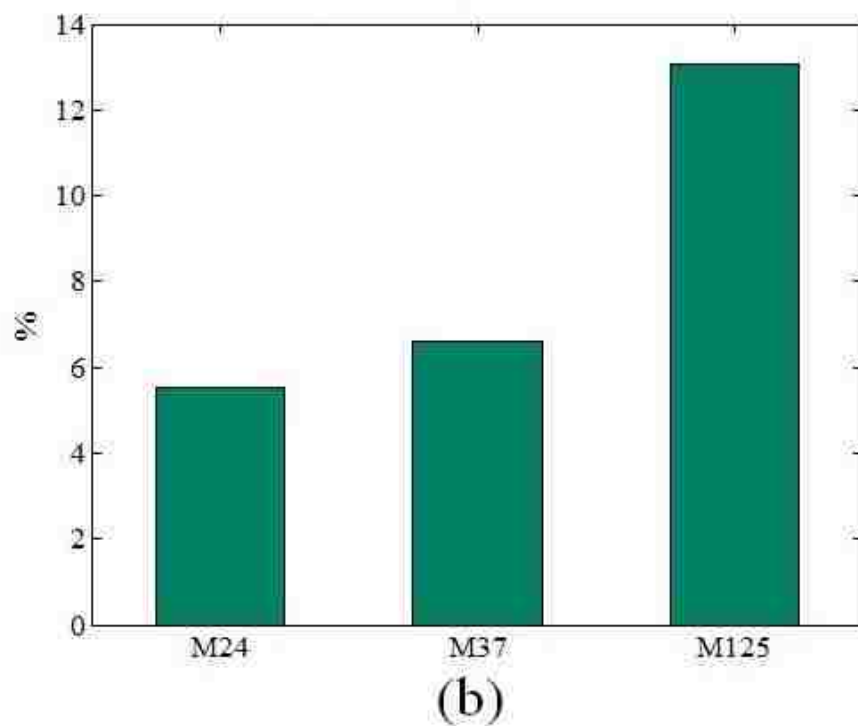
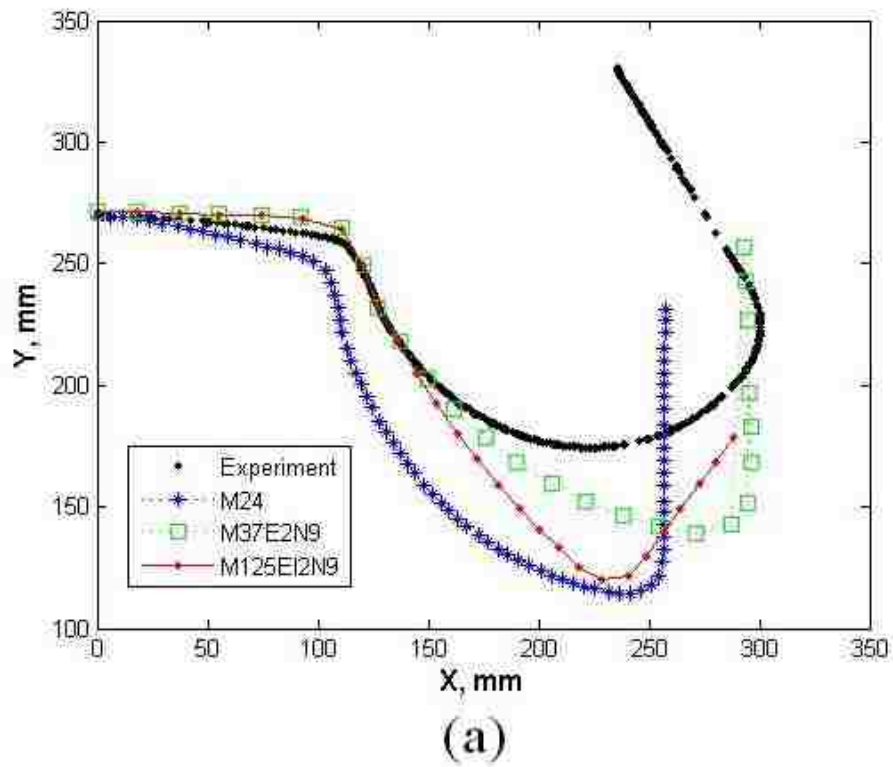


Figure 4.22: Comparison of simulated and experimental sidewall profiles for DP980 channels without beads and DER=12mm: a) different material models, b) sidewall error (Eq.4.8)

The comparison between simulation results and experimental profiles, can also be considered by estimating the wall opening and flange tip angles as well as a best fitted arc to the sidewall, similar to the study of experimental data in Chapter 3. Results of these geometrical measures were estimated with a developed Matlab function and are summarized in Tables 4.7 and 4.8 for various conditions. It should be mentioned that only simulation results for which the implicit springback solution converged were reported here. It can be seen that the results for no bead conditions are more erroneous than those with the beads.

The effect of friction coefficient was investigated by conducting several simulations for no bead conditions of TPIP780 with DER 12 and the results are shown in Fig.4.23. It can be seen that the relative error on sidewall curvatures decreases when higher values of friction coefficient are used.

Table 4.7: Geometrical measures for channel sidewall profiles with shallow beads, predicted with LS-DYNA

Channel condition	LS-DYNA Mat.Type	Element Formulation	NIP	Sidewall opening angle <sup>o</sup>	Curl fitted radius, mm	Flange tip angle <sup>o</sup>
Experimental results				16.9	121.3	103
TPSB	24	2	9	14.9	146.2	84.1
	36	2	9	12.9	148.1	84.6
	36	16	19	13.9	138.7	79.8
	37	2	9	13.6	163.3	80.0
	37	16	19	20.0	117.6	99.3
	125	2	9	12.0	247.2	43.8
Experimental results				24	117	100
DPSB	36	2	9	18.5	174.7	78.7
	36	16	19	5.8	164.4	78.5
	37	2	9	18.1	191.7	73.5
	37	16	19	23.4	139.4	86.2
	125	2	9	21.8	259.7	60.1
	125	16	51	20.6	141.0	84.9

Table 4.8: Geometrical measures for channel sidewall profiles without beads and DER=12 mm, predicted with LS-DYNA

Channel condition	LS-DYNA Mat.Type	Element Formulation	NIP	Sidewall opening angle <sup>o</sup>	Curl fitted radius, mm	Flange tip angle <sup>o</sup>
Experimental results				21	107	126
TPNB12	24	2	9	23.1	131.3	88.2
	36	16	19	24.4	150.2	81.4
	37	2	9	16.0	157.9	78.6
	37	16	19	26.8	147.6	81.6
	37	16	25	23.6	138.4	87.6
	125	16	9	24.7	198.1	67.3
Experimental results				28	122	117
DPNB12	24	2	9	22.6	153.6	89.5
	37	2	9	29.9	208.9	92.7
	125	2	9	28.1	314.4	50.6

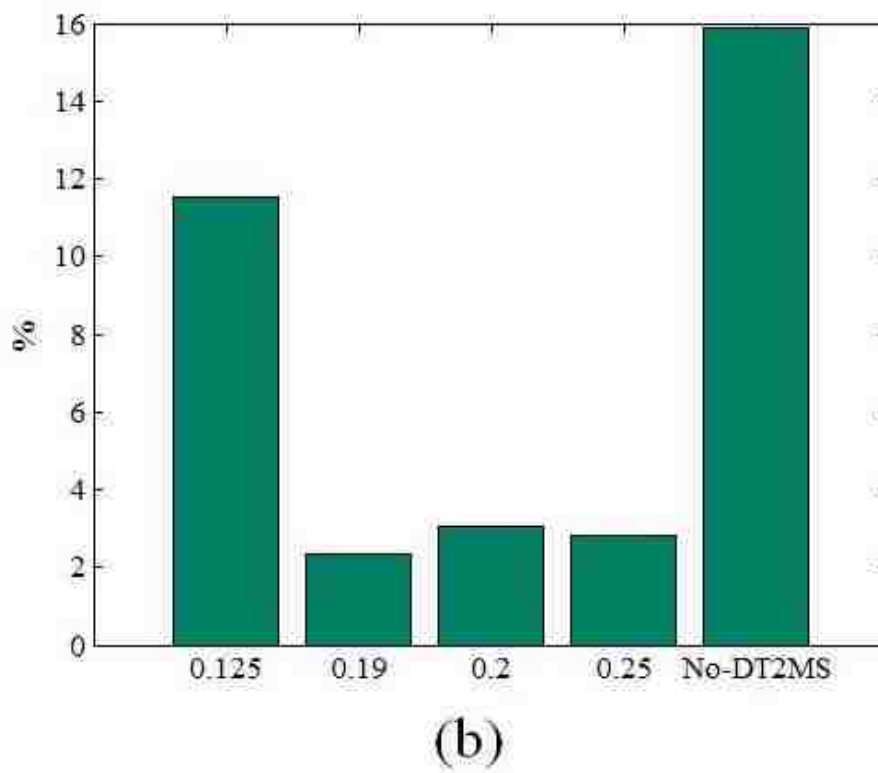
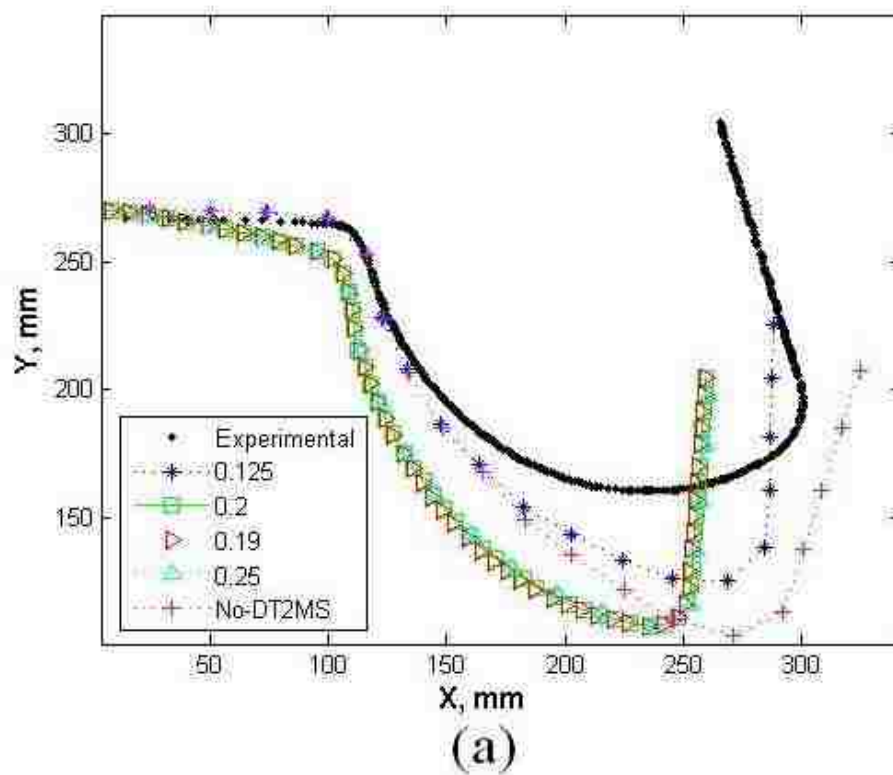


Figure 4.23: Simulated sidewall profiles for TPNB12 condition: a) with various friction coefficients, b) sidewall error (Eq. 4.8)

### 4.4.3 Thickness reduction and strain distribution

Shell thickness reduction and effective plastic and total strain values were obtained for each simulation in LS-DYNA. For TPSB and DPSB conditions, results of thickness reduction with material type 37, element formulation 16 and 19 integration points are shown in Fig.4.26, as a representative demonstration. Plastic strain distributions for the same simulations are displayed in Fig.4.27. It is notable that maximum values of thickness reduction and plastic strains for conditions with drawbeads, happened on sidewall of the channels after the impact of drawbeads. Strains along the width of channels were checked to ensure they are smaller than strains along width and through the thickness of the blank, confirming the plane stress condition of the simulations.

Thickness reduction and strain outputs of simulations for channels with and without beads and various models were summarized in Table 4.9. It should be noted that in order to compare simulation results with experimental values, maximum and minimum strains should be used instead of the plastic strains. As shown for a representative case of the forming simulations in Fig.4.24, maximum principal strains on lower, upper and mid surfaces of a shell element - which passes through the drawbead, over the die radius and ends up in the sidewall - converges to an average strain value, while the effective plastic strain is the accumulated result of the entire strain history. Minimum principal strains for the same element are also shown in Fig.4.25 and these converge to a value which is approximately the negative value of the maximum strain. The abrupt change that is observed in the strain history on the lower surface of this element (curve C), is due to the element passing through the drawbead region. But it can be seen that the strain levels on the upper and lower surfaces converged to the strain at the mid-plane. The simulation results that were reported in Table 4.9 showed an acceptable conformity with the experimental data summarized in Table 3.5.

Table 4.9: Summary of maximum values of thickness reduction and plastic strains predicted in the channel sidewalls

Channel condition	LS-DYNA Mat.Type	Element Formulation	NIP	Max. Thickness reduction (%)	Major sidewall strain (%)
Experimental results				5.8	4.0
TPSB	24	2	9	4.6	4.0
	36	2	9	4.5	4.1
	36	16	19	4.4	4.1
	37	2	9	4.3	3.9
	37	16	19	4.7	4.2
	125	2	9	4.5	2.5
Experimental results				3.4	2.4
DPSB	24	2	9	5.4	4.8
	36	16	19	5.8	4.2
	37	2	9	5.1	4.9
	37	16	19	4.8	3.6
	125	2	9	2.1	3.4
	125	16	51	3.2	3.4
Experimental results				1.25	0.8
TPNB12	24	2	9	1	0.08
	36	2	9	0.6	0.06
	37	2	9	0.5	0.06
	125	2	9	0.4	0.04
Experimental results				0.6	0.8
DPNB12	24	2	9	0.9	0.09
	37	2	9	0.5	0.8
	125	2	9	1	0.01



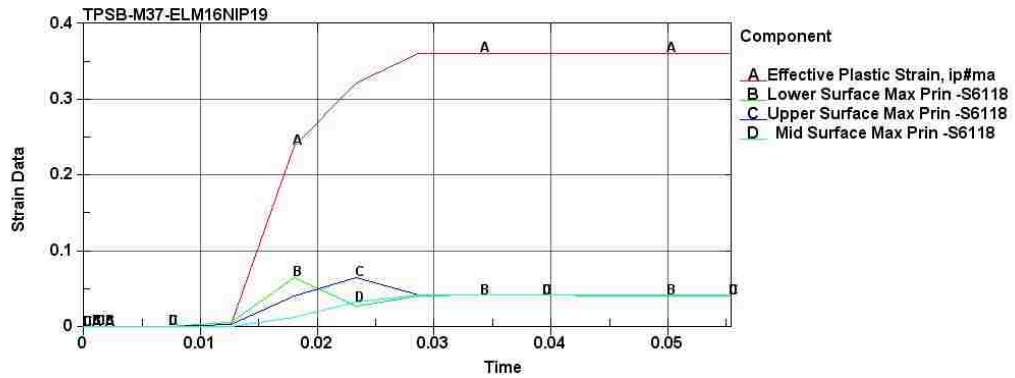


Figure 4.24: Maximum principal strain histories for an element on the sidewall of TPSB channel forming simulation

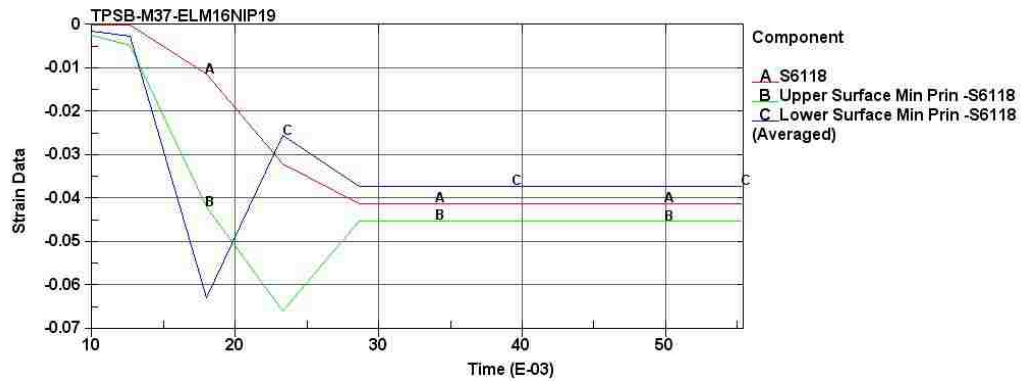


Figure 4.25: Minimum principal strain histories for an element on the sidewall of TPSB channel forming simulation

Finally, the shell thickness reduction and effective plastic strain distributions for TPSB and DPSB cases simulated with Mat37 model are shown in Figs.4.26 and 4.27, respectively.

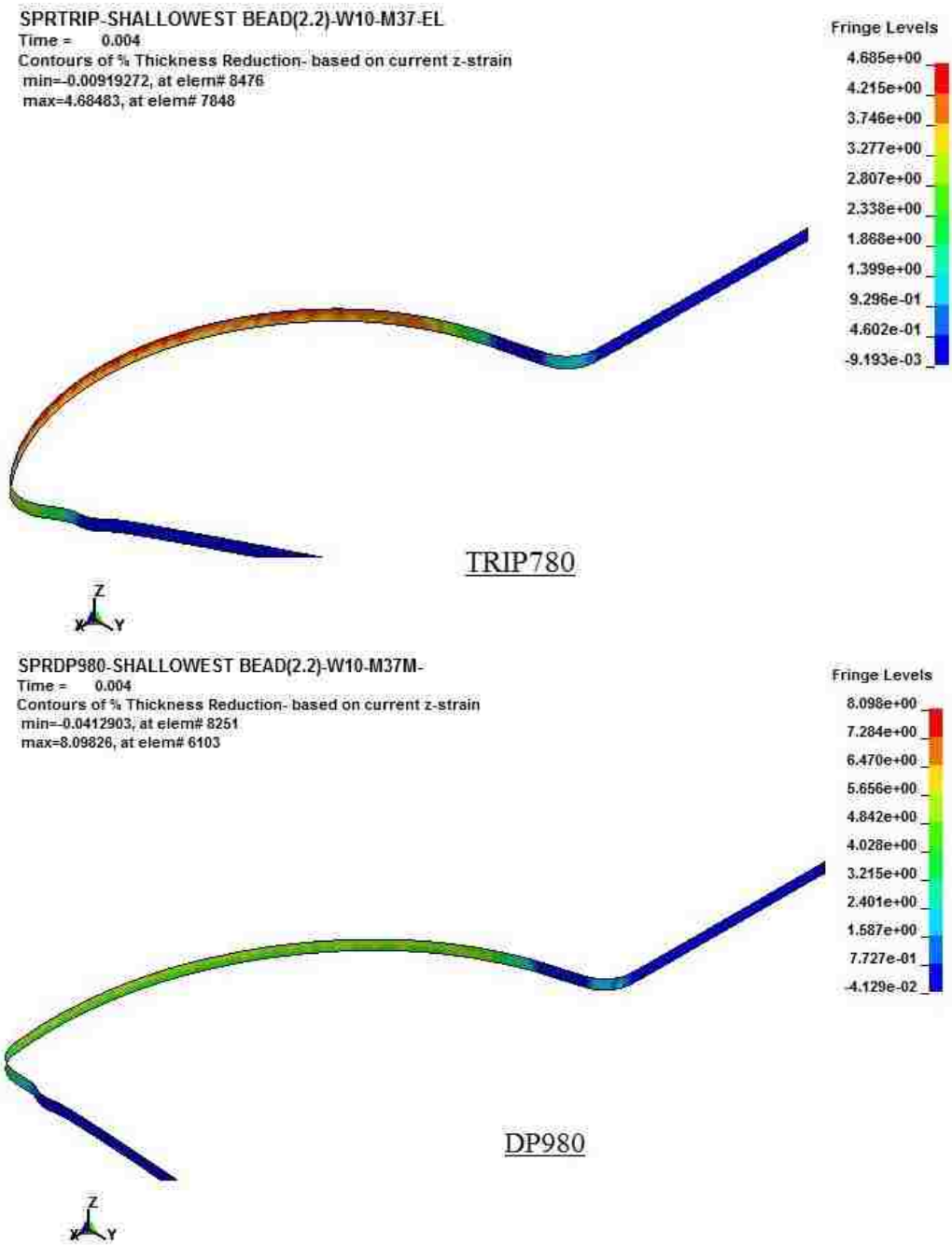


Figure 4.26: Shell thickness reduction (%) for TPSB and DPSB conditions

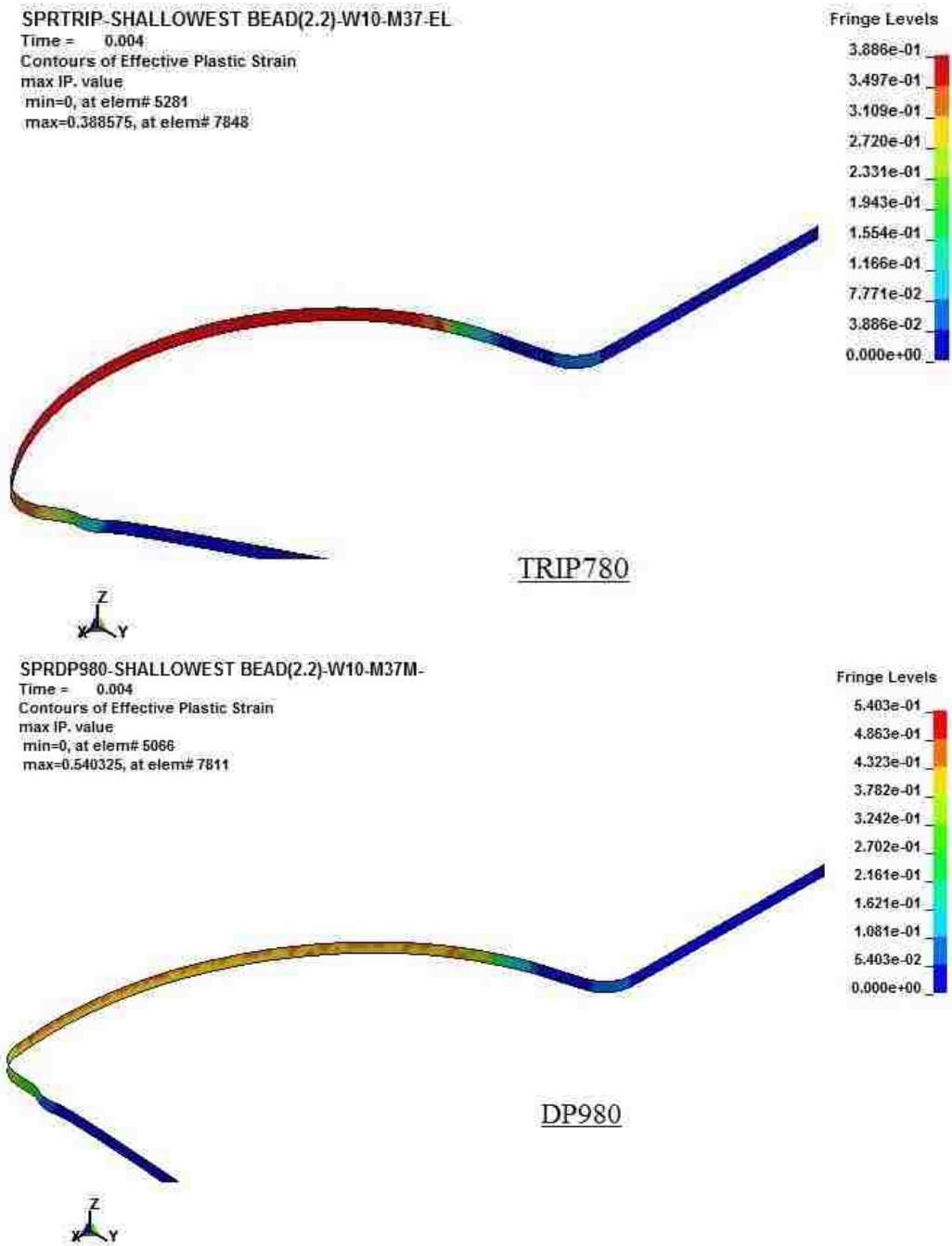


Figure 4.27: Effective plastic strain distributions for TPSB and DPSB conditions

# Final Discussions and Conclusions

---

In the previous chapters, various experimental results of the channel draw forming were presented and then compared with predicted results in LS-DYNA. Different material models were used to simulate the forming and springback of the U-channel sections made from advanced high strength materials TRIP780 and DP980. Also specific material characterization tests were performed on these two grades of AHSS.

Neither the TRIP780 nor the DP980 material showed any work-hardening stagnation during cyclic tension-compression tests, however, both sheet materials exhibited significant transient work-hardening during reverse loading. Both materials also showed significant Bauschinger effect although it was less significant for DP980 material, as the yield stress during reverse loading was closer to that in forward loading than TRIP780. The isotropic hardening model (IH) which is implemented in material types 24, 36 and 37 of LS-DYNA, is not able to accurately describe the cyclic behaviour of either materials. Although this prediction can be improved when numerical parameters are finely tuned with Nelder-Mead simplex optimization method, as shown in Fig.5.1, but it still cannot predict the reverse loading or the re-loading behaviours.

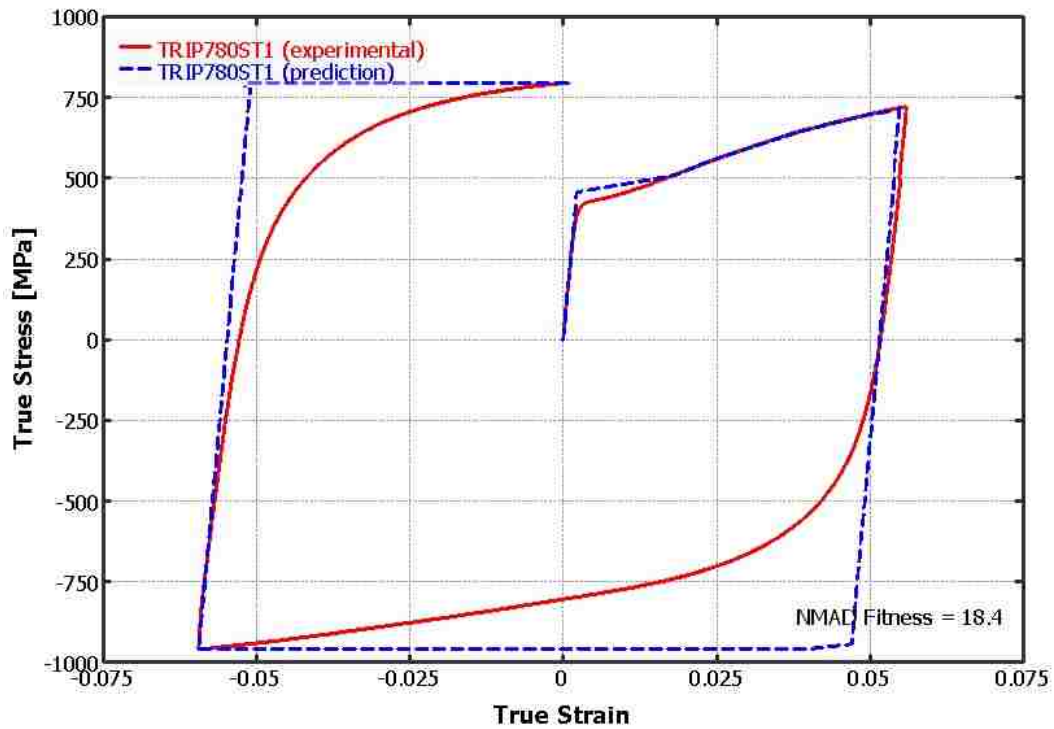
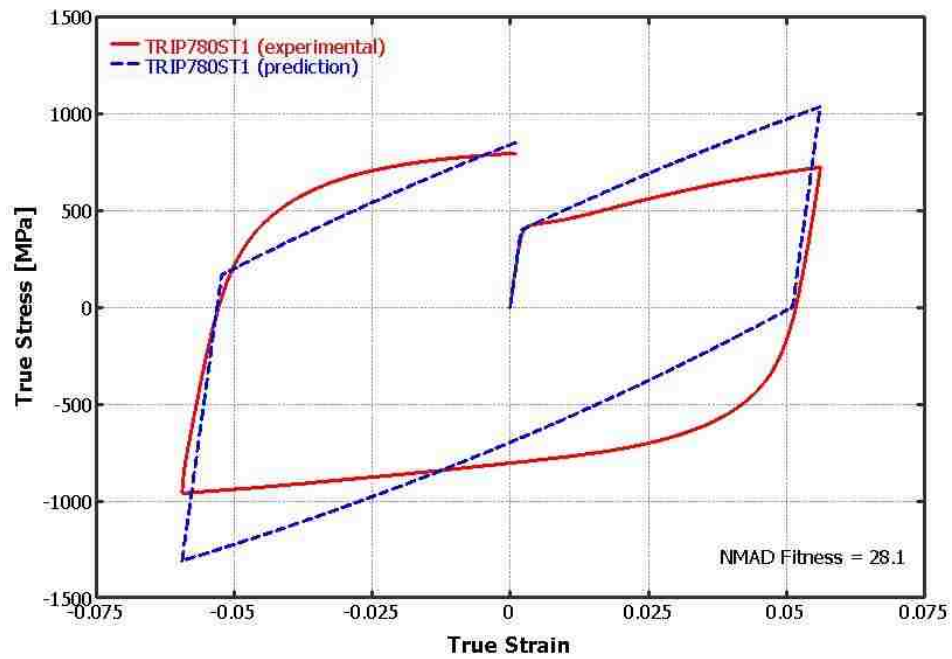
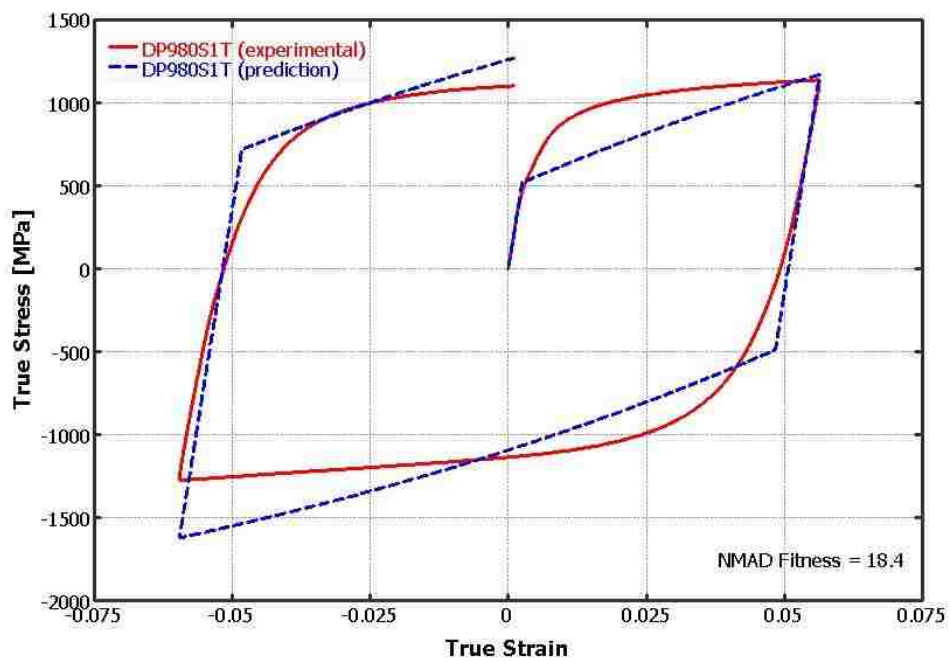


Figure 5.1: Modified prediction of cyclic behaviour of TRIP780 sheet metal by the isotropic hardening law

The combined isotropic-linear kinematic hardening model (which is also available in LS-DYNA as material model 3, MAT\_PLASTIC\_KINEMATIC) is also not able to accurately predict the cyclic behaviour of the two sheet steels as it can be seen in Fig.5.2. However, the cyclic behaviour of TRIP780 and DP980 is very well predicted with the YU model (Mat125), as shown in Fig.4.5.



(a)



(b)

Figure 5.2: Prediction of the cyclic behaviour of a)TRIP780 and b)DP980 with the combined isotropic-linear kinematic hardening law

Since the YU model is able to predict the actual cyclic behaviour of these sheet

material, it was expected that it would also accurately predict the actual forming and springback of the channel section. However, the miscalculation of energy balances and probably the stress state with the YU model (Mat 125) limits its applicability. This is because of the incorrect implementation of the YU model in LS-DYNA solver (version 971 edition R5.1.1). To show this, the energy balance and punch force results predicted with the YU model in ABAQUS were examined in Chapter 4 and did not exhibit such error for a similar representative case (TPSB), in Figs.4.10 and 4.11.

Further comparison can be made from the results of simulations in ABAQUS with those from LS-DYNA. Fig.5.3 compares the predicted channel sidewall profiles for the TPSB case carried out with both ABAQUS and LS-DYNA. The YU material model, with the parameters in Table 4.3, was used to obtain these results. As can be seen, more accurate prediction of the channel profile is achieved by YU model in ABAQUS than LS-DYNA. A similar result is also observed for the DPSB case. In terms of the sidewall curvature, less than 8% error was calculated for the simulation results with ABAQUS compared to the experimental results. Another interesting result is the over-prediction of the channel profiles with the YU model with respect to the experimental values in ABAQUS. This is most probably due to the fact that the material parameters reported by Shi et. al [46] were not optimized for the DP980 material used in the current study. It is intended to continue this aspect of the research using an optimization code for ABAQUS, and also when the bug is fixed for Mat125 in LS-DYNA.

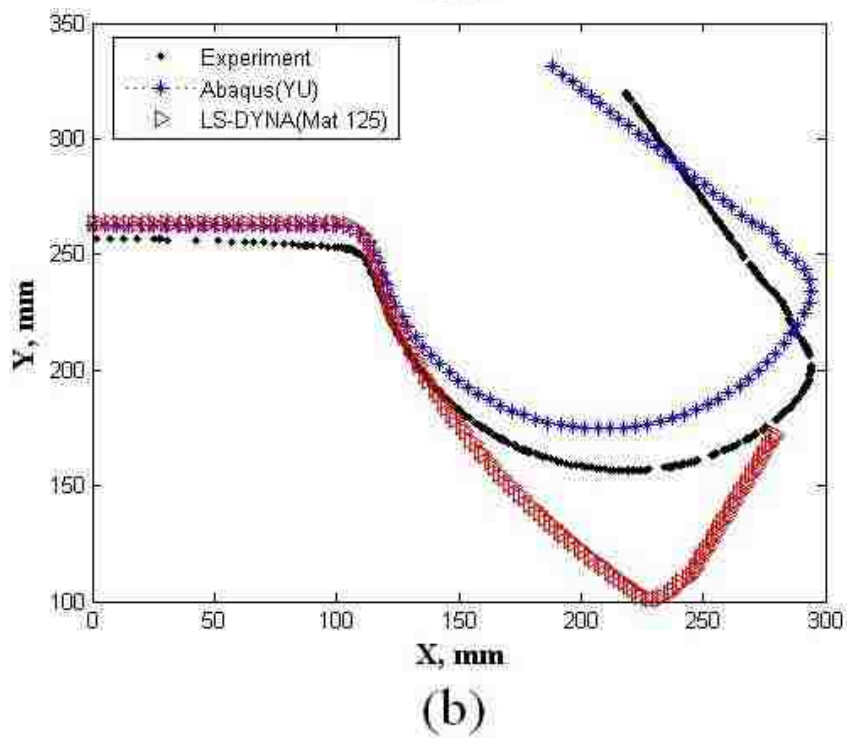
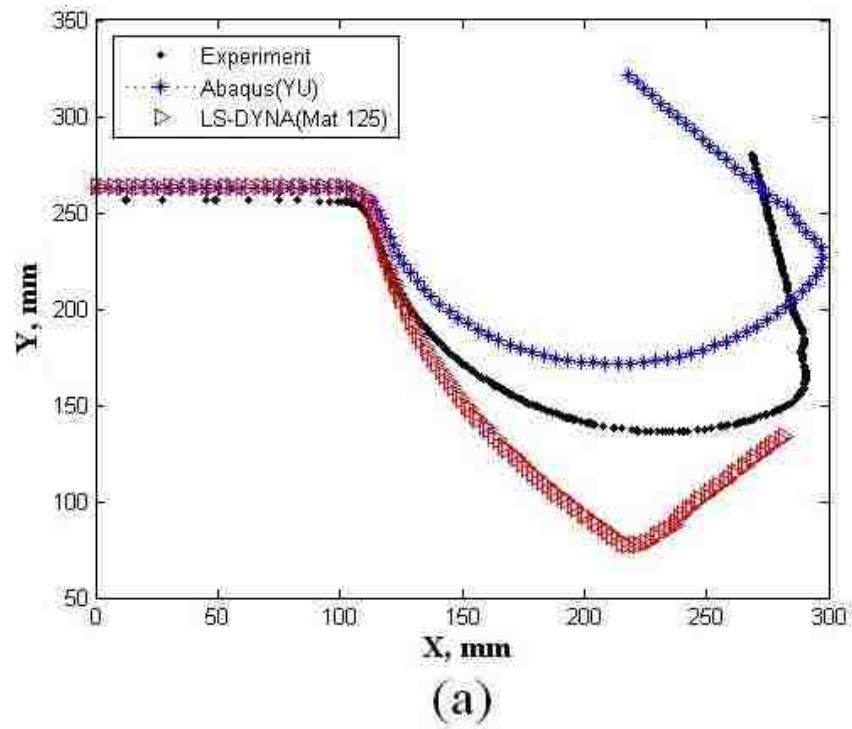


Figure 5.3: Channel sidewall profiles predicted with the YU model in ABAQUS and LS-DYNA and compared with the experimental results for: a)TRIP780 (TPSB), b)DP980 (DPSB)



Also, the thickness of the sheet metal for various points along the channel section was obtained from the simulations in ABAQUS as shown in Fig.5.4. They are in good agreement with experimental measurements reported in Table 3.5, by 2 and 3% thickness reduction for TRIP780 and DP980 channels with shallow beads, respectively.

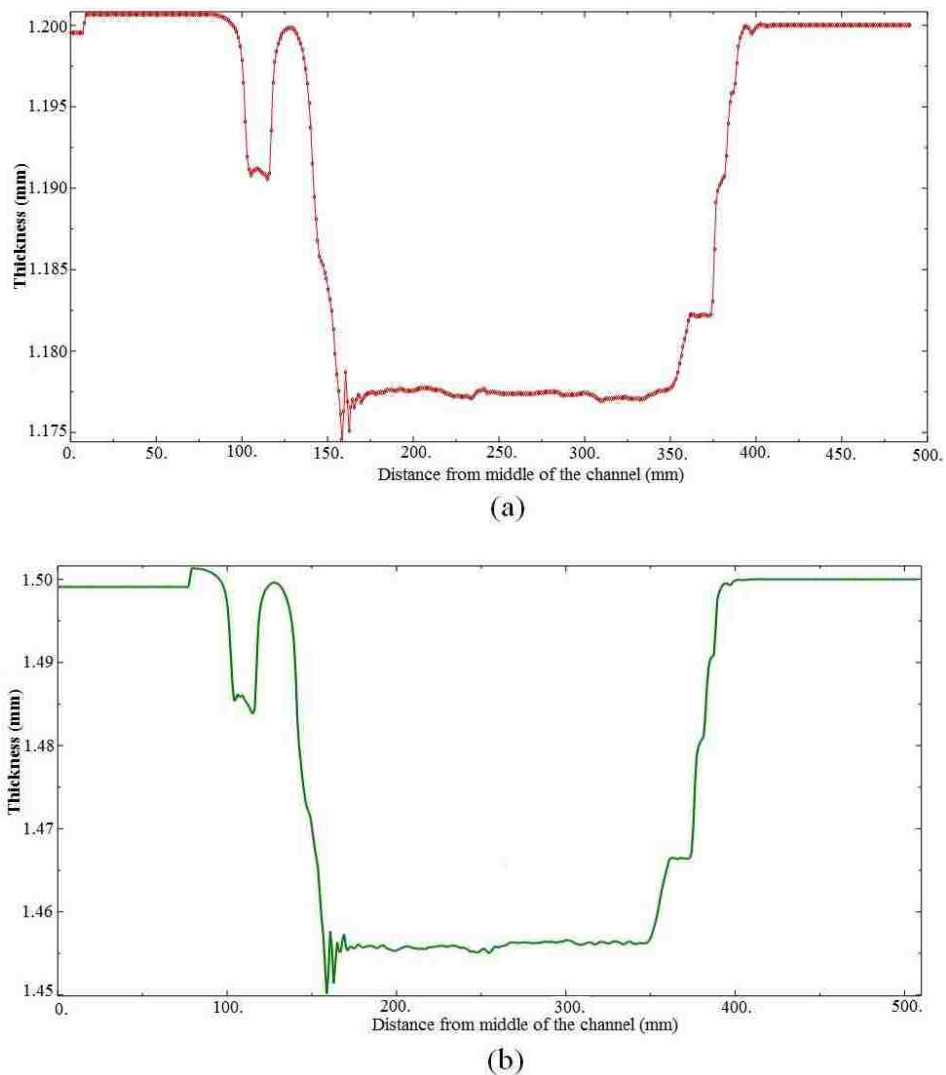


Figure 5.4: Prediction of the thickness along the channel section predicted with the YU model in ABAQUS for: a) TRIP780 (TPSB), b) DP980 (DPSB)

As a summary of the work done in this study, a U-channel draw process (BM3 of Numisheet 2005) was simulated with the FE code LS-DYNA and material models

24, 36, 37 and 125 for TRIP780 and DP980 sheet materials. Experimental channel sections were drawn with various drawbead penetrations and without drawbeads but with different die entry radii. Based on the numerical studies of Chapter 4 and comparisons with the experimental results in Chapter 3, the following conclusions can be drawn for this study:

1. For advanced high strength steels such as TRIP780 and DP980, parameters of the constitutive model have a great impact on the convergence of the springback simulations. Without appropriate parameters, it is likely that the implicit springback simulation will not converge to an appropriate solution.
2. From the material models in the LS-DYNA library, Mat 125 (YU) failed to predict accurate sprungback and sidewall curl results. The stress and strain distributions and various energy levels predicted with this material model show significant deviation from what is predicted by other material models. These results were also different from results predicted with the YU model implemented in ABAQUS used-defined model.
3. Mat 37 (transverse anisotropy constitutive model) with increased number of integration points (up to 19) yielded more accurate results than other material models in the LS-DYNA library which were used to predict the sidewall curl of channels made of TRIP780 and DP980.
4. The severity of sidewall curl increased when no drawbeads were used and also when a tighter die entry radius was used for both TRIP780 and DP980.
5. When drawbeads were used in the channel draw process, springback (wall opening angle) decreased but sidewall curl increased in the channel sections for both TRIP780 and DP980.
6. By comparison of the sprungback channel sidewall profiles of TRIP780 when the blanks were taken parallel and perpendicular to the sheet rolling direction,

it was concluded that in-plane anisotropy did not have a significant effect on the final sidewall curl. Tensile test results for samples cut at different angles with respect to the rolling direction also did not show significant variations.

7. Channels made of TRIP780 show less sidewall curl and less springback angle than those made of DP980.
8. The unloading elastic modulus of TRIP780 and DP980 was determined for a range of strain up to 0.1. Although the results were fitted to the empirical decaying function of plastic strains, the decreasing trend is expected to continue even beyond this strain level. Further investigations are in progress in this regard.
9. The YU model implemented in ABAQUS with a user defined subroutine produced less than 8% error in predicting sidewall curl for channels made of TRIP780 and DP980 with the shallow drawbead configuration. Similar results are expected with LS-DYNA once the implementation of this constitutive model is corrected in the solver or a user-defined material model is developed for Yoshida in LS-DYNA.
10. The coefficient of friction had an important effect in predicting punch force results of the forming stage when no drawbeads were present in the model. When drawbeads were used, the tension force on the blank was mainly produced in the drawbead region and the friction coefficient had a minor effect.
11. The amount of predicted sidewall curl and springback depended on the material constants which were obtained by fitting the simulated stress-strain curves to the experimental data. Therefore an optimization method was required to minimize the fitting error and globally determine the best set of parameters. It is worth noting various sets of material parameters are expected from different types of cyclic tests, and this may affect the accuracy of the results. Further investigation is required in this regard.

# Simulation of B-pillar

---

The forming and springback of an industrial auto body part known as B-pillar made of DP980 sheet steel with a thickness of 1.5 mm was simulated with LS-DYNA. The FE model of the forming process was created and analyzed here, using the findings from the current study. Material model 37 with 19 integration points through the thickness and fully integrated element formulation (type 16) was used. The upper and lower tools were created with zero offset as shown in Fig.A.1. Two “FORMING\_ONE\_WAY\_SURFACE\_TO\_SURFACE” contact algorithms with a friction coefficient of 0.1 were defined between the blank and the upper and lower tools. A prescribed rigid motion boundary condition in the form of a velocity curve was assigned to the upper tool to form the part in one step until the complete closure of the die. Adaptive meshing and other control parameters were assigned similar to the channel forming simulations. The deformed part after the forming stage was submitted to an implicit springback solution by fixing three points to eliminate the rigid body motion of the part. The result of the forming stage is shown Fig.A.2 and the result of the springback stage is shown in Fig.A.3 which showed very little springback or twist in the part. More investigation for the improvement of the analysis is in progress.

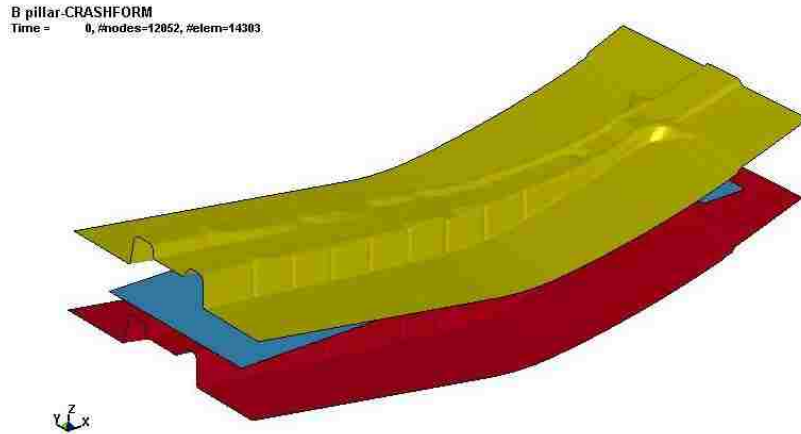


Figure A.1: FE model of crash forming a B pillar part from DP980

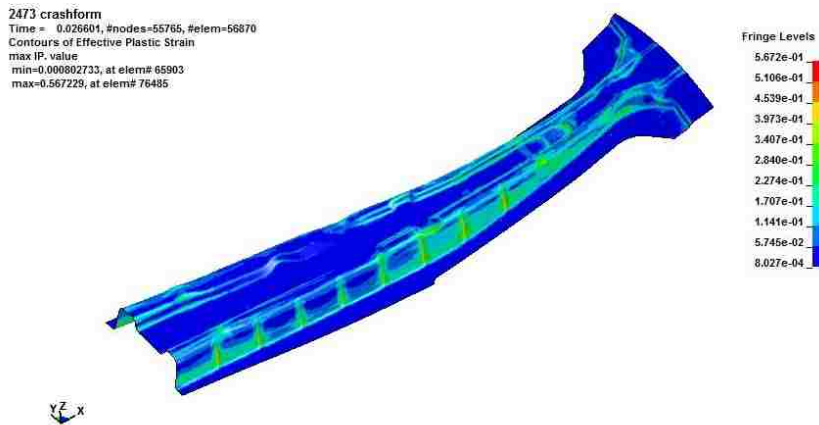


Figure A.2: Plastic strain distribution of forming simulation of a B-pillar, using Mat37

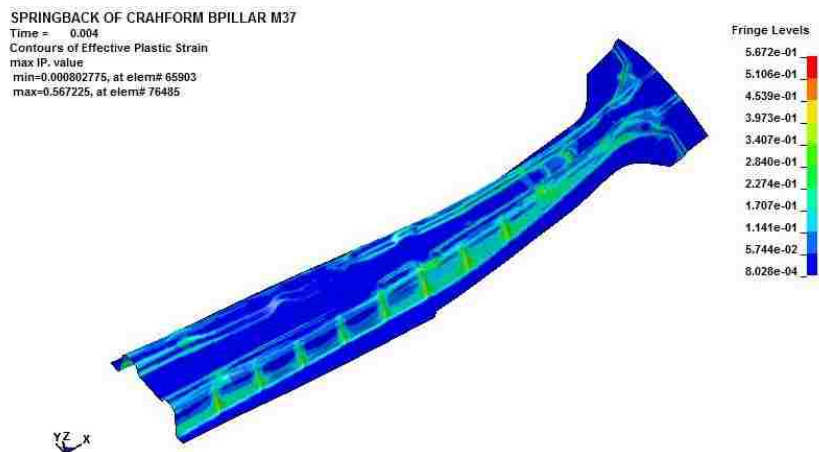


Figure A.3: Predicted sprungback B-pillar, using Mat37 model

# Bibliography

- [1] AHSS application guidelines. Technical report, World Auto Steel, June, 2009. (Cited on pages 4, 5, 6, 7, 8, 9 and 10.)
- [2] R. A. Ayres. Shapset: A process to reduce sidewall curl springback in high strength rails. *Applied Metalworking*, 2(3):127–134, 1984. (Cited on page 14.)
- [3] S. Al. Azraq, R. Teti, and J. Costa. Springback prediction with FEM analysis of advanced high strength steel stamping process. *Intelligent Production Machines and Systems*, pages 264–269, 2006. (Cited on page 20.)
- [4] I. A. Burchitz. *Improvement of Springback Prediction in Sheet Metal Forming*. PhD thesis, Twente University, 2008. (Cited on page 11.)
- [5] M.S. Bzdok, J. Fekete, and C Du. High strength steel stamping projects. Technical report, Auto/Steel Partnership, 2005. (Cited on page 15.)
- [6] J. Cao and Th. Buranathiti. An effective analytical model for springback prediction in straight flanging processes. *International Journal of Manufacturing and Product Technology*, 21:137–153, 2004. (Cited on pages 16 and 17.)
- [7] J. Cao, W. Lee, H. S. Cheng, M. Seniw, H.P. Wang, and K. Chung. Experimental and numerical investigation of combined isotropic-kinematic hardening behavior of sheet metals. *International Journal of Plasticity*, 25(5):942–972, 2009. (Cited on page 31.)
- [8] J. Chaboche. A review of some plasticity and viscoplasticity constitutive theories. *International Journal of Plasticity*, 24(10):1642–1693, 2008. (Cited on page 27.)
- [9] J.L. Chaboche. Time-independent constitutive theories for cyclic plasticity. *International Journal of Plasticity*, 2(2):149–188, 1986. (Cited on page 29.)

- 
- [10] F.K. Chen and P.C. Tseng. Deformation analysis of side-wall curl in the sheet metal forming of flanged channels. *Journal of Manufacturing Science and Engineering*, 127(2):369–375, 2005. (Cited on page 17.)
- [11] N. Christodoulou, O.T. Woo, and S.R. MacEwen. Effect of stress reversals on the work hardening behaviour of polycrystalline copper. *Acta Metallurgica*, 34(8):1553–1562, 1986. (Cited on page 38.)
- [12] C. C. Chu. The effect of restraining force on springback. *International Journal of Solids Structures*, 8(27):1035–1046, 1991. (Cited on page 16.)
- [13] K. Chung, M. Lee, D. Kim, C. Kim, M. L. Wenner, and F. Barlat. Spring-back evaluation of automotive sheets based on isotropic-kinematic hardening laws and non-quadratic anisotropic yield functions Part I : theory and formulation. *International Journal of Plasticity*, 21:861–882, 2005. (Cited on pages 20, 21 and 26.)
- [14] J.M. Collin, T. Parenteau, G. Mauvoisin, and P. Pilvin. Material parameters identification using experimental continuous spherical indentation for cyclic hardening. *Computational Materials Science*, 46(2):333–338, 2009. (Cited on page 32.)
- [15] R. G. Davies. Side-wall curl in high-strength steels. *Applied Metalworking*, 2(3):120–126, 1984. (Cited on page 14.)
- [16] F. Dunne and N. Petrinic. *Introduction to Computational Plasticity*. Oxford University press, 2005. (Cited on pages 23 and 25.)
- [17] P. Eggertsen and K. Mattiasson. On constitutive modeling for springback analysis. *International Journal of Mechanical Sciences*, 52(6):804–818, 2010. (Cited on page 32.)
- [18] P. Eggertsen and K. Mattiasson. On the identification of kinematic hardening

- material parameters for accurate springback predictions. *International Journal of Material Forming*, 4(2):103–120, 2010. (Cited on page 37.)
- [19] P. Eggertsen and K. Mattiasson. On the modeling of the unloading modulus for metal sheets. *International Journal of Material Forming*, 3(S1):127–130, 2010. (Cited on pages 39 and 41.)
- [20] Barlat F., J.M. Ferreira, J.J. Gracio, Lopes A.B., and Rauch E.F. Plastic flow for non-monotonic loading conditions of an aluminum alloy sheet sample. *International Journal of Plasticity*, 19:1215–1244, 2003. (Cited on page 31.)
- [21] M. Firat, B. Kaftanoglu, and O. Eser. Sheet metal forming analyses with an emphasis on the springback deformation. *Journal of Materials Processing Technology*, 196(1-3):135–148, 2008. (Cited on pages 22, 23, 28 and 30.)
- [22] Chen F.K. and Tseng P.C. Deformation analysis of sidewall curl in sheet metal forming of flanged channels. *Manufacturing Science and Engineering*, 127:369–375, 2005. (Cited on page 3.)
- [23] C.O. Frederick and P.J. Armstrong. A Mathematical representation of the multiaxial Bauschinger effect. Technical report, G.E.G.B Report RD/B/N731, 1966. (Cited on page 29.)
- [24] L. Geng and R.H. Wagoner. Role of plastic anisotropy and its evaluation in springback. *International Journal of Mechanical Sciences*, 44(1):123–148, 2002. (Cited on page 23.)
- [25] A. Ghaei. *Modeling springback in stamped automotive structures*. PhD thesis, University of Windsor, 2009. (Cited on pages 19, 26, 106 and 109.)
- [26] A. Ghaei and D.E. Green. Numerical implementation of Yoshida-Uemori two-surface plasticity model using a fully implicit integration scheme. *Computational Materials Science*, 48(1):195–205, 2010. (Cited on page 22.)



- [27] D. E. Green. Description of Numisheet 2005 Benchmark #3 stage-1: Channel Draw with 75% drawbead penetration. *Proceedings of Numisheet 2005*, B(1):894–904, 2005. (Cited on page 11.)
- [28] T. Hasegawa, T. Yakou, and S. Karashima. Deformation behaviour and dislocation structures upon stress reversal in polycrystalline aluminum. *Materials Science and Engineering*, 20:267–276, 1975. (Cited on page 38.)
- [29] Y. Hayashi and M. Tagagi. Control of side-wall curl in draw-bending of high strength steel sheets. *Advanced Technology of Plasticity*, 1:735–740, 1984. (Cited on page 14.)
- [30] Miyauchi K. A proposal of a planar simple shear test in sheet metals. *Scientific Papers of the Institute of Physical and Chemical Research*, 78(3):27–40, 1984. (Cited on page 31.)
- [31] L. Kessler, M. S. Aydin, and J. Gerlach. Springback simulation with complex hardening material models. In *7th LS-DYNA Conference*, pages 1–10, 2008. (Cited on pages 21 and 33.)
- [32] A. S. Khan and S. Huang. *Continuum Theory of Plasticity*. John Wiley & Sons. Inc., 1996. (Cited on page 28.)
- [33] J. K. Kim and P. F. Thomson. Springback and side-wall curl of galvanized and galvalume steel sheets. *Mechanical Working Technology*, 19:223–238, 1989. (Cited on page 15.)
- [34] T. Kuwabara, Y. Morita, Y. Miyashita, and S. Takahashi. Elastic-plastic behavior of sheet metal subjected to in-plane reverse loading. In *5-th International Symposium on Plasticity and its current applications*, pages 841–844, 1995. (Cited on page 30.)
- [35] M.G. Lee, D. Kim, R. H. Wagoner, and K. Chung. Semi-Analytic hybrid

- method to predict springback in the 2D draw bend test. *Journal of Applied Mechanics*, 74(6):1264–1275, 2007. (Cited on pages 17 and 18.)
- [36] B.S. Levy, C.J. Van Tyne, Y.H. Moon, and C. Mikalsen. The effective unloading modulus for automotive sheet steels. In *Proceeding of SAE 2006 World Congress & Exhibition, Detroit, MI, USA*, pages 264–269, 2006. (Cited on pages 39 and 84.)
- [37] Y. C. Liu. The effect of restraining force on shape deviations in flanged channels. *ASME Journal of Engineering Materials Technology*, 110:389–394, 1988. (Cited on page 14.)
- [38] Livermore Software Technology Corporation (LSTC). *LS-DYNA keyword user's manual. Vol. I. version 971*, 2007. (Cited on pages 32 and 45.)
- [39] D. Matlock, T.B. Hilditch, and J. Speer. Influence of low-strain deformation characteristics of high strength sheet steel on curl and springback in bend-under-tension tests. *Journal of Materials Processing Technology*, 182(1-3):84–94, 2007. (Cited on page 21.)
- [40] O. E. Mattiasson and Enqvist B. K. Identification of material hardening parameters by the three-point bending of metal sheets. *International Journal of Mechanical Sciences*, 48:1525–1532, 2006. (Cited on page 31.)
- [41] Y. Moon, D Kim, and C Vantyne. Analytical model for prediction of side-wall curl during stretch-bend sheet metal forming. *International Journal of Mechanical Sciences*, 50(4):666–675, 2008. (Cited on page 19.)
- [42] Genevois P. *Etude expérimentale et modélisation du comportement plastique anisotrope de tôles d'acier en grandes déformations*. PhD thesis, Institute National Polytechnique de Grenoble, 1992. (Cited on page 31.)
- [43] F. Pourboghrat and E.Chu. Prediction of spring-back and side-wall curl in 2-d

- draw bending. *Materials Processing Technology*, 50:361–374, 1995. (Cited on pages 3 and 16.)
- [44] E.F. Rauch. Plastic anisotropy of sheet metals determined by simple shear tests. *Journal of Material Science and Engineering*, 241:179–183, 1998. (Cited on page 31.)
- [45] M. Samuel. Experimental and numerical prediction of springback and side wall curl in U-bendings of anisotropic sheet metals. *Journal of Materials Processing Technology*, 105(3):382–393, 2000. (Cited on page 20.)
- [46] M. F. Shi, X Zhu, C. Xia, and T. Stoughton. Determination of nonlinear isotropic/kinematic hardening constitutive parameters for AHSS using tension and compression tests. In *Proceedings of Numisheet 2008*, pages 264–270, 2008. (Cited on pages 104, 105 and 143.)
- [47] N. Stander, W. Roux, T. Eggleston, and K. Craig. *LS-OPT User's Manual, version 4.2*. (Cited on pages 32 and 101.)
- [48] A. Taherizadeh, A. Ghaei, D. E. Green, and W. J. Altenhof. Finite element simulation of springback for a channel draw process with drawbead using different hardening models. *International Journal of Mechanical Sciences*, 51(4):314–325, 2009. (Cited on page 22.)
- [49] S. C. Tang. Analysis of springback in sheet forming operation. *Advanced Technology of Plasticity*, I:193–197, 1987. (Cited on page 15.)
- [50] L. Taylor, J. Cao, M. C. Karafillis, and M. C. Boyce. Numerical simulations of sheet-metal forming. *Materials Processing Technology*, 50:168–179, 1995. (Cited on page 15.)
- [51] N. E. Thompson and C. H. Ellen. A simple theory for side-wall curl. *Applied Metalworking*, 1(4):39–42, 1985. (Cited on page 15.)

- [52] R. Wagoner and M. Li. Simulation of springback: Through-thickness integration. *International Journal of Plasticity*, 23(3):345–360, 2007. (Cited on page 18.)
- [53] R.H. Wagoner, R.K. Boger, F. Barlat, M.G. Lee, and K. Chung. Continuous, large strain, tension/compression testing of sheet material. *International Journal of Plasticity*, 21(12):2319–2343, 2005. (Cited on page 31.)
- [54] D.Y. Yang and S.W. Lee. An assessment of numerical parameters influencing springback in explicit finite element analysis of sheet metal forming process. *Journal of Materials Processing Technology*, 80-81:60–67, 1998. (Cited on page 19.)
- [55] H. K. Yi, D. W. Kim, C. J. Van Tyne, and Y. H. Moon. Analytical prediction of springback based on residual differential strain during sheet metal bending. *Journal of Mechanical Engineering Science*, 222(2):117–129, 2008. (Cited on page 18.)
- [56] F. Yoshida, Urabe M., and V.V. Toropov. Identification of material parameters in constitutive model for sheet metals from cyclic bending tests. *International Journal of Mechanical Sciences*, 40:237–249, 1998. (Cited on pages 31 and 32.)
- [57] F. Yoshida and T. Uemori. A model of large-strain cyclic plasticity describing the Bauschinger effect and work-hardening stagnation. *International Journal of Plasticity*, 18(5-6):661–686, 2002. (Cited on pages 29, 32, 33 and 43.)
- [58] F. Yoshida and T. Uemori. A model of large-strain cyclic plasticity and its application to springback simulation. *International Journal of Mechanical Sciences*, 45:1687 – 1702, 2003. (Cited on pages 34, 35 and 40.)
- [59] F. Yoshida, T. Uemori, and S. Abe. Modeling of large-strain cyclic plasticity for accurate springback simulation. *Key Engineering Materials*, 340-341:811–816, 2007. (Cited on page 38.)

- 
- [60] F. Yoshida, T. Uemori, and K. Fujiwara. Elastic-plastic behavior of steel sheets under in-plane cyclic tension-compression at large strain. *International Journal of Plasticity*, 18(5-6):633–659, 2002. (Cited on pages 29, 30, 41 and 42.)
- [61] F. Yoshida, M. Urabe, R. Hino, and V.V. Toropov. Inverse approach to identification of material parameters of cyclic elasto-plasticity for component layers of a bimetallic sheet. *International Journal of Plasticity*, 19(12):2149–2170, 2003. (Cited on page 32.)
- [62] D. Zhang, Z. Cui, X. Ruan, and Y. Li. An analytical model for predicting springback and side wall curl of sheet after U-bending. *Computational Materials Science*, 38(4):707–715, 2007. (Cited on page 18.)
- [63] K. M. Zhao and J. K. Lee. Generation of cyclic stress-strain curves for sheet metals. *Journal of Engineering Materials and Technology*, 123(4):391–395, 2001. (Cited on page 31.)

---

## VITA AUCTORIS

NAME	Ali Aryanpour
PLACE OF BIRTH	DEZFOOL, IRAN
YEAR OF BIRTH	1977
EDUCATION	KAMAL HIGH SCHOOL, TEHRAN, IRAN 1991 - 1995 Sharif University, Tehran, IRAN 1995 - 1999, B.A.Sc. University of Windsor, Windsor, Ontario 2009 - 2011, M.A.Sc.